

THESIS FOR THE DEGREE OF DOCTOR OF PHILOSOPHY

Component and system
design of a mild hybrid
48 V powertrain for
a light vehicle

STEFAN SKOOG



Department of Electrical Engineering
Chalmers University of Technology
Gothenburg, Sweden, 2020

**Component and system
design of a mild hybrid
48 V powertrain for
a light vehicle**

STEFAN SKOOG

Copyright © 2020 STEFAN SKOOG
All rights reserved.

Technical Report No. 4790
ISSN 978-91-7905-323-9
This thesis has been prepared using L^AT_EX.

Department of Electrical Engineering
Chalmers University of Technology
SE-412 96 Gothenburg, Sweden
Phone: +46 (0)31 772 1000
www.chalmers.se

Printed by Chalmers Reproservice
Gothenburg, Sweden, May 2020

*This thesis is dedicated to the
giants in science and engineering upon
whose shoulders I have the privilege to stand.*

Abstract

This thesis presents contributions in three areas relevant for the development of 48 V mild hybrid electric powertrains for cars. The first part comprises methodologies and extensive testing of lithium-ion battery cells in order to establish the electric and thermal performance by using equivalent circuit models. Empirical, lumped-parameter models are used to ensure fast simulation execution using only linear circuit elements. Both electrochemical impedance spectroscopy and high-current pulse discharge testing is used to extract model parameters. Plenty of parameter results are published for various cells, temperatures and SOC levels. Further on, the model accuracy in voltage response is also evaluated. It is found that an R+2RC equivalent circuit offers the lowest error, 11 mV RMSE in a 1.5 h drive cycle, which is among the lowest numbers found in the literature for similar models.

In the second part, electric machines with tooth-coil windings are explored as a viable candidate for mild hybrids. First, a method of analytically calculating the high-level electro-magnetic properties for all possible combinations of three-phase, dual layer tooth-coil winding machines is established and presented in a graphically appealing manner. Then, a pair of pseudo-6-phase 50 kW PMSMs are designed, constructed and validated in a custom designed calorimetric dynamo test stand. These machines feature a in-stator and in-slot forced oil cooling, enabling very high current densities of 25 A/mm² continuous and 35 A/mm² peak. A high net power density (19 kW/l) and a large area of high peak efficiency (95%) is shown numerically and validated by calorimetric measurements.

Finally, low-level design, construction and evaluation of 48 V inverter hardware is explored. By using high-performance, extra-low-voltage silicon-based MOSFETs with custom designed metal substrate printed circuit boards, custom made gate drivers, and water cooling, 3x220 A RMS is reached experimentally on a 154 cm² area and an efficiency of 95.6%.

Keywords: Hybrid Electric Vehicle, 48 V, Extra low voltage, Permanent Magnet Synchronous Machine, Efficiency, Oil cooling, Power density, Calorimetric, Li-ion battery, Power Electronics, Inverter, PWM, MOSFET, Multi-phase

Acknowledgments

I would like to express my gratitude to the following individuals who helped me to make this work possible:

Thank you Torbjörn Thiringer and Stefan Lundberg, my examiner and my supervisors at Chalmers, for excellent support, insightful feedback and valuable mentorship throughout my time at Chalmers.

At Volvo Cars, I truly appreciate the collaboration with Torbjörn Larsson, Alexander Robertsson, Patrik Stridh, Daniel Midholm, and Jonas Forsell.

At Chalmers, special thanks to Alessandro Acquaviva for the fruitful cooperation around electric machine development and testing. And to many of my colleagues at Chalmers with who I have collaborated or shared office space with: Andreas Andersson, Christian Dubar, Zeyang Geng, Emma Grunditz, Elisabeth Jansson, Douglas Jutsell, Felix Mannerhagen, Daniel Pehrman.

Pontus Fyhr at Lund University, for broad and deep discussions on design and production of vehicle electrification systems.

Jens Groot at AB Volvo, thanks for guidance and interesting discussions regarding battery performance testing.

Special thanks to Master's students contributing to this research project: Sandeep David[1], [2], for extensive battery measurements leading to the results in Paper 4.

Biju Jude[3], Akshay Santosh[3], Carl Tisell[4], Usman Tariq[4] for excellent collaboration in measurements for inverter prototypes and in assisting with hardware design and test setups.

Thanks to all the other Master's students whom I had the pleasure to collaborate with and supervise within this research project: Mohanapriya Anandaguru[5], Andreas Eriksson[5], Akik Biswas[6], Xuming Yao[6], Sebastian Larqvist[7], Hannes Östergren[7], Linas Brusokas[8], Naveen Raja[8].

Lastly, the financial support from the Swedish Governmental Agency for Innovation Systems (VINNOVA) is gratefully appreciated.

Acronyms

BEMF:	Back-ElectroMotive Force
CFD:	Computational Fluid Dynamics
CHT:	Conjugate Heat Transfer
CPE:	Constant Phase Element
CPE:	Constant-Phase Element
DE:	Drive end (of electrical machine)
DFT:	Discrete Fourier Transform
ECM:	Equivalent Circuit Model
ECU:	Electronic Control Unit
EIS:	Electrochemical Impedance Spectroscopy
EM:	Electric Machine
ESS:	Electrical Energy Storage System
ESS:	Electrical Storage System
EV:	Electric Vehicle
FEA:	Finite Element Analysis
FEM:	Finite Element Method
FFT:	Fast Fourier Transform
FSCW:	Fractional Slot (pitch) (non-overlapping) Concentrated Winding
G:	Graphite (LIB anode material)
HEV:	Hybrid Electric Vehicle
HLF:	Harmonic Leakage Factor
HTC:	Heat Transfer Coefficients
ICE:	Internal Combustion Engine
IPM:	Internal-Permanent magnet (synchronous) Machine
ISO:	International Organization for Standardization
KPI:	Key Performance Index
LCO:	Lithium-Cobalt Oxide (LIB cathode material)

LFP:	Lithium-FerroPhosphate (LIB cathode material)
LIB:	Lithium-Ion Battery, referes here to li-ion cell
LMO:	Lithium-Manganese Oxide (LIB cathode material)
LPN:	Lumped-Parameter Network (model)
LTO:	Lithium-Titanium Oxide (LIB anode material)
MBD:	Model-Based Development
mHEV:	mild Hybrid Electric Vehicle
MMF:	Magneto-Motive Force
MTPA:	Maximum Torque Per Ampere
NDE:	Non-Drive End (of electrical machine)
NMC:	(Lithium-)Nickel-Manganese-Cobalt oxide (LIB cathode material)
OCV:	Open Circuit Voltage
PHEV:	Plug-in Hybrid Electric Vehicle
PM:	Permanent Magnet
PMSM:	Permanent Magnet Synchronous Machine
RMSE:	Root-Mean-Square Error
RMSE:	Root-Mean-Squared Error
SOC:	State Of Charge
TCWM:	Tooth-Coil Wound Machine
VDA:	Verband der Automobilindustrie (organization)
WLTP:	Worldwide harmonised Light vehicle Test Procedure
VSI:	Voltage Source Inverter

Contents

Abstract	i
Acknowledgements	iii
Acronyms	iv
I Overview	1
1 Introduction	3
1.1 Background	3
1.2 Review of previous work	7
System Studies	7
Electric Machines	7
Power Electronics	9
Drive Systems: EM and PE	10
Battery modeling	11
1.3 Purpose of thesis	12
1.4 Thesis outline and methodology	12
1.5 Contributions	13
1.6 List of Publications	14

2	History and theoretical framework	15
2.1	Short history of electrification	15
2.2	Levels of electrification	16
2.3	Hybrid topologies	16
2.4	Why 48 V?	16
2.5	Battery modeling	18
	Equivalent Circuit Models	20
2.6	Electric machine	23
	Winding layout	23
	Equivalent circuit for electric machine	23
3	Case Setup	27
3.1	System assumptions	27
3.2	Battery testing	28
	Test equipment	28
3.3	Inverter test setups	31
3.4	Electric machine setup	36
	Winding layout	36
	Electric machine test setup	36
4	Results	43
4.1	Battery modeling	43
	Parameter results	43
	Voltage headroom	44
	Model verification	45
	High-level comparison	47
4.2	Inverter results	52
4.3	Electric machine results	53
	Winding layout	53
	Machine construction and results	53
5	Conclusions	57
5.1	Main conclusions	57
5.2	Future Work	61
A	Linear equivalent circuit model	63
	State space model	66

References	69
II Included Papers	77

Part I

Overview

CHAPTER 1

Introduction

1.1 Background

The fleet of personal vehicles in the world is known to be a considerable source of emissions by the burning of fossil fuels through internal combustion engines. In the EU, cars account for 18.2% of the total CO₂ emissions[1]. The transportation sector is the only sector not showing a clear trend in decrease in total pollution year by year[1]; the total car distance traveled is increasing much faster than the fleet average propulsion efficiency.

One part of the emission problem is that combustion engines are operated on hydrocarbons that have been stored for millions of years, which when combusted releases green house gasses into the atmosphere, disrupting the the natural carbon cycle. The other part of the problem is that cars, with their combustion engines, are releasing most green house gasses in densely populated areas and thus compromising the air quality where the human population density is the highest.

Authorities around the world, especially in the EU, have declared goals and targets for a more environmental friendly car fleet. The standard policy for fossil fuel based combustion engine vehicles is to put a cap on the fleet

average emission level measured in CO₂ equivalents. The goal is set to 95 g CO₂ per travelled kilometer on average in a WLTP drive cycle, for 95% of the car fleet in year 2020. By 2021, all new vehicles must comply to the same CO₂ figure[2]. These figures correspond to 4.1 l/100 km and 3.6 l/100 km fuel consumption for gasoline and diesel engines, respectively. This can be compared with the most fuel efficient series produced car, a Volkswagen Lupo 3L, with a real-world driving diesel consumption of 2.78 l/100 km[3]. The EU established a penalty system that requires each major OEM to pay 95 € for each car and for each g CO₂/km above the set fleet limit[4], which forms a clear incentive for the Original Equipment Manufacturers (OEMs) of personal vehicles to take action.

OEMs are responsible for offering their customers a range of cars that, when sold, will reach the target fleet average. OEMs now also have an interest to convince their customers to buy the lower-emitting vehicles they offer. Reducing a vehicle's average emission without changing the chassis type and functionality significantly, typically requires less powerful engines which limits the ability of active dynamical driving.

Many solutions to lower the average CO₂ emissions exist. All requires either massive change of transportation behavior, and/or massive investment in technology and infrastructure. Increasing the efficiency of the internal combustion engine is one feasible engineering leap to pursue, this can be done by engine downsizing, overcharging, cylinder deactivation, usage of more advanced materials to lower friction[5], exhaust gas recirculation (EGR) for gasoline vehicles[6] to mention some examples.

However, the goals are still set very challenging and to meet them only with improvements in combustion technology would imply forcing OEMs to front-load combustion engine R&D more than ever, which requires resources hard to allocate. This investment is so ambitious that many other alternatives seem more attractive. Honda and Toyota were the first major OEMs to introduce mild hybrid electric vehicles (mHEVs) in late 1990's for production cars, proving the viability of such systems. However, the technology was too expensive to apply on the majority of the car fleet and hybridisation was limited as a niche product.

The cost of implementing a mild hybridisation with a 48 V system can be 25% less compared to a corresponding class B voltage system according to Mahle[7]. This cost advantage allows mild hybridisation to be implemented

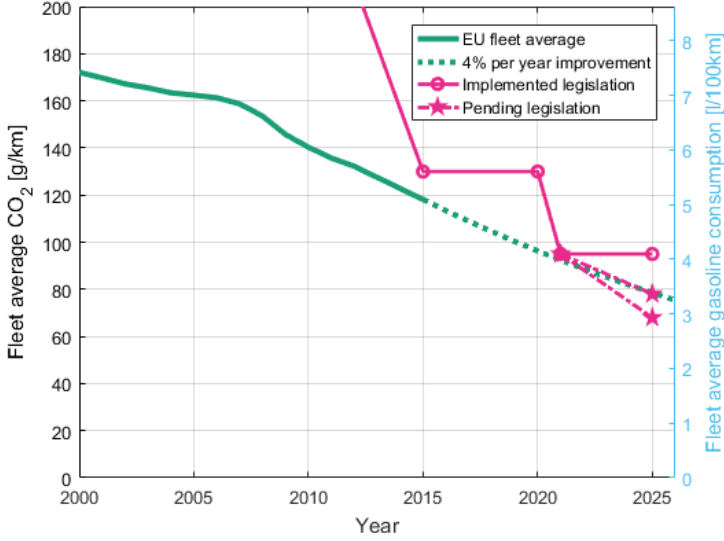


Figure 1.1: EU measured real emission levels and legislative targets. Data from[4].

on the majority of car models. Industry sources report a reduction in fuel consumption by 10%(PSA)[8], 13%(Continental)[9], 15%(Johnson Controls)[10] and (Kia)[11], 17% (Schaeffler and Continental)[12] through the implementation of a 48 V mild hybrid system. CO₂ emissions are generally proportional to fuel consumption when disregarding transient operating points[13]. Figures ranging from 7 g/km to 15 g/km (PSA)[8] and (Hella)[14] up to 30 g/km (ALACD and CPT)[15] in emission reduction are reported. All of those numbers are estimates and, unfortunately, the reference drive case are not declared properly in the sources mentioned.

Increasing the voltage level in light vehicles was suggested before in the mid 1990's to cope with the ever increasing electrical loads from convenience functions and drive support electronics. An enhanced voltage bus at 42 V was announced[16], but it never gained momentum in the car industry. The 48 V voltage level was proclaimed by the German automotive organization Verband der Automobilindustrie (VDA) in 2011[17], and in the first few car models from Audi and Daimler rolled out equipped with 48 V mild hybridisation in late 2018.

A complete 48 V hybrid system is a complex mechatronic system containing several new components, or new versions of previously familiar components, for the automotive market. Time-to-market is critical, and model based development (MBD) is used to replace intermediate verification steps involving hardware design and testing of subsystems. However, MBD requires virtual models with fair and known accuracy. Also important, the models need to be straight-forward to plug into and execute efficiently in existing large virtual vehicle models. The virtual models can be used both to estimate the electrical and thermal performance before any hardware systems are built, and the same models can also later be used to estimate sub-system performance while running on-line in the vehicle ECUs.

The first generation of 48 V hybrids typically replace the classical 12 V belt-driven generator with a higher-power density machine at 48 V designed for ca 10 kW peak power (P0 or P1 position, see Chapter 2), together with a small 0.2-0.5 kWh 48 V Lithium-Ion Battery (LIB) and a DC/DC converter. Such a system will be very limited in the amount of support it can provide in pure EV traction. The mentioned energy and power levels are confirmed by a study made by Hella[14].

The next generation of 48 V systems will likely use a purpose-developed, high-power-density, high-efficiency electric machine positioned inside or adjacent to the gearbox (P2, P2.5, P3), enabling it to offer enhanced brake re-generation and even some amount of pure EV driving capability. Even rear axle electric drives are relevant (P4 position). Peak power levels of 20-50 kW are needed to offer sufficient hybrid functionality. The electric machine, or machines, used here will likely have more in common with what is today used as traction machines for EVs, rather than a 12 V generator which serves as the reference in generation one. Very few car models on the market are equipped with a P2 or more advanced 48 V solution at the time of writing this thesis. With 20-50 kW and a LIB of 0.5-1.5 kWh, the performance numbers are matching mainstream non-plug-in hybrids such as Toyota Prius and the same gains in fuel efficiency can be achieved. The market penetration of 48 V mHEVs in cars is expected to be larger than for all other electrification topologies (PHEV, HEV, EV) combined for the upcoming two decades.

1.2 Review of previous work

As the 48 V voltage bus is a new design in the light vehicle sector, there is not a long history of previous work within this topic, where components and systems are specifically designed for high-power density and high efficiency. Some amount of publications are available on prototypes for 42 V systems from the 1990's.

The following sections present a review of work done with heavy emphasis on clear experimental results for electric machines, power electronics and battery testing.

System Studies

The engineering firm Ricardo[18] establish benefits of mHEV based on the contribution from each mHEV specific support function. All relevant mHEV topologies are presented together with power histograms, and challenges and opportunities with each topology. However, no experimental verification is performed. The same company presents a full-vehicle demonstrator with an advanced mHEVsystem called HyBoost[19], claiming an experimentally verified 40% reduction in emissions; down to 99.7 g CO₂/km for a Ford Focus sized car. This is done by ICE downsizing, start-stop, re-gen, EGR and e-supercharger. Although impressive results, the mHEV components are not based on 48 V technology and the implications of using different drive cycles are not presented.

Electric Machines

A range of custom-designed electric machines can be found in literature. Below is a selection of machines designed for automotive usage, with a power range of 5-150 kW, with either high power density, high efficiency, or a novel cooling layout as a design goal. The net power density of the machines will be highlighted, meaning peak mechanical output (ca 10 s) divided by volume of the smallest cylinder that encloses the active iron of the machine.

An automotive e-Assist ISG 115 V_{DC} hairpin stator winding induction machine is designed and tested by representatives of General Motors in [20]. 15 kW peak power is reported at an stack volume of 1.14 l, yielding a net power density of 13 kW/l. A peak efficiency of 88% is observed through mea-

surements.

The design and testing of a 6-phase, 48 V, 9 kW induction machine with hairpin windings is presented in [21], [22]. It features water jacket cooling designed for 5 l/min. Maximum mechanical output power is 9.0 kW at 3400 RPM, however, the only reported efficiency point is 85.3% at 2860 RPM, 21 Nm (5.8 kW mechanical). The net and bulk power density at 9 kW is 2.84 kW/l and 9.28 kW/l respectively.

Engineers from Ricardo presents the design and construction of two versions of 15 kW, 150 V PMSMs for mHEV [23]; one surface-mount PM (SPM) and one interior-PM (IPM) machine. Peak system motoring efficiency, including inverter, of 86% and 88% is reported, and the experimentally verified net power density is 2.54 kW/l and 3.63 kW/l for SPM and IPM respectively.

A high-speed, hybrid excitation machine is designed, built and tested by ORNL [24], measuring about the same gross volume as the Toyota THS2 main traction machine [25]. The machine is tested showing a peak efficiency of 95%, and powers up to 42 kW, yielding a net and bulk power density of 15.4 kW/l and 3.89 kW/l respectively. The large difference in net and bulk power density could be explained by the extra volume needed for the wireless rotor excitation circuit.

Engineers from Mercedes-Benz [26] report on a automotive-grade, high-speed, oil cooled three-phase PMSM developed for 48 V mild hybrids in P2.5 or P3 position. It is specified at 28 kW peak for 30 s. The measured peak efficiency is 90.5% and the gross power density is 3.94 kW/l. Unfortunately, no geometry for the active stack length are available to calculate net power density.

Automotive, mass-produced electric machines are extensively tested by Oak Ridge National Laboratory (ORNL) in the US. One interesting reference example is the 2012 Nissan Leaf traction machine reported in [27], with an net volume of 4.66 l and a rated maximum power of 80 kW with 97% peak efficiency. Net power density is 17.2 kW/l. This machine serves as a reference for high efficiency and high net power density. However, no electromagnetic or thermal design features are discussed.

Another interesting reference machine is the 2004 Toyota THS2 main traction machine, also tested by ORNL [28], [29] and reported by Toyota [25]. The rated peak power is 50 kW and the net/gross volume is 4.76 l and 11.2 l respectively. This results in a net and gross power density of 10.5 kW/l and 4.46 kW/l, respectively. Peak efficiencies of 94% are measured.

The 2010 Toyota HSD-G3 main traction system is extensively tested in[29], at 60 kW maximum power, peak efficiency of 96%, resulting in net and bulk power density of 21.6 kW/l and 5.17 kW/l.

Benchmarking of the BMW i3 traction machine is reported in[30], [31], showing peak efficiency of 94%, power output of 125 kW, net and bulk power density of 20 kW/l and 9.2 kW/l respectively.

To sum up, what is rare or even missing in the literature is a report on the design of a electric traction machine with high efficiency ($>90\%$) and high power density (>15 kW/l net, >5 kW/l bulk) proven simultaneously by experiments in the power range of 30-50 kW. Even more rare is extra-low-voltage (<100 V_{DC}) designs. Several automotive high-power traction machines in production (BMW, Toyota, Nissan) do indeed fulfill these requirements, but the performance are reported from third-party benchmarking, leaving out all comments on the design procedures from the engineering teams.

Power Electronics

In [32], a direct-water-cooled, high-current three-phase 48 V inverter board using aluminum substrate PCB and six paralleled high-current 100 V MOSFETs is experimentally evaluated. While dimensioned for 300 A_{RMS}, the maximum current achieved in tests was 150 A_{RMS} due to thermal limitations in the DC capacitor bank, and voltage spikes during switching. The measures of active components are 150x115x15 mm.

A custom made 48 V inverter with direct-oil cooling is presented in[33], and tests with phase currents up to 431 A_{RMS} at 17 l/min oil flow. The total volume for the automotive encapsulated inverter including controller is 13.4 l. No efficiency numbers are reported.

A compact, three-phase, two-level, water-cooled 48 V inverter in[34] is tested for peak performance at 55 V_{DC}, achieving 93.9% efficiency at a three-phase output of 210 A_{RMS}, 10.3 kW, $\cos(\phi)=0.75$.

US ORNL presents a modular (6-leg) converter topology in[35], and evaluates the losses for three different SiC MOSFET models operating at 30 kHz water cooled at 10 l/min. The system is aimed to power a 360 V_{DC} BMW i3 electric machine at 125 kW peak. The modular 6-leg setup uses carrier wave phase shift to minimize the DC capacitor current ripple. The ripple minimisation effect is not quantified, and the resulting inverter efficiency is not explicitly declared.

In[30], it is claimed that the next-generation of automotive inverters for HEVs are likely to use multi-level inverters, or *segmented* inverters, meaning several sets of three-phase VSI powering one electric machine equipped with open-ended windings. This topology would be an effective method of reducing the maximum current per phase leg, and minimizing the ripple voltage at the DC bus, reducing the size of the DC capacitor.

What is lacking in the literature is design and successful testing of compact, high-power-density (i.e. liquid cooled) extra-low-voltage ($<100\text{ V}_{DC}$) motor converters for multiphase electric machines in the power range ($>10\text{ kW}$).

Drive Systems: EM and PE

In[36], Engineers from Mahle present a 48 V rear-axle drive unit (P4 position) with a 30 kW peak, high-performance EM and integrated power electronics. A peak EM efficiency of 97% is reported (calculated). The highly integrated, water cooled MOSFET inverter is designed for 600 A_{RMS} continuous. The importance of effective cooling is highlighted for both PE and EM, but no quantification is provided. However, no further design results, e.g. power density, or efficiency measurements are reported.

In[34], [37], [38], a water-cooled 48 V, 10 kW (peak 30 s) Electrically-Excited Synchronous Machine (EESM) machine and inverter system is designed, build and experimentally verified. While the inverter tested up to 371 A_{RMS} , the machine achieves 34 Nm at 750 RPM, yielding 2.7 kW. The prototype machine efficiency is limited to 47% at 2.7 kW, and peak 62% at 0.3 kW output according to measurements in[37]. The net power density for the electric machine, using active stack length and diameter, excluding the excitation system, equals to 11.0 kW/l (30 s design target) and 3.0 kW/l verified.

The very-low-voltage asynchronous traction machine ISCAD is presented in[39]. The design target for both machine and integrated inverter is $<60\text{ V}_{DC}$, 240 kW[40]. However, no experimental figures for output power or efficiency are provided. Further ISCAD experiments are presented in [41], but without any experimental results to indicate power density or efficiency.

An Integrated Modular Motor Drive (IMMD) is presented in[42], where a five-phase tooth-coil wound machine with key winding factor one (one adjacent coil per phase) is offering the possibility of controlling each individual coil with one small inverter board. A prototype is built and powered, and a hypothetical net power density for the machine of 1.71 kW/l at 2.7 kW is reported. A GaN

IMMD is also built for 2x100 V operation[43], but only one open-loop test at ca 500 W is reported. More concepts and prototypes are built of the IMMD, but no further high-power operating points can be found in the literature.

A version of the IMMD, from another research team, for an axial-flux 48 V PMSM is presented in[44]. The effects of using carrier wave interleaving to minimize DC current ripple is mainly evaluated. The tests are performed up to 4 kW, which means net power density of 2.58 kW/l with size numbers reported from[45].

Continental are presenting production-ready water-cooled Belt-ISG components for 48 V mHEV applications[46], with a 5 s peak gross power density of 3.18 kW/l including power electronics and motor control.

The EU project ECOCHAMPS has reported by Ricardo UK on the design and testing of components for 48 V hybrids. One example is a pseudo 6-phase, oil spray cooled electric machine[33], [47] with hairpin windings, designed for 25 kW and tested up to 15.5 kW output power. An oil flow of 2 l/min is preferred by design. The net power density is 17.0 kW/l by design target, and 10.5 kW/l validated experimentally. No efficiency numbers are reported.

Battery modeling

A short overview of empirical modeling is presented in Paper 1 , and a more comprehensive overview in Paper 4. At the start of the thesis work, a lack of examples was identified in the literature on how various testing methods for LIB leads to extraction of parameters for linear circuit models which then are evaluated in load cycles relevant for vehicle use. Further on, most reports on battery modeling only apply a proposed model to one specific make, model, size and chemistry of LIB.

1.3 Purpose of thesis

System design, component modeling, and component interactions in a high-performance 48 V mild hybrid electric powertrain is the main focus in this thesis. Electrical, thermal and electromagnetic properties are to be studied for the main propulsion components: LIB and EM. Accurate electrical and thermal models are crucial to maximise the utilisation of LIBs. Novel design features for high efficiency, high power density EMs are also to be explored. Relevant test procedures available within the project was electrochemical Impedance Spectroscopy (EIS) and high-current pulse charge and discharge.

Two main research questions have been followed throughout the work presented in this thesis:

- How can model based design be used to represent high-performance LIBs of various sizes, performances and chemistries?
 - What model accuracy can be established using EIS and pulse discharge when characterizing the electrical and thermal performance of LIBs?
 - What accuracy can be achieved using simple Thevenin models to represent the electrical behavior in LIBs over a wide operating range in SOC, temperature and current range?
- Design and construction of an electric machine concept that is promising for mHEVs, featuring a power output of at least 20 kW, high efficiency and high power density.
- Demonstration of compact and efficient power electronics hardware to allow for tight integration on the electric machine concept.

1.4 Thesis outline and methodology

This thesis consists of a summary of eight papers, of which six are peer-reviewed and accepted at the time of print on this thesis. To give a context and understanding of the work, additional theory and history is outlined in Chapter 2, and the setup in Chapter 3. Highlighted results from papers, as well as previously unpublished results from the thesis work, are presented in Chapter 4.

1.5 Contributions

The following list of contributions are claimed:

- Development, and extensive applications, of a high-current, portable, robust, easy-to-use, and very-high-accuracy test methodology for LIBs that works across many cell sizes, cell types and various test equipment.
- Applying and quantifying the difference in accuracy between high-current pulse discharge measurements with low-current electro-chemical impedance spectroscopy as methods to extract equivalent circuit parameters for LIBs.
- Development, verification, of accuracy for a high-accuracy empirical electrical model for LIBs, including publication of the parameter results. The model is optimized for use in model-based vehicle drive cycle simulations, using only a limited number of linear electrical standard circuit elements. Very low average voltage error is shown compared to literature.
- Development and verification of a lumped-parameter electro-thermal model for LIBs including reversible entropy heat, and development of a test method to parameterize the entropy coefficient. This 1D LPN significantly increases the temperature accuracy in LIB models.
- Experimental measurements of fuel consumption with a prototype car equipped with a 48 V mild hybrid system, and validation of a simulation model to emulate the mild hybrid powertrain behavior.
- Categorization, classification and visual presentation of the most important electromagnetic properties of double-layer, three-phase tooth-coil wound machines in a comprehensive way not previously found.
- Design, deployment and calibration of a customized calorimetric test system for low-viscosity oils as the main coolant, and water as the secondary coolant medium.

1.6 List of Publications

This thesis is based upon the following papers:

- I *Parameterization of Equivalent Circuit Models for High Power Lithium-Ion Batteries in HEV Applications*
Conference paper presented 2016-09-06 at
EPE2016, Karsruhe, Germany
- II *Electro-Thermal Modeling of High-Performance Lithium-ion Energy Storage Systems Including Reversible Entropy Heat*
Conference paper presented 2017-03-27 at
APEC2017, Tampa, Florida, USA
- III *Experimental and model based evaluation of mild hybrid fuel consumption gains and electric machine utilization for personal vehicle application*
Conference paper presented 2017-08-08 at
ITEC-AP2017, Harbin, China
- IV *Parametrization of Linear Equivalent Circuit Models over Wide Temperature and SOC spans for Automotive Lithium-Ion Cells using Electrochemical Impedance Spectroscopy*
Published 2017-09-22 in Elsevier Journal of Energy Storage
- V *Pole-Slot Selection Considerations for Double Layer Three-phase Tooth-Coil Wound Electrical Machines*
Conference paper presented 2018-09-03 at
ICEM2018, Alexandroupoli, Greece
- VI *Design and Verification of In-slot Oil-Cooled Tooth Coil Winding PM Machine for Traction Application*
Published 2020-04-07 in IEEE Journal of Industrial Electronics
- VII *Electromagnetic and Calorimetric Validation of Direct Oil Cooled Tooth Coil Winding PM Machine for Traction Application*
Submitted 2020-05-17 to MDPI Energies
- VIII *Manufacturing of in-slot cooled tooth coil winding PM machines*
Conference paper submitted to ICEM2020
(2020-08-23, Gothenburg, Sweden)

CHAPTER 2

History and theoretical framework

2.1 Short history of electrification

In the end of the 1800's, the vehicle fleet consisted of a mix between horse carriages, steam engines, electric vehicles and internal combustion engines (ICE). The competition between the different propulsion technologies was even, but within two decades in the start of the 1900's, the availability of gasoline and the advancements in the ICE made both horses and electric vehicles obsolete. Hybrid electric vehicles (HEVs), a powertrain where one or several electric machines cooperate with a combustion engine, also existed to a small degree, more history on this can be read in [48]. The start of mass-produced hybrid electric powertrains was probably when Ford introduced the option of an electric starter motor, battery and generator to the Model T in 1919. The starter motor did only support with power to start up the combustion engine, to alleviate the driver from the burdensome task of hand-cranking. Unfortunately, the level of electric hybridisation remained on a very low level for the next 80 years until late 1990s, when Honda introduced *Integrated Motor Assist* and Toyota introduced the *Hybrid Synergy Drive* on several car models. The first series produced 48 V mild hybrid electric vehicles

(mHEVs) were sold in 2018, and they quickly gained popularity. It is predicted that 48 V hybrids will dominate by quantity in the light vehicle market over HEV and EVs for the next two decades[17].

2.2 Levels of electrification

One way of categorizing the level of electrification in the vehicle powertrain is to look at the quota between installed electric peak power (P_{EM}), and total peak power from both electric machine and ICE (P_{ICE}) and call it the electrification factor, expressed as

$$e_f = \frac{P_{EM}}{P_{EM} + P_{ICE}} . \quad (2.1)$$

If this factor is 1, the car is purely electric. In the lowest range of e_f for modern cars we find an example of $e_f=0.01$; a 1 kW starter motor and a 99 kW ICE. Mild hybrids as a concept has the opportunity to fill a gap of electrification factor between 0.05-0.5. Fig. 2.1 shows the connection between vehicle traction voltage, electrification factor and expected electrification features.

2.3 Hybrid topologies

The electro-mechanical part of a 48 V mild hybrid powertrain can be formed in many ways. For cost and size reasons, the most common solutions will be restricted to one electric machine situated within a classical mechanical powertrain where it provides the most beneficial effects. The automotive industry has united around a vocabulary of how the electric machine installation can be done, as illustrated in Fig. 2.2. The hybrid topologies are further presented in [17] and [18]. In this thesis, P0 and P2 are compared in Paper 3. The electric machine presented in Paper 6-8 is powerful enough to cover all positions (P0...P4).

2.4 Why 48 V?

The International Organization for Standardization (ISO) defines safety levels for automotive applications in ISO6469-1[49], which is legally binding for light

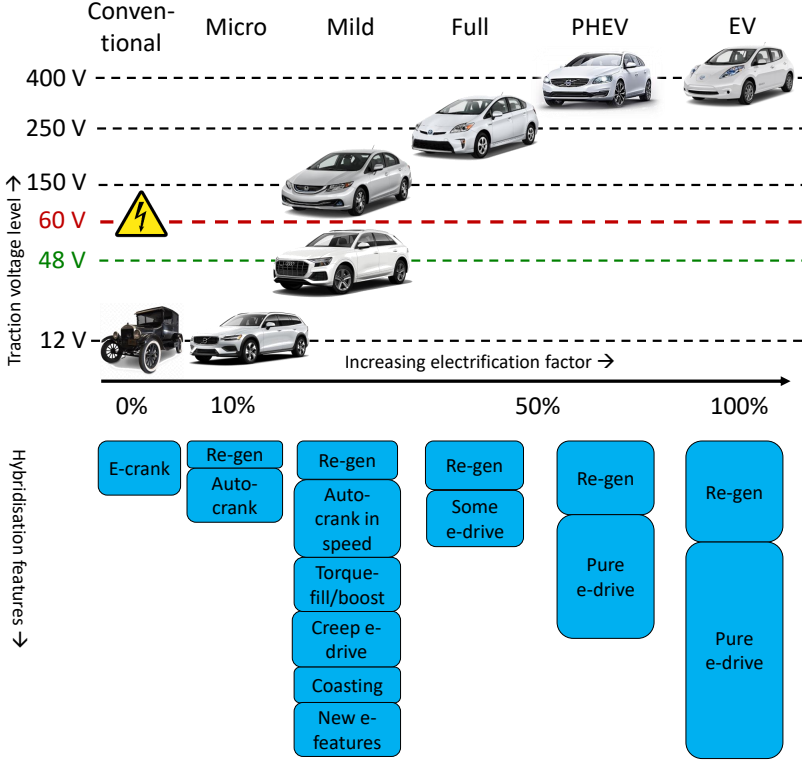


Figure 2.1: Features, voltage levels and electrification levels.

road vehicles by UN ECE R100[50]. The limit is fixed at $60 V_{DC}$ or $30 V_{AC}$ and components and subsystems operating above this limit are labeled class B voltage systems. Class B systems explicitly require proper galvanic isolation from driver, passengers and service personnel, which must be realized through a list of mandatory safety features. Below the limit, e.g. $<60 V_{DC}$, is labels Class A and implies none or few mandatory safety measures in order to protect humans from electric shock. However, regardless of voltage level, the hazard of current induced phenomena such as arc and burning still prevails which motivates at least a basic protection layer with regards to electrical safety. The exact range of voltage to be used for automotive 48 V systems are standardized through VDA320[51] (published in 2014), formerly known as L148, as well as

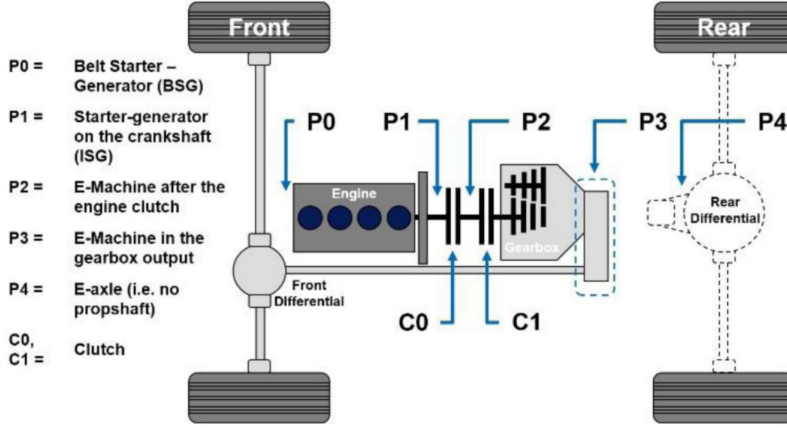


Figure 2.2: The five viable electric machine topologies for mHEVs (P0..P4). Courtesy of[33].

through ISO21780[52] (standard under development). An example of allowed voltage range is illustrated in Fig. 2.3.

For stationary applications, slightly different voltage limits and naming are defined compared to automotive applications. According to IEC60364[53], *extra low voltage* is all systems $<120 V_{DC}$, and according to EU Low Voltage Directive[54] $<75 V_{DC}$ means *extra low voltage*.

Up until the standardization of 48 V in the last few years, all successful hybrid electric vehicles on the market have utilized a class B voltage system, usually utilizing a traction voltage in the range of 150-400 V_{DC} . The class B system requires substantial protective measures which adds complexity, weight, volume and hence cost to all solutions associated with the class B voltage bus. By limiting the system voltage to 48 V, cost, size and weight can be kept at competitive levels.

2.5 Battery modeling

Electrical and electro-thermal models for LIBs are usually either physics-based or black-box empirical based models. Very related to black-box approach is a hybrid model called "gray box", often represented by an electric equivalent

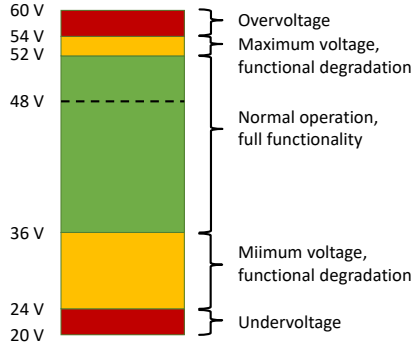


Figure 2.3: Allowed voltage levels for a 48 V system according to VDA320[51].

circuit model. The circuit elements and parameters are selected to match the observed voltage response from experimentation.

The most basic equivalent circuit model (ECM) for a LIB consist of a basic Thevenin equivalent: An internal voltage source with an internal resistance in series, see Fig. 2.6a. However, this model does not capture the time dynamics of most LIBs, even with parameters varying with temperature and SOC. If this basic circuit is to be used, it is important to specify at what charge or discharge time the resistance value is sampled. Common values are 1,2,5,10,30 s for automotive usage.

Regarding time dynamics to study, the scope is limited to what makes most sense to minimize the error within a single drive cycle. LIBs exhibit interesting effects in the frequency domain from 10 kHz and spanning down to period times of years (i.e. ageing). A typical drive cycle, such as WLTP, is 30 minutes long and is sampled in 1 s increments. If an FFT is performed on the drive cycle, most of the data intensity will be focused within a frequency window of $0.5 \left[(30 \cdot 60)^{-1} \dots 1 \right]$ Hz. This is visualized in Fig. 2.4. With this said, advanced ageing phenomena that arises despite obeying manufacturers' voltage and temperature limits, are not within the scope of this work.

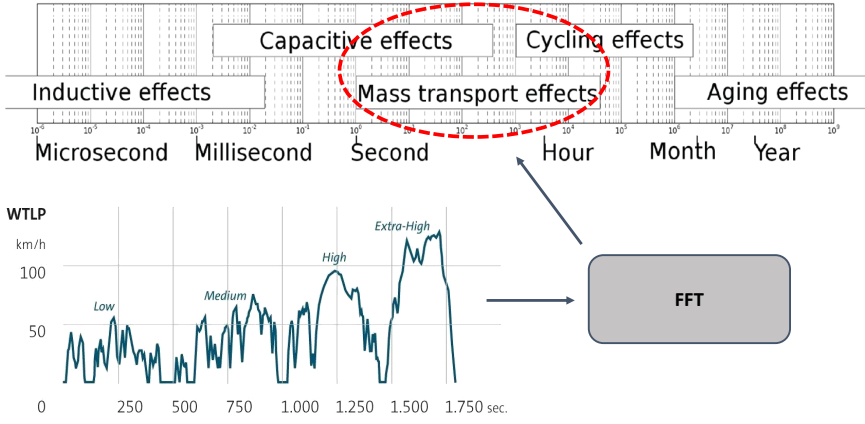


Figure 2.4: Means of selecting the most relevant time dynamics for equivalent circuits to be used in a drive cycle.

Equivalent Circuit Models

The fundamentals of electrical cell modeling usually presupposes a basic Thevenin equivalent circuit comprising only of an ideal voltage source and a resistance symbolizing the internal losses, see Fig. 2.6a. The circuit parameters should be mapped to operating points, such as temperature and charge level (SOC), to accurately represent the electrical behavior. The most obvious influence of charge level is the Open Circuit Voltage (OCV). The SOC is an internal battery state which cannot be directly measured. However, it can fairly accurately be estimated by a combination of integration of the current and estimating the OCV on-line and then map the OCV to the SOC. Examples of how the OCV depends on SOC can be seen in Fig. 4.3.

In the scope of this work, OCV is modeled with look-up tables as a function of SOC. The dependence of temperature in the OCV is very small and not critical for electrical performance modeling as long as the SOC value is normalized for temperature[55]. However, for thermal modeling, the entropy effect is defined by the change of OCV over temperature, as discussed in Paper II.

The second current dependent dynamics to capture in ECMs, is a significant reactance displayed by LIBs when they are exposed for large changes of charge, for example a regenerative braking event in a mHEV. The phenomena

is referred to as *charge diffusion*[56], [57] or *mass transport*. Diffusion typically increases the reactance in the negative direction proportionally to the decrease in frequency of current excitation; the battery behaves as a pseudo-capacitor for low frequencies. The behavior can be accurately modeled by the non-linear Constant Phase Element (CPE)[58] parallel connected with a linear resistor. The CPE represent an impedance of

$$Z_{CPE} = Q^{-1}(j\omega)^{-n} , \quad (2.2)$$

where Q is a pseudo-capacitance (F), j the imaginary operator, ω angular frequency (rad/s), and n is a unitless real scalar in the range of $[0 < n < 1]$. When the CPE is parallel connected with a resistor (R), it forms a Zarc element with the impedance

$$Z_{Zarc} = \frac{R}{1 + RQ(j\omega)^n} = \left(R^{-1} + Q(j\omega)^n \right)^{-1} . \quad (2.3)$$

A special case of the Zarc element is defined at $n=0.5$; the Warburg element, which is often used to model diffusion[56], [57]. The behavior described by (2.2) and (2.3) are crucial to the scope of Paper 3. A challenge with Zarcs is that they cannot be realized in the time domain, they have no direct inverse frequency transform. The most effective way to use them in a time-domain simulation (such as a car drive cycle simulation), is to approximate them with several series connected RC links. In[59], it is suggested that 5 series connected RC links are used to represent a Zarc element. An EIS measurement of a automotive LIB is shown in Fig. 2.5 where six RC elements are used to capture the capacitive behavior. An even more simplified ECM suggested in this thesis is to further limit the number of RC groups to two, as seen in Fig. 2.6b. This can be done without sacrificing much of the model accuracy in the frequency range 10 mHz to 10 Hz. An important condition to fulfill is that the value of the two time constants ($\tau = R \cdot C$) are clearly separated. A thorough explanation of how the RC links are mathematically modeled is found in Appendix A.

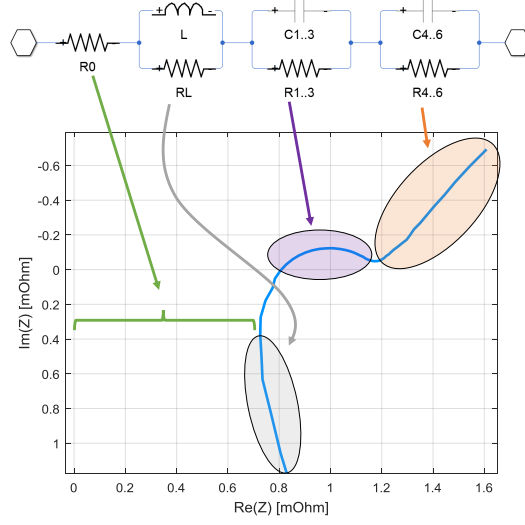
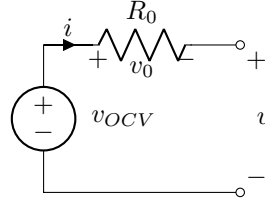
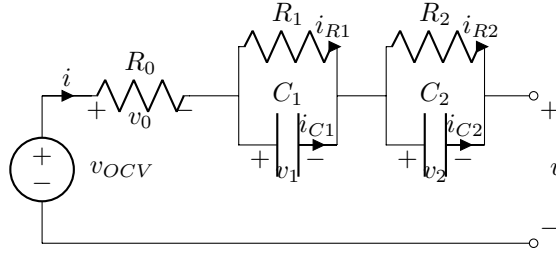


Figure 2.5: Example of reproduction of impedance from EIS measurements using only linear ECMs. Results from cell H from Table 3.1 at 25°C.



(a) Simple R_0 Thevenin ECM.



(b) Extended R+2RC Thevenin ECM.

Figure 2.6: Reference ECMs for LIBs.

2.6 Electric machine

Winding layout

TCWMs can be designed in many high-performance configurations. Paper 5 lays out the theory of key performance indices (KPIs) for three-phase balanced windings, which is briefly summarized in Table 2.1.

Table 2.1: Summary of TCWM key performance indices

Symbol	Name	Explanation
Q	Slot number	Number of total slots in stator
p	Pole number	Total number of rotor poles ($2 \cdot$ pole pairs)
q	Slots per pole per phase	
t	Periodicity	Number of symmetric or anti-symmetric repetitions of the stator winding layout in one mechanical revolution
W	Key winding factor	Number of consecutive teeth coils connected in series to form the smallest coil group
M_f	Cogging multiplier	Multiplication of cogging torque frequency versus electrical frequency due to stator layout
k_w	Winding factor	Linking factor between coil group current and stator induced MMF
δ_σ	Harmonic air gap leakage factor	Excessive stator inductance due to magnetisation of MMF sub- and super-harmonics over the air gap

Equivalent circuit for electric machine

A standard way of modeling a three-phase electric machine is to transform all variables to the dq reference frame. The output torque of the machine can be expressed as[60]

$$T = n_{ph}n_p \left(\Psi_d i_q - \Psi_q i_d \right) , \quad (2.4)$$

where Ψ (Wb) is RMS flux linkage, i (A) is RMS stator current, n_{ph} number of phases, and n_p pole pair number. The flux linkages for a permanent magnet rotor including saliency are expressed as

$$\Psi_d = L_d i_d + \Psi_{PM} \quad (2.5a)$$

$$\Psi_q = L_q i_q, \quad (2.5b)$$

where L_d and L_q (H) are the equivalent stator inductance in d and q direction respectively. Ψ_{PM} (Wb) is the RMS linked flux between rotor permanent magnet and stator coils of one phase. Linked flux can be established either by the use of FEA or experimentally for a prototype machine. A reformulation of (2.4) can now be done using (2.5), highlighting reluctance torque production through the term $(L_d - L_q)$:

$$T = n_{ph} n_p \left(\Psi_{PM} i_q + (L_d - L_q) i_d i_q \right). \quad (2.6)$$

The ECM for RMS phase voltages u (V) can be defined as in Fig. 2.7, where stator phase resistance R_s (Ω) and rotor electrical speed ω_e (rad/s) compiles to

$$u_d = L_d \frac{di_d}{dt} + R_s i_d - \omega_e L_q i_q \quad (2.7a)$$

$$u_q = L_q \frac{di_q}{dt} + R_s i_q + \omega_e (L_d i_d + \Psi_{PM}). \quad (2.7b)$$

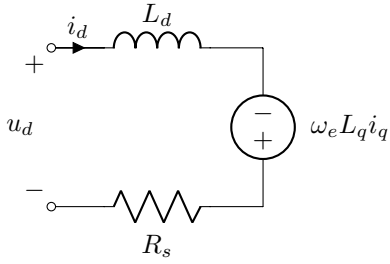
The mechanical speed ω_m scales with the electrical speed with the number of pole pairs:

$$\omega_e = n_p \omega_m. \quad (2.8)$$

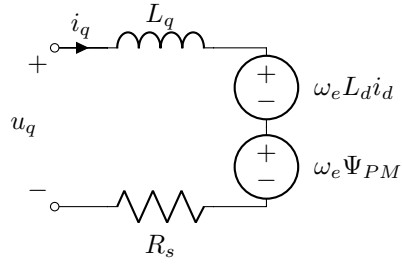
For steady-state operation, the terms containing $L \frac{di}{dt}$ can be neglected. For a special case of no-load ($i_d = i_q = 0$), steady-state ($di/dt = 0$, $d\omega/dt = 0$) rotation, the relation between total stator output voltage, electrical speed and linked permanent magnet flux can be derived from (2.7b) as:

$$u_s = \omega_e \Psi_{PM}. \quad (2.9)$$

This relation is very useful during experimental establishment of permanent magnet linked flux under no-load conditions.



(a) Direct voltage ECM



(b) Quadrature voltage ECM

Figure 2.7: Equivalent Circuit Models for electric machine in dq frame.

CHAPTER 3

Case Setup

In this chapter, the boundary conditions and hardware used for LIB, power electronics, and EM testing is discussed.

3.1 System assumptions

Even though a Electrical Energy Storage System (EESS) consists of many electrical components, focus in this work has been on modeling the individual LIB cells, since they are the most influential components on the ESS performance. The assumption is that a single-cell electro-thermal model can easily be scaled to system level by a combination of series and parallel connection of many cells. With this said, it is assumed that the parameter spread between cells, for example from production, is negligible. It is also assumed that the EESS is free from thermal gradients that will induce a spread in parameters between cells and the EESS. For each cell model, tests are performed on one or a few specimen with the assumption that the parameter spread is negligible.

3.2 Battery testing

Parameters for a R+2RC equivalent circuit presented in Chapter 2 are extracted for numerous different LIB models. Most tests are done in room temperature (20-24°C), while some cells are tested more extensively over a temperature span from -10°C to +60°C with the help of a temperature chamber. The first batch of cells (C through G) is acquired from the open market in 2015. About the same time, the first cells for a Formula Student project at Chalmers became available for measurements; cell A & B. Also, the Automotive cell H was borrowed from a adjacent research project in the same lab. In 2017, a batch of new automotive, high-performance, very high power density cells from leading cell manufacturers was made available for measurements (M,N,S,T). Many different cell types, in various formats, and various chemistries are evaluated using the same test and characterisation strategy with the goal of evaluating if the same strategy an electrical model can successfully be used generally. Table 3.1 summarizes the main properties of tested cells and Fig. 3.2 shows pictures of some of the cells. The cell chemistry is a qualified guess in most cases, as it is rarely disclosed in or outside datasheets. The energy density U_m and specific energy e_m are derived by measuring the available energy at room temperature during 1 C charging. Weight and volume are also measured by own means. The test current is normally 5 C discharge current as the target application requires 5-30 C in peak discharge and charge. Please note that the naming of the cells in Table 3.1 is not consistent with the naming in Paper I and Paper IV. However, all cells tested in all papers are listed in Table 3.1.

Test equipment

For the first few years of pulse testing, a Digatron BTS-600 battery tester is used. In the latter part of this project, a PEC ACT 0550 was available in the lab. The test procedure and post-processing are adapted to work with this equipment. All EIS measurements are made with a Gamry Reference 3000. The test procedures are illustrated in Fig. 3.1. For iso-temperature tests, the thermal chamber ILW53 from Pol-Eko is used.

Table 3.1: Overview of tested LIBs and their basic parameters.

Test object	Brand	Form Factor	Chemistry	Q_{nom} (Ah)	V_{max} (V)	V_{min} (V)	I_{test} (A)	U_m (Wh/dm ³)	e_m (Wh/kg)
A	Melasta	Pouch	LCO/G	10	4.20	3.00	50	447.5	180.6
B	EP	Pouch	LCO/G	10	4.20	2.75	50	444.5	182.7
C	Tinkang	Pouch	LMO/LTO	20	2.75	1.60	100	-	-
D	Tinkang	Pouch	LMO/LTO	15	2.75	1.60	75	128.9	64.6
E	Tinkang	Pouch	LMO/LTO	26	2.75	1.60	130	151.8	67.2
F	Tinkang	Pouch	NMO/LTO	26	3.30	2.00	130	151.7	-
G	Tinkang	Pouch	NMO/LTO	28	3.30	2.00	140	171.7	78.3
H	-	Pouch	(NMC+LMO)/G	26	4.15	2.80	130	345.7	169.6
I	A123	Pouch	LFP/G	19.6	3.60	2.00	98	-	-
M	-	Prismatic	(NMC+LMO)/G	5.0	4.20	2.80	25	230.8	106.6
N	-	Pouch	NMC/LTO	11	2.70	1.50	55	161.5	67.4
J	Melasta	Pouch	LCO/G	7.5	4.20	3.00	37.5	505.7	193.8
S	SKC	Pouch	(NMC+LMO)/G	10	4.30	2.50	50	178.0	101.1
T	Toshiba	Prismatic	NMC/LTO	20	2.70	1.50	100	177.0	90.0

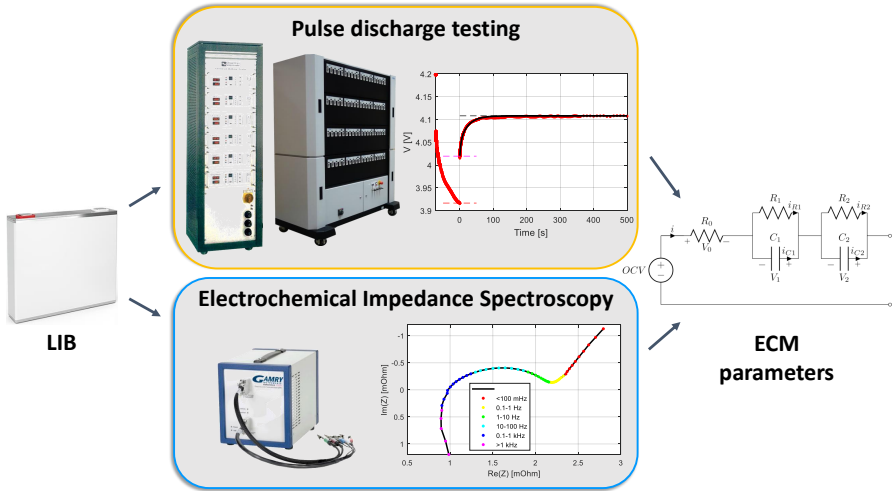


Figure 3.1: Visualisation of the two utilized test methods and used equipment for high-power LIB testing.



Figure 3.2: Pictures and CAD models of a selection of cells, with labels matching Table 3.1.

3.3 Inverter test setups

Two high-current inverter prototypes are built within the project. Both are three-leg, two-level topologies with silicon MOSFETs and high-capacity multi-layer ceramic capacitors. Inverter 1 is depicted in Fig. 3.4, and Fig. 3.5. More details on the design and testing of inverter 1 can be found in [61]. Inverter 2 can be seen in Fig. 3.7, and more details are presented in [62]. A brief of the design and the achieved results is summarized in Table 3.2. The common design features for both inverters are to use high-performance, 100 V, low- $R_{ds,on}$ MOSFETs with low switching losses to enable 100 kHz PWM switching frequency (f_{sw}), as opposed to normal f_{sw} for automotive traction machines of 5-20 kHz. With the increased f_{sw} , a smaller capacitor bank can be used due to the small time duration energy need to be stored between switching events. The switching losses are still a fraction of the conduction losses for these types of MOSFETs. Water cooling is used to limit the temperature rise of the MOSFETs, which is necessary to operate close to the rated datasheet current. To enable high f_{sw} , a robust, well-integrated gate drive is needed. During the design of inverter prototype 2, a miniaturized, modular phase leg gate drive card was designed, see Fig. 3.6, based on Texas Instruments UCC27201 gate drive chip and other lessons learned from previous inverter designs. All inverter prototypes are controlled open-loop with the 32-bit microcontroller TMS320F28379D from Texas Instruments, and programmed through Matlab Simulink.

Table 3.2: Design features and test results for prototype inverter

	Prototype 1	Prototype 2
Design		
Topology	3-leg, 2-level	3-leg, 2-level
Target power	16 kVA	25 kVA
Cooling	Water	Water
Gate drive	Gen1 off-board	Gen2 miniature
PCB type	Dual layer	Single-layer 105 μ copper
PCB substrate	FR4	Aluminum
Target (f_{sw})	100 kHz	100 kHz
Transistor make	Infineon	Infineon
Transistor model	IPP045N10N3GXKSA1	IAUT300N10S5N015
Transistor package	TO220	HSOF-8-1
Transistor config.	1(2)p	2p
Transistor rating	100 V, 137 A, 4.5 m Ω	100 V, 300 A, 1.5 m Ω
Capacitor make	TDK	TDK
Capacitor model	C5750X7S2A156M250KB	C5750X7S2A226M280KB
Capacitor rating	100 V, 15 μ F	100 V, 22 μ F
Capacitor count	60	45
Test Setup		
Load type	3-phase coils reactive load	3-phase step-up transformer plus 400 V resistive loads

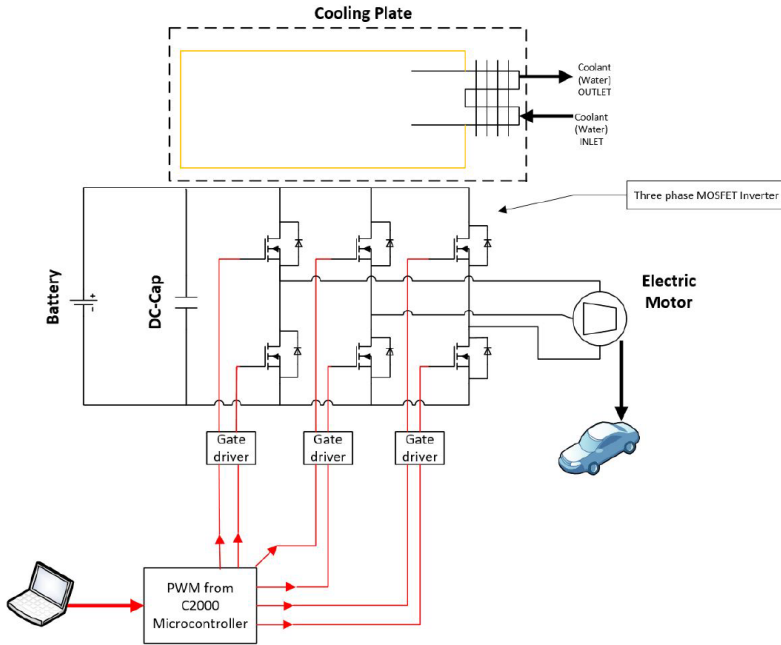


Figure 3.3: Test setup for inverter tests. The electric machine is represented by a high-current RL load or transformer. Courtesy of[61].

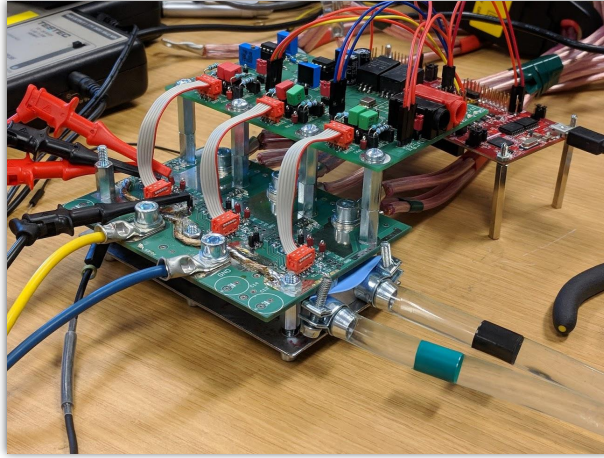


Figure 3.4: Picture of inverter 1 prototype, featuring water cooling and external gate drive board. The power board measures 120x90 mm.

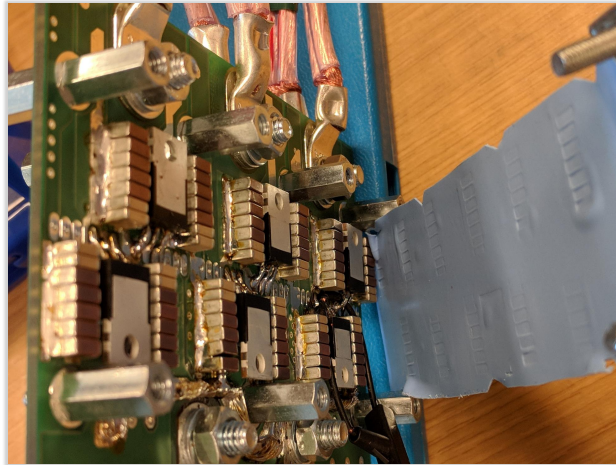


Figure 3.5: Bottom side of inverter prototype 1 board, where half of the dual parallel MOSFETs in TO-220 package are mounted. The water cooling covered by a silicon thermal pad is seen to the right, where footprints of both ceramic capacitors and MOSFETs can clearly be distinguished, telling good thermal contact.

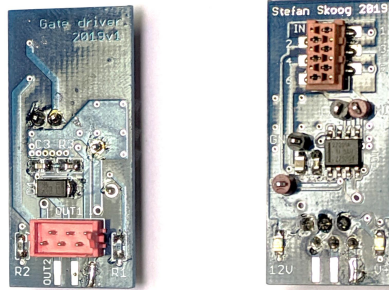


Figure 3.6: Picture of miniature, modular gate driver cards for one phase leg, measuring 8x39 mm.

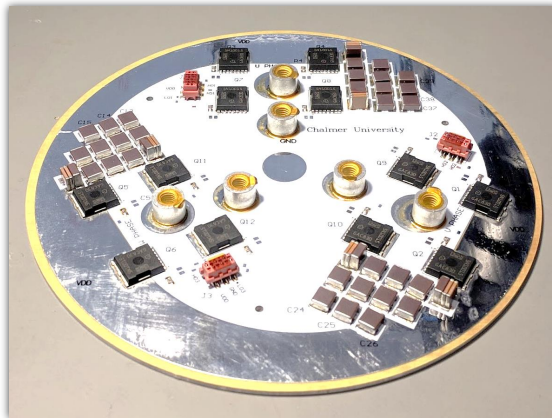


Figure 3.7: Picture of inverter 2 prototype, featuring aluminum substrate which allows for very effective water cooling. The diameter is 140 mm.

3.4 Electric machine setup

A TCWM is selected because of interesting properties of modularity, flexible manufacturing, possibility of in-slot cooling, high torque density, and high efficiency. A tooth-coil stator, when combined with a PM rotor, should preferably feature embedded magnets, in order to reduce the eddy current losses in the magnets caused by significant sub- and super-harmonics in the airgap magnetic wave. In this work, the selected rotor is a single-layer V-insert NdFeB magnet layout with the intention to offer a large saliency.

Winding layout

With the analysis from Paper 5, and the preference of using six or more open-ended windings, the most appealing slot (Q) - pole (p) combinations for this applications is Q12p10 and Q12p8. A comparison of iron losses in Paper 7 favors the Q12p10 layout. To acquire the optimal winding layout for this slot-pole combination, Cros' method is implemented as a Matlab script as described in [63]–[65] and then imported directly to Ansys simulation suite. Results can be seen in Fig. 3.8 and Fig. 4.9.

Electric machine test setup

A 6-phase, TCWM is designed with the intention to serve either as a traction machine for a small EV, or as an assist machine in a mHEV. The design specifications are presented in Table 3.3. CAD pictures of the general setup is shown in Fig. 3.10. The resulting design for the prototype ready machine is presented in Table 3.4. More on the design and assembly is found in Paper 8 and Fig. 3.11. The machine is tested in a dynamo setup reported in Paper 6-7. The winding layout is presented in Fig. 3.8, showing how twelve individual tooth coils are series connected in pairs, resulting in six open-ended phases available on the NDE. The six phases consist of two symmetrical three phase windings, making it possible to both series and parallel connect two coil groups for three phase operation. With the open-ended windings, phase windings can be formed externally by using either Y, Delta or individually powered coil groups. Three examples are shown in Fig. 3.9.

Efforts are made to identify the signal parameters in the ECM presented in (2.4) through (2.7). Each coil is measured individually for voltage and

resistance. For inductance, individual coils are measured and the rotor angle is varied slowly to scan for max and min values. The stator resistance is measured for each individual phase group consisting of two internally series connected tooth coils. An excitation current of 10.0 A DC is used while the voltage drop is measured at the machine terminals with a bench multimeter, see Fig. 3.12. The phase voltage at no-load is measured with an oscilloscope while driving the machine with an external dynamo at 1027 RPM, as shown in Fig. 3.12. The oscilloscope is set up to calculate the true RMS values. The power electronics and motor controller available for this motor setup is limited to 110 A RMS per phase, whereas the expected 10 s peak current for the machine is 600 A RMS. Torque output is measured up to the the maximum system current in 10 A increments and with a current angle of 90° advancement, i.e. i_q only.

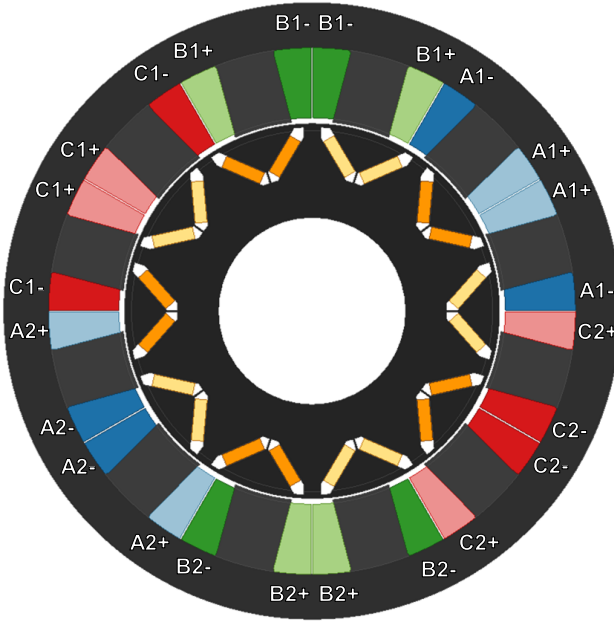


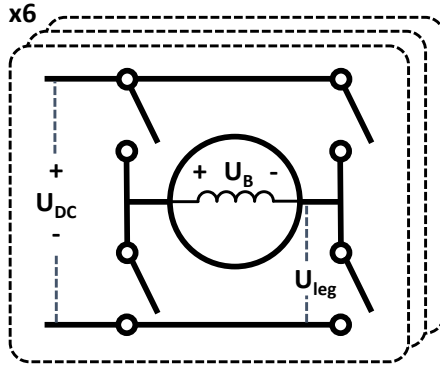
Figure 3.8: Geometry and winding overview of the designed machine.

Table 3.3: Electrical machine design specifications

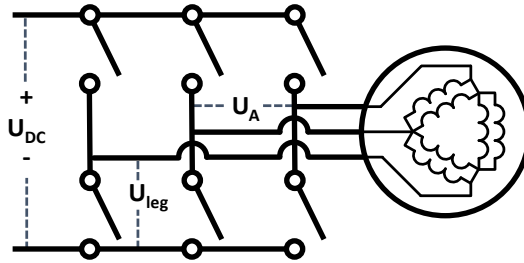
Quantity	Value	Unit
Peak torque	140	Nm
Peak power	50	kW
Base speed	3 600	rpm
Max speed	11 000	rpm
Coolant max temperature	60	°C
Max winding temperature	180	°C
DC bus voltage	48	V

Table 3.4: Geometric parameters for electric machine in 3-phase connection

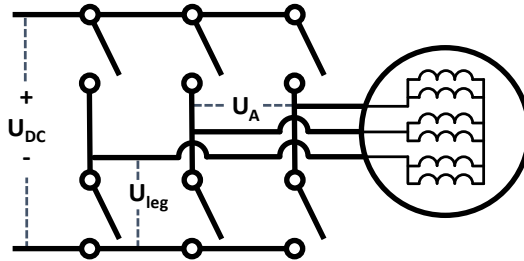
Quantity	Value	Unit
Outer Stator diameter	180	mm
Inner Stator diameter	111.4	mm
Airgap radius	0.7	mm
Active length	100	mm
Tooth width	17	mm
Stator Yoke width	13	mm
Magnet thickness	3.5	mm
Conductor diameter	1.5	mm
Parallel conductors per turn	9	-
Turns per coil	3	-
Number of phases	6	-
Max. phase RMS current	600	A
Max. peak current density	35	A/mm ²
Hard iron remanent flux	1.31	T
Hard iron type	Vacodym 745DHR	-
Soft iron type	M235-35	-



(a) Six phase single coil groups connection



(b) Three phase, parallel coil groups Delta connection



(c) Three phase, parallel coil groups Y connection

Figure 3.9: Examples of electrical configurations of machine and two-level inverter.

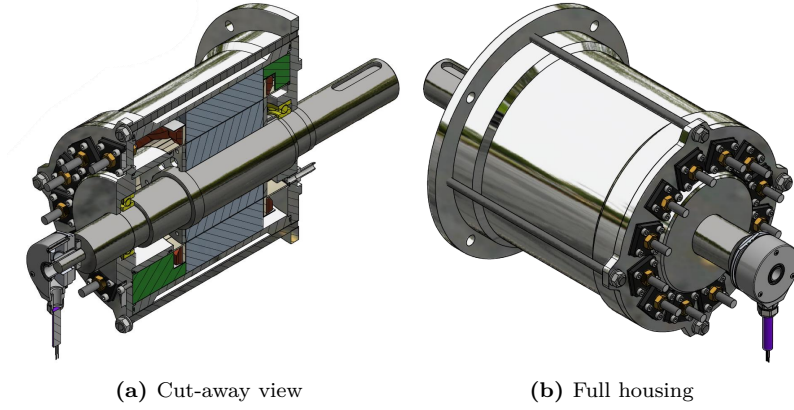


Figure 3.10: CAD pictures with cut-away of the prototype EM. Length: 100|223 mm stack|total. Diameter: 180|206 mm stack|outer.



Figure 3.11: 48 V machine during manufacturing, stator without housing and before assembly of phase connection terminals. Each coil has 3 turns of 9 parallel strands 1.5 mm enameled copper wire.

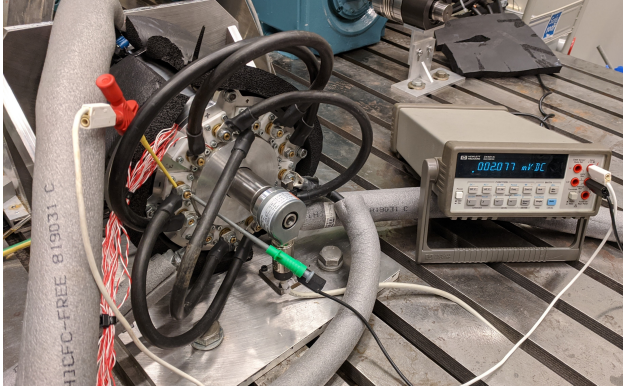


Figure 3.12: 48 V machine during phase resistance measurements with 10 A DC.

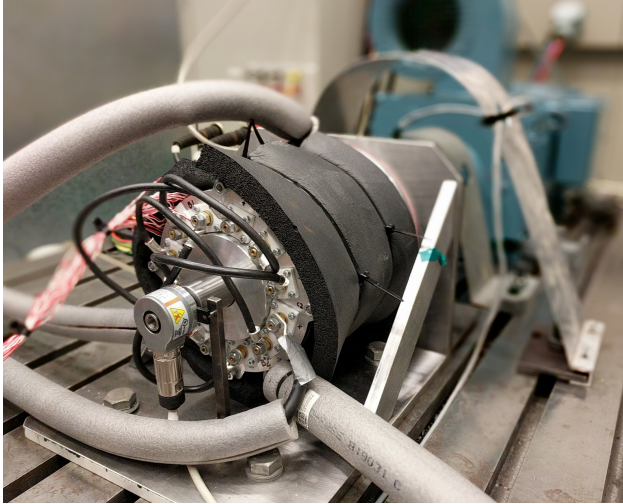


Figure 3.13: 48 V machine during low-current (<100 A) testing in dynamo in calorimetric setup.

4.1 Battery modeling

Parameter results

All parameters for OCV, $R_{0,1,2}$ and $C_{1,2}$ are extracted using semi-automated Matlab scripts that operate on the raw data from the test equipment. The details of the procedure is more described in Paper I. Results from room-temperature tests and 5 C discharge pulses for the maximum achievable SOC window are presented in Fig. 4.3 for OCV, Fig. 4.4 for R_0 , and Fig. 4.5 for $R_{0,1,2}$ and $C_{1,2}$. Since all batteries differ in size and charge capacity, the passive parameters have been scaled with charge capacity to make them fit in the same plots.

A selection of the LIBs are more thoroughly parameterized over a wide temperature span. In this case, all R's and C's are a function of both SOC and temperature and thus become 3D look-up tables in the equivalent circuit model. A simplification of these results, by establishing the R_{10} resistance, is shown in Fig. 4.7. More extensive results can be found in [66], in where the naming of the cells are preserved.

Voltage headroom

When the R+2RC ECM parameters are established, they can be used to predict power availability instantaneously, as well as fairly accurately for a future time that is less than the slowest time constant of the RC networks. Projecting allowed charge and discharge power is extremely useful in advanced LIB applications such as automotive systems. The maximum sustainable power output, i.e. a power level that can be repeatedly used without significantly damaging and accelerating the aging of the cell, is limited by three things:

- Maximum allowed current magnitude
- Maximum temperature
- Minimum (discharge) or maximum (charging) terminal voltage.

High LIB temperatures are often a result from self-heating due to high currents and Joule losses (i^2R), in combination with entropy heating as discussed in Paper 2. Static current limits can be established to limit self-heating, or due to other bottlenecks in current carriers or due to chemical reaction speed in LIBs. Terminal voltage limits are usually given as hard limits by the cell manufacturer. The maximum achievable current can be limited also by the allowed voltage headroom between the internal voltage (OCV) and the terminal voltage. The difference between the two voltages is the internal voltage drop. The maximum power theorem cannot be achieved due to the small voltage drop allowed by static voltage limits. With diffusion and mass transport represented by the two slow RC links, the internal voltage drop increases over time for a constant current, which means the allowed voltage headroom shrinks as a function of the duration of charge or discharge current. The first step in establishing the real-time maximum power capability is to calculate the projected voltage drop, then solve for the resulting maximum current. Fig. 4.1 shows examples for four cells of how the projected voltage response looks for a charge and discharge pulse at the maximum allowed peak rate according to the LIB manufacturer (median value is 10 C). The magnitude of the projected voltage drop according to ECM parameters vary significantly between the parameterized LIB cells at the allowed maximum current. This voltage variation is very important information to include when evaluating the electrical system performance of the adjacent component connected to the same voltage bus.

The resulting power limits, restricted by either static current or voltage headroom, are illustrated in Fig. 4.2. Please note that the absolute power limits are hard to compare because of the large variation in size and capacity for the cells.

Voltage and power in Fig. 4.1 and Fig. 4.2 are evaluated for room temperature. The temperature effect can be incorporated by including temperature dependence in the ECM parameters.

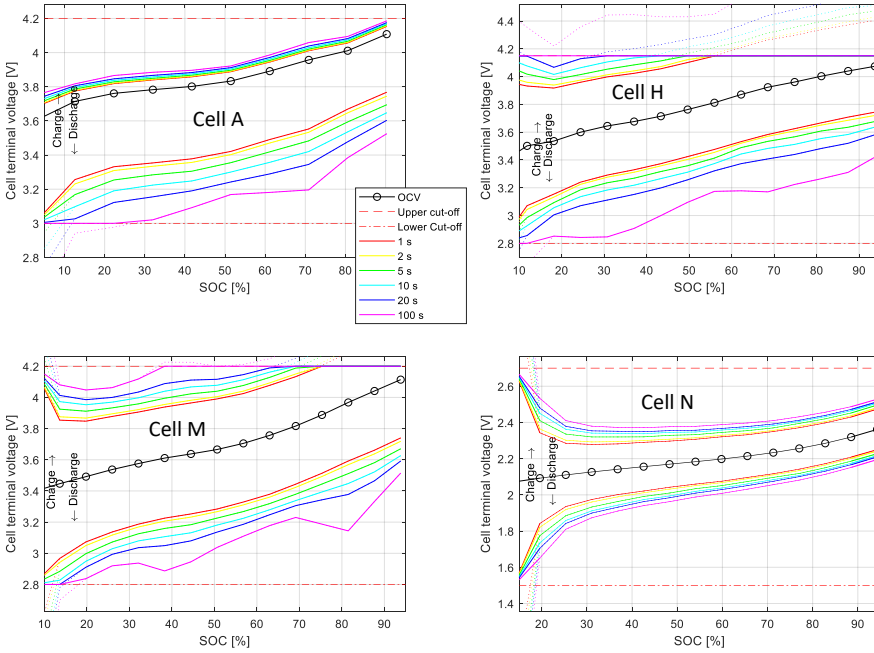


Figure 4.1: The resulting cell voltage at the terminals at the maximum specified current. The legends represent for how long time the current is present, to visualize the effect of diffusion. Dotted lines represent the cell voltage if it was not limited by the minimum and maximum cut-off voltages.

Model verification

Two steps of verification of the ECM are performed. The first level encompasses the simulation of the voltage response with the ECM, feeding in the

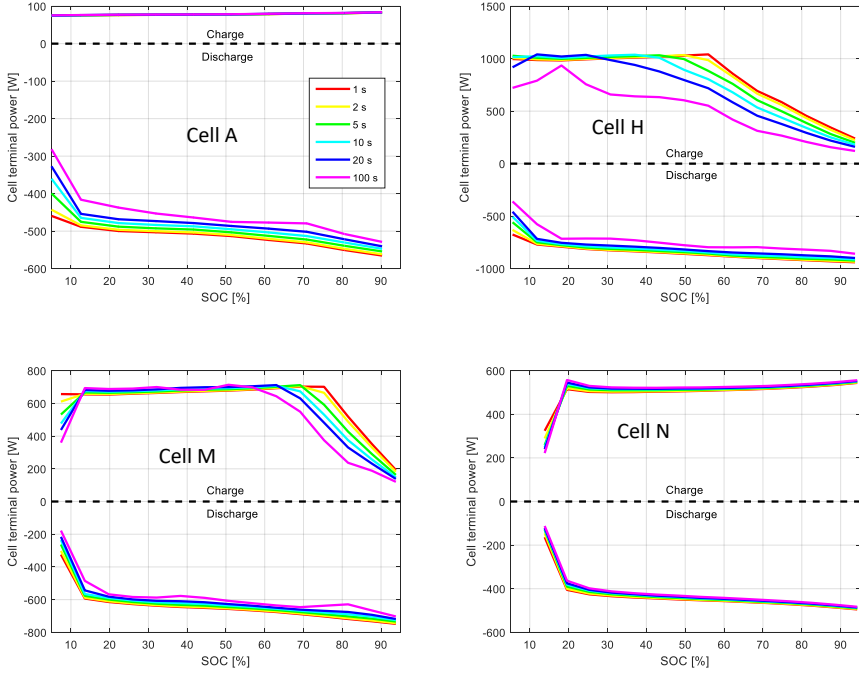


Figure 4.2: Look-ahead charge and discharge power limits established by using a R+2RC ECM and comply with both maximum current and voltage limits.

current used during the pulse discharge test. The model now have both OCV and R, C to vary with SOC, leaving temperature on the side at the moment. A sensitivity analysis of keeping OCV and/or R, C values constant is shown in Fig. 4.6. The RMSE between measurement and model is used to define model error. This method is a way of validating the importance for model accuracy to include the SOC dependence in OCV than it is to incorporate it for the SOC dependence in the R and the C values. It also shows results from both a simple Thevenin ECM (Fig. 2.6a) and the extended Thevenin R+2RC ECM (Fig. 2.6b). For the best case in Fig. 4.6, SOC=50% all variables are SOC dependant, the R+2RC ECM results in 3.4 mV RMSE, and the R_{10} ECM 71.2 mV RMSE. This equates to that best R_{10} ECM shows 21 times higher error in voltage prediction. The corresponding number, when evaluated in a

long drive cycle is 10.7 mV and 28.4 mV RMS voltage error for R+2RC and R₁₀ respectively, as seen in Paper 1, Table III.

The second method of verification includes using a realistic, long, dynamic load cycle that represents how the cell is aimed to be used in its end application. This method is used and presented in Paper II and Paper II. For a over 1.5 hour long drive cycle, without any feedback, the proposed R+2RC ECM performs an RMSE of 15.5 mV (Paper II cell B), 20.3 mV (Paper II cell C), and 10.7 mV (Paper II cell H). No such low RMSE values are found elsewhere in the literature for long dynamic drive cycles.

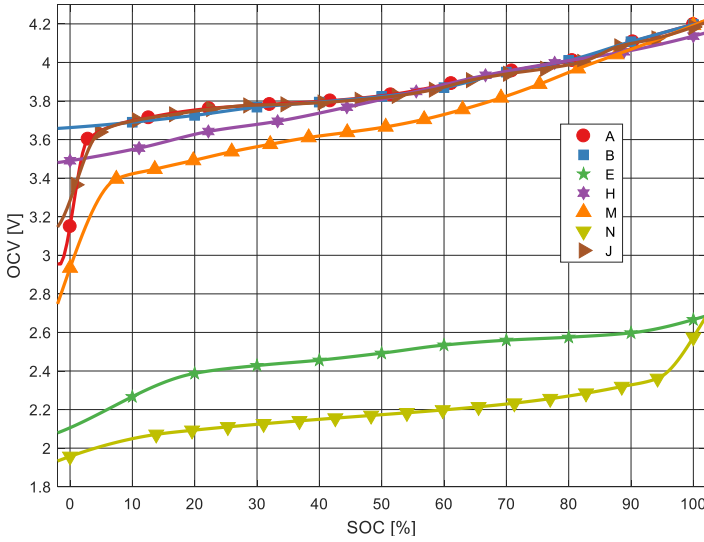


Figure 4.3: Open circuit voltage sample points acquired after 1 h of relaxation between pulse discharge measurements. Inter- & extrapolated lines.

High-level comparison

Fig. 4.8 shows the comparison with a selection of the analyzed cells for the size-independent specific energy versus specific power, where the maximum power is specified for a typical 10 s discharge pulse at room temperature. Each straight line intersecting origo in this chart represent the rate of discharge (C-rate) in (hours)⁻¹. Since the cell manufacturers' maximum peak

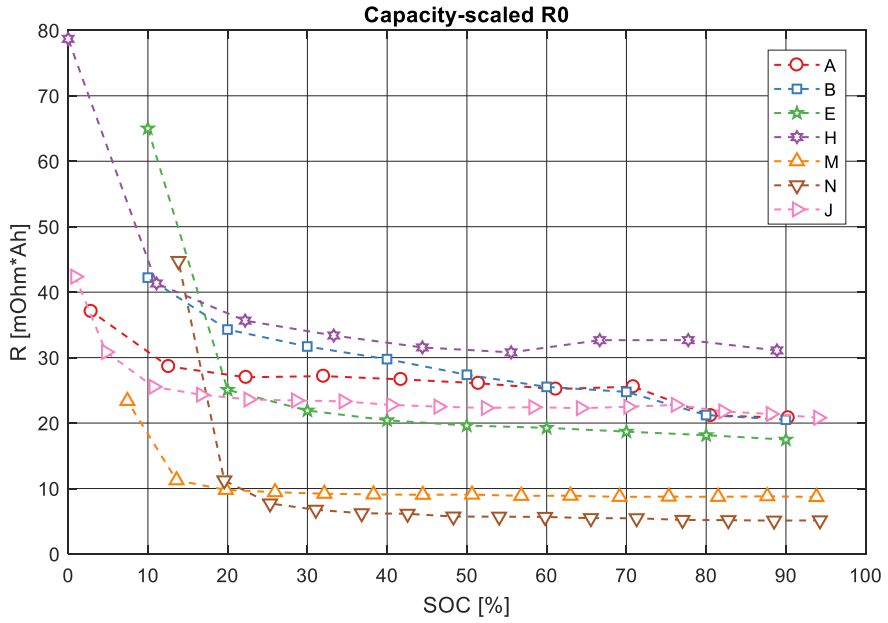


Figure 4.4: Parameters results for R_0 element in the R+2RC ECM (Fig. 2.6b) at room temperature and 5 C discharge. Resistance values are scaled with charge capacity.

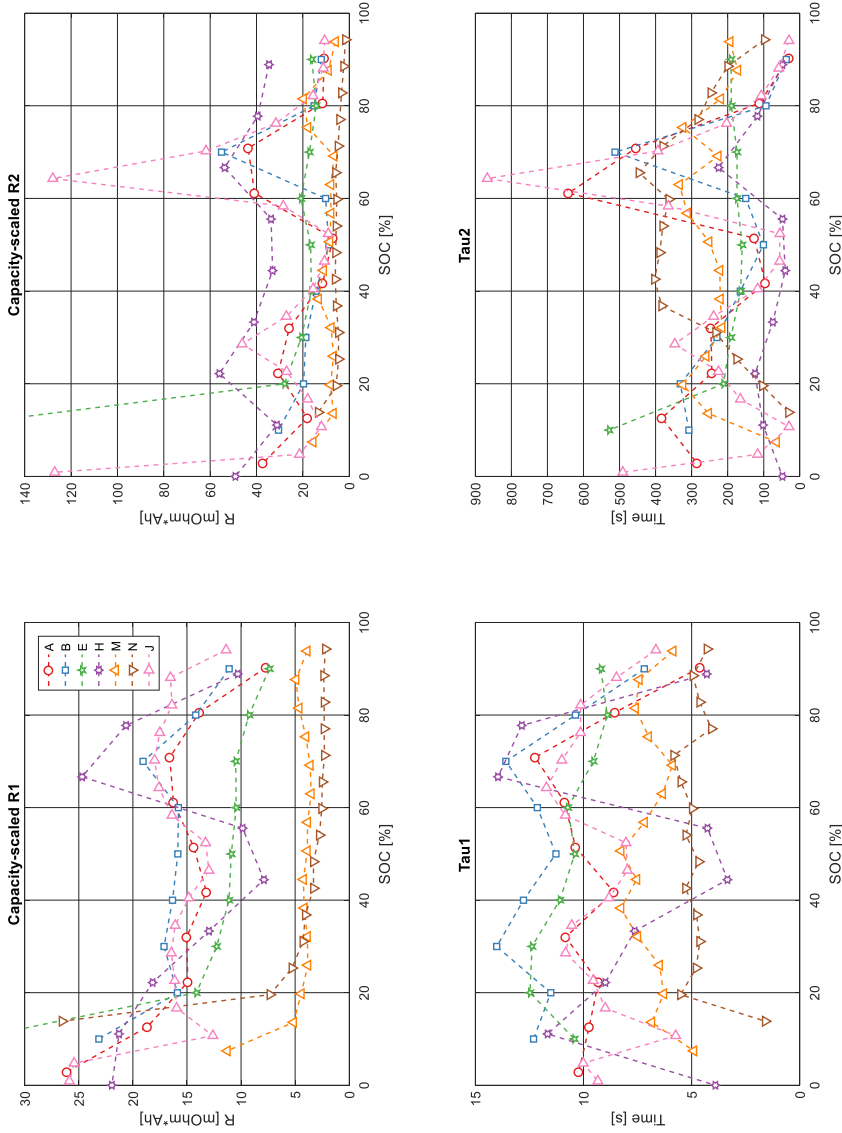


Figure 4.5: Parameters results for R+2RC ECM (Fig. 2.6b) at room temperature and 5 C discharge. Resistance values are scaled with charge capacity.

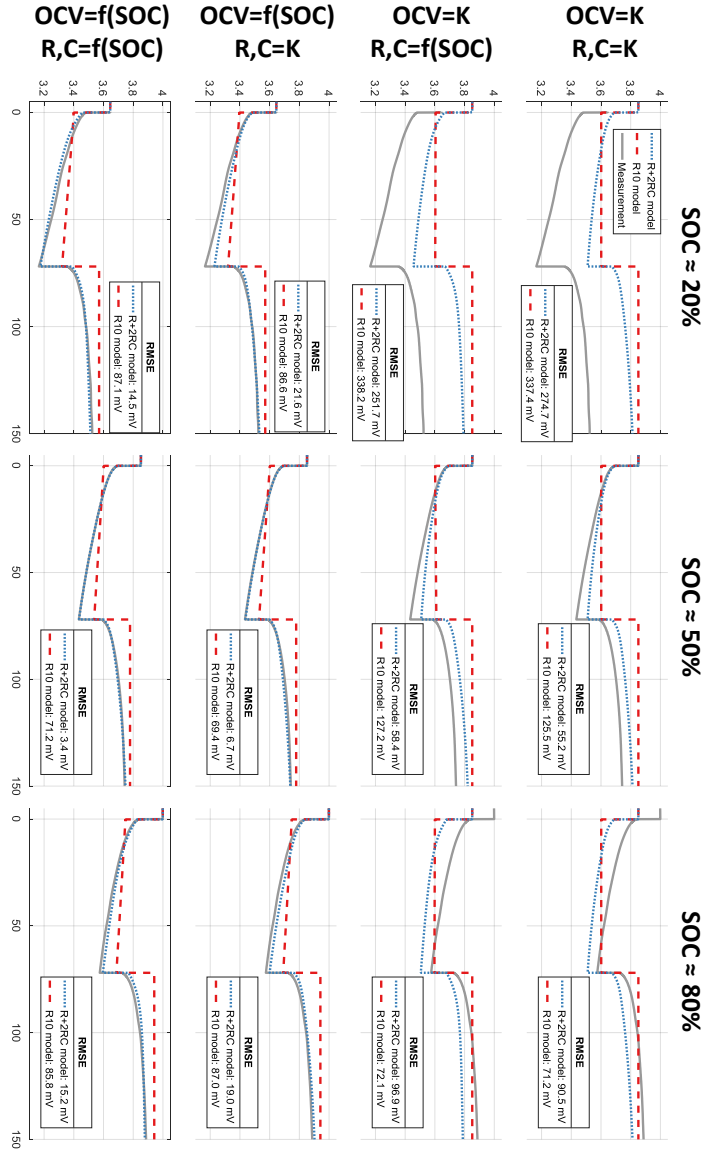


Figure 4.6: The variation of accuracy using both models in R+2RC (Fig. 2.6) while letting OCV and R,C values remain constant (at SOC=50% value) or vary with SOC. X axis is time in seconds. Example for cell H.

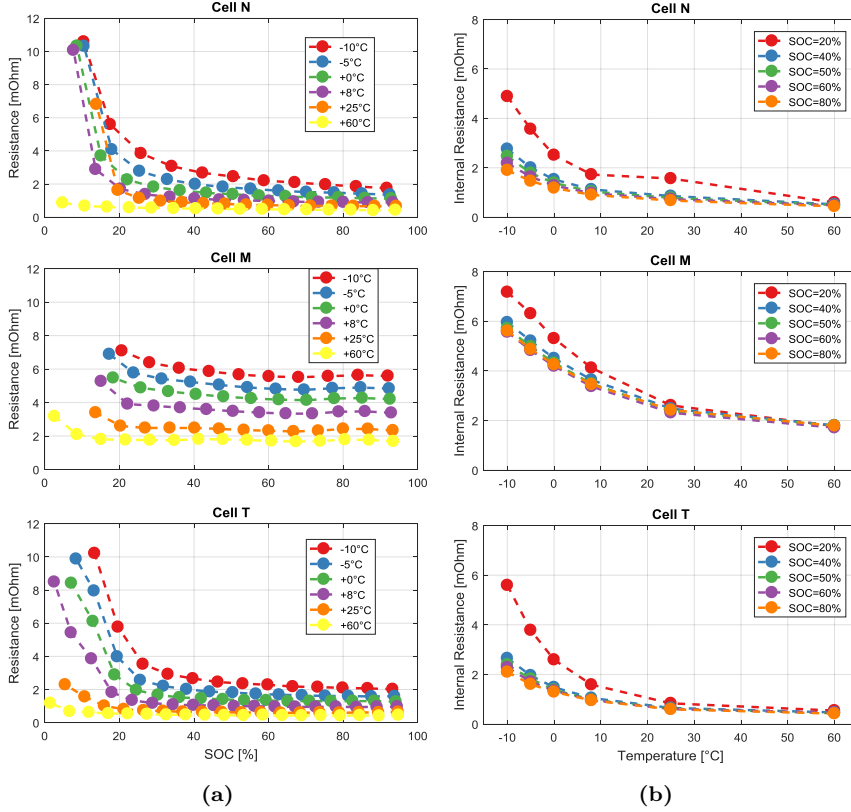


Figure 4.7: Equivalent R_{10} resistance for ECM in Fig. 2.6a as a function of SOC (left column) and temperature (right column). Resistance is typically flat between 20-95% SOC. Low temperature has a very strong effect on resistance. Cell names matching Table 3.1 is found in the plot tile.

discharge C-rate is used to calculate the power, it should be noted that safety margins to ensure long lifetime plays in as a penalty for automotive cells, which are expected to withstand thousands of cycled in harsh environment. Semiprofessional cells are typically specified for a few hundred cycles in ideal conditions.

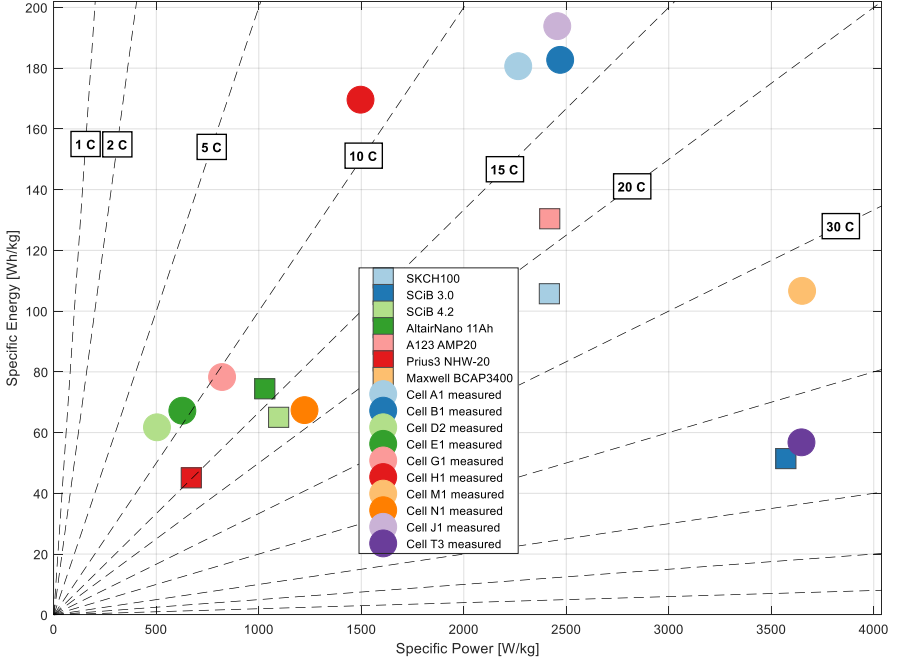


Figure 4.8: Ragone chart over tested batteries (circles) and examples of reference battery cells from datasheet values (squares). The Maxwell supercapacitor is found on coordinate [8500, 7.6] outside the plot.

4.2 Inverter results

The two inverters are tested at 100 kHz f_{sw} continuously up to a current level where either the temperature of the MOSFET packages is close to the maximum allowed, or a power limitation of the power supply or load is reached. For prototype 1, 45 A RMS is reached. The efficiency could not be established

due to very low power factor of the load. Prototype 2 is tested up to 220 A RMS, mainly active current, resulting in 9.0 kW. The available DC power supplies was limiting the possibilities of achieving higher powers. An efficiency of 95.6% is measured, excluding the significant losses in power cables to and from the inverter. This is considered to be successful results considering the challenges with high switching frequency and high currents.

4.3 Electric machine results

Winding layout

The resulting balanced winding layout for a three-phase 12-slot, 10-pole TCWM is visualized in Fig. 4.9. The smallest individual phase element is a coil group, consisting of two adjacent tooth-coils connected in series. Each phase contains two coil groups, which can be configured in a drive system wither individually, in series, and in parallel.

Machine construction and results

Two mechanically identical machines are built, as presented in Paper 8, one with windings optimised for 600 V, and the other optimized for 48 V. Results from testing the 600 V machine can be found in Paper 6-8. The 48 V machine test results are presented in this chapter. All ECM parameters in this chapter are measured for one coil group, meaning the machine is considered to operate in six-phase mode. Voltages and resistances are measured individually on all six phase groups, and the mean (μ) and standard deviation ($\pm 1 \sigma$) is presented in Table 4.1. Ψ_{PM} is calculated using (2.9) from voltage measurements at 1027 rpm mechanical speed. Inductance measurements are made with an LCR meter at 1 kHz excitation while step wise moving the rotor to find minimum and maximum values within one electrical period. The measured torque output for the 48 V machine is seen in Fig. 4.10 together with simulated average torque output beyond maximum thermal limits. The available motor controller was limited to 110 A RMS phase current at the time of measurement. To illustrate the expected performance with a more powerful inverter drive, the measurements from the 600 V machine presented in Paper 7, figure 14, at 90° current angle are re-scaled for the current axis with the coil turn ratio: $N_{600 \text{ V}}/N_{48 \text{ V}} = 28/3$.

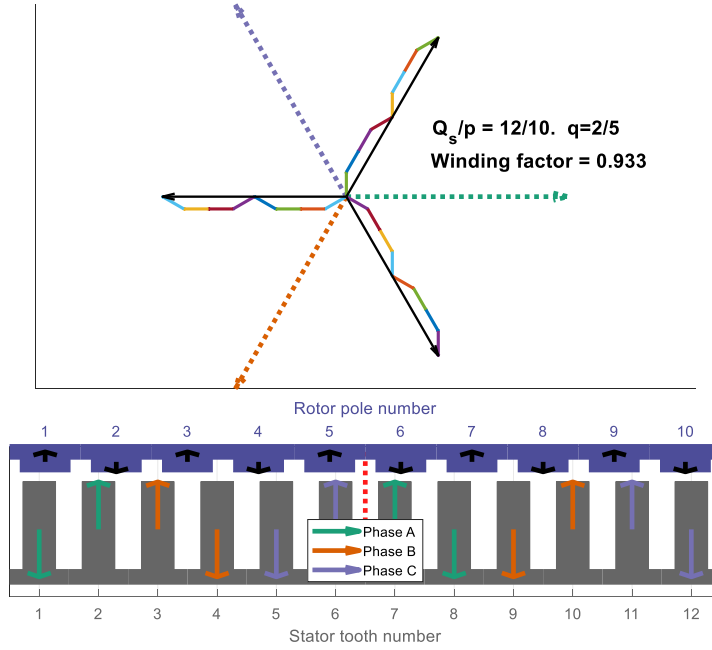


Figure 4.9: Winding phasors and winding layout using Cros' method. Slot per pole per phase (q) and winding factor is displayed. The dotted vertical red line marks the line of anti-symmetry in the stator winding.

Table 4.1: Parameter results from EM ECM extraction

Symbol	Parameter	Value	Unit
n_{ph}	Phase number	6	-
n_p	Pole pairs	5	-
L_d	Stator d inductance	20.9	μH
L_q	Stator q inductance	40.5	μH
$\mu(R_s)$	Coil group resistance	2.18	$\text{m}\Omega$
$\sigma(R_s)$	Standard deviation	47.3	$\mu\Omega$
$\mu(\Psi_{PM})$	PM linked flux	7.74	mWb
$\sigma(\Psi_{PM})$	Standard deviation	19.8	μWb

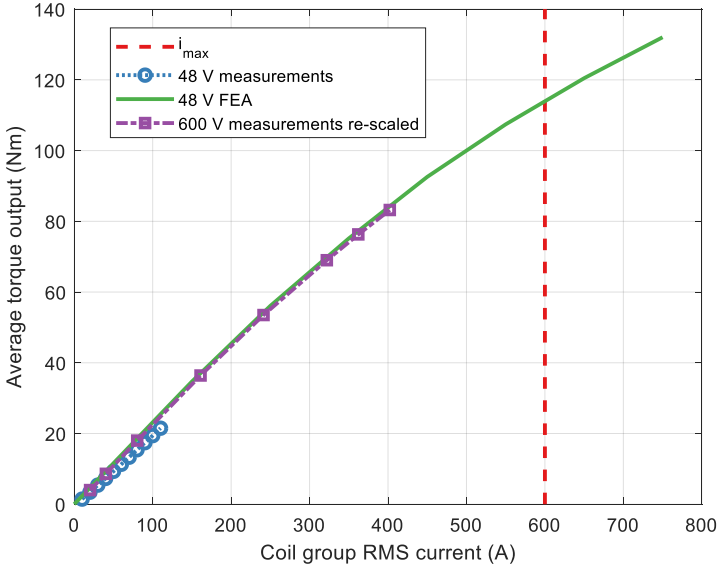


Figure 4.10: Output torque over one electrical period at 150 rpm, 90° current advancement, measured and simulated with FEA at 48 V, and measured for the 600 V machine and re-scaled with the coil turn ratio.

5.1 Main conclusions

The following claims, found during the work presented throughout the thesis, including the appended papers, are:

- For battery models used in time scales relevant to vehicle drive cycle simulations, i.e. 0.1-1000 s, a linear, two-time-constant equivalent circuit model offers a very appealing accuracy compared to all other options found in literature
 - The two time constants should both represent the diffusion phenomena, but still have explicitly separated time constants by more than an order of magnitude, e.g. $\tau_1=10$ s and $\tau_2=200$ s
 - During LIB testing, it is important to allow for plenty of relaxation between operating points in order to make sure the diffusion effects have stabilized. In this work, a 1 h rest time is used for room temperatures. Testing at lower temperatures than room might require more relaxation time. Some cells might need even longer relaxation times, this is believed to be associated with optimization towards

- high energy density, e.g. thick electrodes
- For ECM circuit elements, the temperature is the most important variable to take into account in order to keep model accuracy high, except for OCV where SOC has the higher impact on model accuracy.
 - Using more than two RC networks in the circuit model does not necessarily increase the accuracy in a car drive cycle evaluation, but rather increases the difficulty of achieving robust parameter fits.
 - The model voltage deviation, measured as RMSE in a cell load cycle, reaches as low as 11 mV for a 2RC equivalent circuit. This is the lowest deviation (e.g. highest accuracy) found in literature for linear circuit models without feedback.
 - An RMSE of 15-20 mV is reached by using EIS to identify circuit parameters instead of pulse discharge, which is still among the lowest deviations found in literature.
- The temperature dependence in the measured LIBs, using EIS and frequency-domain analysis, is by far dominated by the medium-frequency spectrum (ca 1 Hz to 1 kHz). This is attributed to charge transfer process in the cells. The charge transfer is shifting the lower-frequency impedance higher, but the delta resistance between 10 mHz and 1 Hz does not change much in comparison.
 - LIBs typically, in room temperature, exhibit a global resistive minimum at 0.5-2 kHz. Additionally, for cells with graphite anodes, a local minimum in reactance is usually displayed around 1 Hz. These features can be interesting when modeling electrical properties in traction systems.
 - The reversible entropy heat can dominate over the irreversible joule losses for some LIB types and some operating points, shown with experiments of a NMC/G cell and experienced even stronger in several experiments with LCO/G cells. The entropy heat is an essential component in any high-accuracy thermal model for LIBs.
 - For a mild hybrid powertrain, using a well designed P2 topology, rather than a P0, can save 21% to 35% more fuel in a rural and city drive cycle respectively.

- For a mild hybrid powertrain, a 20 kW peak power rated electric machine will capture >98% of the use cases in the tested drive cycles. For acceleration purposes, 50 kW peak capability is needed for the rural/highway cycle tested if the electric machine is to power the car alone.
- Compiling a visually navigational map for three-phase double-layer tooth-coil wound machines and their most important electromagnetic properties.
 - Defining and visualizing key performance indices: *key winding factor*, *cogging multiplier*, *fundamental winding factor* and *harmonic leakage factor*.
 - Grouping all TCWM into categories using *key winding factor*, and showing they share electromagnetic features.
 - Declaring, by analytical means, that many winding configurations display excessive inductance (*harmonic leakage factor*) due to the magnetisation of sub- and super-harmonics over the airgap that are not necessarily contributing to net torque output.
- Design, build and test a direct-oil cooled three-phase tooth-coil wound machine and verify the performance using FEA with very good agreement of torque and Back-EMF.
 - The efficiency, measured both as mechanical power out divided by electrical power in, as well as by direct thermal loss (calorimetric), is verified as high as 95%. This point agrees with FEA within 0.9 percent units.
 - The verified FEA model predicts a large peak efficiency area of 95%, which is higher than most automotive machines reported in the academic literature, and it is on par with the state-of-art automotive traction machines use by Toyota, BMW, Nissan.
 - The net power density of the presented machine, accounting for active iron volume, is on par with mass-produced state-of-the-art traction machines from BMW and Toyota, and it is higher than the vast majority of machines presented in the academic literature.
 - The design and validation of an electric machine for automotive application with the combination of high efficiency (>90%) and

high net power density (>15 kW/l) has not been previously found reported in the academic literature.

- The construction and validation at the design target max torque output of a direct-liquid cooled automotive traction machine is rarely found in the literature.

5.2 Future Work

The following topics have been made salient during the process of finalizing this thesis:

- Unifying the LIB test methodology and ECM to work on super capacitors and offer the same level of high model accuracy. Super capacitors might display both high self-discharge and very slow mass transport, which can make the proposed LIB model inaccurate.
- Designing a six-channel compact inverter power module that fits directly on the machine housing and thus share oil cooling with the machine.
- Experimental evaluation of driving the EM with a six-leg or six-H-bridge inverter and utilizing PWM carrier wave phase shift to minimize DC capacitor current ripple.
- Experimentally establishing the rotor (magnet) losses in the prototype TCWM at high rotational speeds. Magnet segmentation is used to limit the harmonic losses, but the theoretical loss calculations have not been verified. The temperature coefficient of the magnet material remanent flux can be used to establish the average magnet temperature on-line at no-load by measuring the BEMF.
- Continue to develop the theoretical framework for key performance indices to include TCWMs with more than three phases.
- Verify the harmonic leakage inductance for different TCWM types by using FEA. It is believed that the rotor geometry, especially reluctance rotors, can reduce the effect of spacial harmonics magnetizing over the airgap.
- Evaluate the extra machine losses due to time harmonics in TCWMs when switching with 10 kHz and 100 kHz through FEA.

APPENDIX A

Linear equivalent circuit model

This appendix presents the basic mathematical analysis of linear equivalent circuit models with RC links used for LIBs. The ideal voltage source in the simple Thevenin ECM of Fig. A.1a is trivial to model, this analysis will focus on modeling one series RC link in Fig. A.1b. Fig. A.2 isolates one RC links from the ECM, and from here one can apply nodal analysis:

$$i = i_R + i_C \quad (\text{A.1a})$$

$$i_R = v/R \quad (\text{A.1b})$$

$$i_C = C \frac{dv}{dt} \quad (\text{A.1c})$$

From here, we can establish an ordinary first order linear homogeneous differential equation (ODE):

$$\frac{dv}{dt} + \frac{v}{R C} = \frac{i}{C} \quad (\text{A.2})$$

It is important now to note that both v and i are function of time. Since

it is hard to find a general analytical solution for the differential equation to the arbitrary function $i(t)$, we instead find solutions for two special cases: Zero-state (Fig. A.2a) and zero-input (Fig. A.2b). Zero state means that no energy is stored in the system at $t = 0$, but an external signal is applied starting at positive time. Zero-input means that there is indeed stored internal energy expressed as voltage over the capacitor, but no external excitation to the circuit.

One solution to the zero-state form ODE is the sum of the homogeneous solution and the particular solution:

$$v_{zs} = v_h + v_p \quad (\text{A.3})$$

The boundary conditions for this homogeneous case is

$$\begin{cases} v(t \leq 0) & = & 0 \\ i(t \leq 0) & = & 0 \end{cases} \quad (\text{A.4})$$

and the differential equation becomes

$$\frac{dv}{dt} + \frac{v}{RC} = 0 \quad (\text{A.5})$$

with the homogeneous solution

$$v_h(t) = K_2 e^{-\frac{t}{RC}}. \quad (\text{A.6})$$

However, the constant K_2 cannot be determined until the particular solution is found. The boundary conditions for the particular solution for the zero-state circuit is defined by applying a step response in current after zero time:

$$\begin{cases} v(t \leq 0) & = & 0 \\ i(t > 0) & = & i_0 \end{cases} \quad (\text{A.7})$$

and the ODE for Fig. A.2a becomes

$$\frac{dv}{dt} + \frac{v}{RC} = \frac{i_0}{C}. \quad (\text{A.8})$$

A solution of the same order as the right-hand side can be found, e.g.

$$\begin{cases} v_p &= K_3 \\ \frac{dv_p}{dt} &= 0 \end{cases} \quad (\text{A.9})$$

Combining (A.9) into (A.8) yields $K_3 = R i_0$. Now (A.3) becomes $v_{zs} = K_2 e^{-\frac{t}{RC}} + R i_0$ and applying the operating point $t = 0$ in (A.4) to this solution, K_2 can be found:

$$0 = K_2 e^{-\frac{0}{RC}} + R i_0; \quad (\text{A.10a})$$

$$K_2 = -R i_0; \quad (\text{A.10b})$$

The full solution to the zero-state problem becomes

$$v_{zs}(t) = R \left(1 - e^{-\frac{t}{RC}} \right). \quad (\text{A.11})$$

As this is true for a charging process of the capacitor, we can also find out the discharge profile through the zero-input case, which is defined through the conditions corresponding to storing energy at time zero, but with no external stimuli:

$$\begin{cases} i(t) &= 0 \\ v(t=0) &= V_0 \end{cases} \quad (\text{A.12})$$

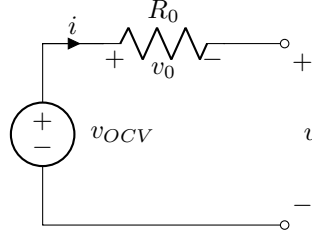
which makes the ODE to solve the same as in (A.5), and the solution v_{zi} has the same form as in (A.6), however, a different constant: K_1 . With the operating point $t = 0$ and the initial condition in (A.12), the solutions becomes:

$$v_{zi}(t) = K_1 e^{-\frac{t}{RC}} \quad (\text{A.13a})$$

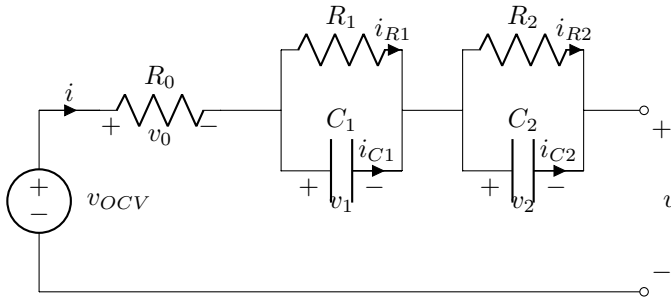
$$V_0 = K_1 e^{-\frac{0}{RC}} = K_1 \quad (\text{A.13b})$$

$$v_{zi}(t) = V_0 e^{-\frac{t}{RC}}. \quad (\text{A.13c})$$

Eq (A.11) or (A.13c) can be used to represent the charging and discharging procedure of one RC link, respectively. For example, the charging or discharging pulse on a LIB. Since the system is assumed to be linear time invariant, two series connected RC links can be superimposed and treated independently during analysis. It should also be noted that the denominator of the expo-



(a) Simple R_0 Thevenin ECM.



(b) Extended R+2RC Thevenin ECM.

Figure A.1: Reference ECMs for LIBs.

nent in the natural logarithms in the solutions to the ODE in e.g. (A.11) and (A.13c) is equivalent to the time constant of the corresponding RC link: $\tau = R C$.

State space model

From the model in Fig. A.1b, it is straight-forward to express the output voltage equation as

$$v = v_{OCV} - v_0 - v_1 - v_2 . \quad (\text{A.14})$$

The voltages over each of the two individual RC links with subscript $x = 1, 2$ can be derived by Kirchhoff's current law within the RC link as:

$$i = i_{Rx} + i_{Cx} = \frac{v_x}{R_x} + \frac{dv_x}{dt} C_x \quad (\text{A.15a})$$

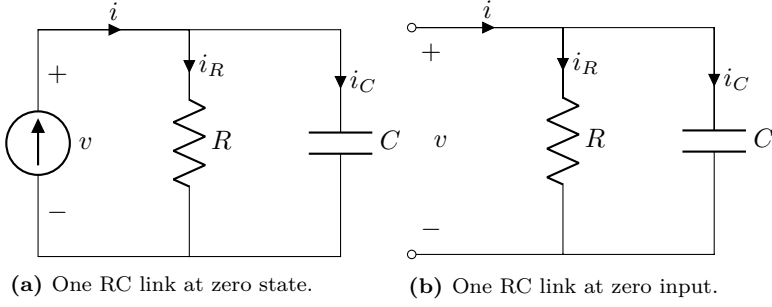
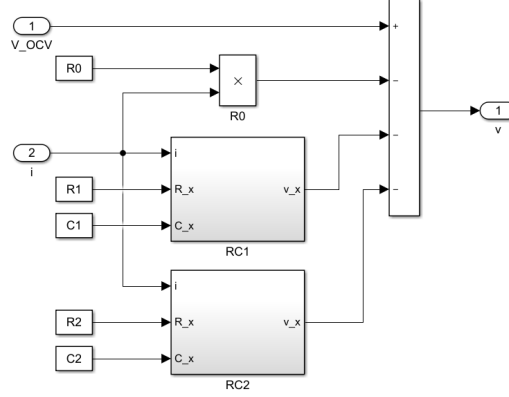


Figure A.2: Simplified RC circuit used for analysis and formulation of equations.

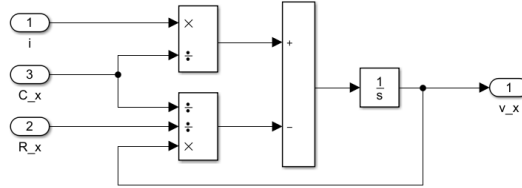
$$\frac{dv_x}{dt} = \frac{i}{C_x} + -\frac{v_x}{R_x C_x} \quad (\text{A.15b})$$

$$v_x = \int \left(\frac{i}{C_x} + -\frac{v_x}{R_x C_x} \right) dt . \quad (\text{A.15c})$$

Equations in state space form can now easily be generated from (A.15b). (A.15c) makes it very intuitive to implement in model based graphical programming environments such as Matlab Simulink. Fig. A.3a shows a such implementation with two subsystems of RC links depicted in Fig. A.3b.



(a) Total Simulink implementation of (A.14), where each of the two subsystems represent an RC link as in Fig. A.3b



(b) Simulink model implementation of one RC link as depicted in Fig. 2.6b and defined in state-space form in (A.15c).

Figure A.3: Implementation of ECM in state-space form in Matlab Simulink.

References

- [1] E. Parliament, *CO2 emissions from cars: Facts and figures*, <https://www.europarl.europa.eu/news/en/headlines/society/20190313ST031218/co2-emissions-from-cars-facts-and-figures-infographics>, Apr. 2019.
- [2] G. Erbach, “CO2 standards for new cars and vans (pe 614.689)”, *European Parliamentary Research Service*, 2019.
- [3] J. V. VWvortex, *Lupo 3l once again enters guiness book of world records*, <https://www.vwvortex.com/news/volkswagen-news/lupo-3l-once-again-enters-guiness-book-of-world-records/>, Dec. 2003.
- [4] E. C. C. Action, *Reducing CO2 emissions from passenger cars*, https://ec.europa.eu/clima/policies/transport/vehicles/cars_en, Aug. 2017.
- [5] P. Els, “Modern materials unlock the potential of downsized engines”, *Automotive IQ*, Dec. 2014.
- [6] B. Morey, “Cooled egr shows benefit for gasoline engines”, *SAE Automotive Engineering*, pp. 18–20, Oct. 2014.
- [7] R. Backhaus, “Electric cars with 48-V powertrains”, *MTZ worldwide*, vol. 81, no. 2, pp. 10–15, 2020.
- [8] G. C. Congress, *PSA peugeot citroën developing 48V mild hybrid solution for 2017*, <http://www.greencarcongress.com/2013/01/psa-20130123.html>, Jan. 2013.

- [9] Continental, *Small step big difference: Continental's "48 Volt eco drive" offers mild hybrid functions*, http://www.continental-corporation.com/www/pressportal_com_en/themes/press_releases/1_topics/fairs_events/pr_2013_09_10_iaa_48v_eco_en.html, Alternative url: <http://www.greencarcongress.com/2013/09/201320910-conti2.html>, Sep. 2013.
- [10] G. C. Congress, *Johnson controls introducing first-generation 48V micro hybrid battery at frankfurt show*, <http://www.greencarcongress.com/2013/09/20130911-jc.html>, Sep. 2013.
- [11] —, *Kia introduces new mild hybrid powertrain, 7-speed DCT*, <http://www.greencarcongress.com/2014/03/20140304-kia.html>, Mar. 2014.
- [12] I. T. Dörsam, I. S. Kehl, D.-I. A. Klinkig, D.-I. A. Radon, *et al.*, "The new voltage level 48 V for vehicle power supply", *ATZ Elektronik*, vol. 7, no. 1, pp. 10–15, 2012.
- [13] C. Lensch-Franzen, M. Gohl, M. Kronstedt, and M. Friedmann, "Rde relevance of 48-v hybrid concepts", *MTZ worldwide*, vol. 79, no. 7-8, pp. 64–69, 2018.
- [14] M. Nalbach, A. Körner, and S. Kahnt, "The 48 V hybrid potential analysis and system design", *ATZelektronik worldwide*, vol. 10, no. 2, pp. 30–33, 2015.
- [15] G. C. Congress, *Alabc and cpt to introduce 48V lc super hybrid demonstrator at vienna motor symposium*, <http://www.greencarcongress.com/2013/04/lcsh-20130424.html>, Apr. 2013.
- [16] J. G. Kassakian, H.-C. Wolf, J. M. Miller, and C. J. Hurton, "Automotive electrical systems circa 2005", *IEEE spectrum*, vol. 33, no. 8, pp. 22–27, 1996.
- [17] J. Bilo, H.-G. Burghoff, H. dos Santos, J. Engbring, E. Erich, P. Gresch, and F. Harrmann, "48-Volt electrical systems-a key technology paving to the road to electric mobility", *ZVEI-German Electrical and Electronic Manufacturers Association*, 2016.
- [18] R. Bao, V. Avila, and J. Baxter, "Effect of 48 V mild hybrid system layout on powertrain system efficiency and its potential of fuel economy improvement", SAE Technical Paper, Tech. Rep., 2017.

-
- [19] J. King, M. Heaney, J. Saward, A. Fraser, M. Criddle, T. Cheng, G. Morris, and P. Bloore, “Hyboost: An intelligently electrified optimised downsized gasoline engine concept”, in *Proceedings of the FISITA 2012 World Automotive Congress*, Springer, 2013, pp. 483–496.
 - [20] S. Jurkovic, J. C. Morgante, K. M. Rahman, and P. J. Savagian, “Electric machine design and selection for general motors e-assist light electrification technology”, in *2012 IEEE Energy Conversion Congress and Exposition (ECCE)*, IEEE, 2012, pp. 906–913.
 - [21] R. Bojoi, A. Cavagnino, M. Cossale, and A. Tenconi, “Multiphase starter generator for a 48-V mini-hybrid powertrain: Design and testing”, *IEEE Transactions on Industry Applications*, vol. 52, no. 2, pp. 1750–1758, 2015.
 - [22] A. Cavagnino, A. Tenconi, and S. Vaschetto, “Experimental characterization of a belt-driven multiphase induction machine for 48-V automotive applications: Losses and temperatures assessments”, *IEEE Transactions on Industry Applications*, vol. 52, no. 2, pp. 1321–1330, 2015.
 - [23] X. Chen and S. Shen, “Comparison of two permanent-magnet machines for a mild hybrid electric vehicle application”, SAE Technical Paper, Tech. Rep., 2008.
 - [24] J. S. Hsu, T. A. Burress, S. T. Lee, R. H. Wiles, C. Coomer, J. W. McKeever, and D. J. Adams, “16,000-rpm interior permanent magnet reluctance machine with brushless field excitation”, in *2008 IEEE Industry Applications Society Annual Meeting*, IEEE, 2008, pp. 1–6.
 - [25] M. Kamiya, “Development of traction drive motors for the toyota hybrid system”, *IEEE Transactions on Industry Applications*, vol. 126, no. 4, pp. 473–479, 2006.
 - [26] C. Palve and P. Tilak, “Design & development of advanced 48 V electrified powertrain for meeting future co 2 emission requirements”, SAE Technical Paper, Tech. Rep., 2019.
 - [27] T. Burress and S. Campbell, “Benchmarking EV and HEV power electronics and electric machines”, in *2013 IEEE Transportation Electrification Conference and Expo (ITEC)*, IEEE, 2013, pp. 1–6.

- [28] R. H. Staunton, C. W. Ayers, L. Marlino, J. Chiasson, and B. Burress, “Evaluation of 2004 toyota prius hybrid electric drive system”, Oak Ridge National Lab.(ORNL), Oak Ridge, TN (United States), Tech. Rep., 2006.
- [29] T. A. Burress, S. L. Campbell, C. Coomer, C. W. Ayers, A. A. Wereszczak, J. P. Cunningham, L. D. Marlino, L. E. Seiber, and H.-T. Lin, “Evaluation of the 2010 toyota prius hybrid synergy drive system”, Oak Ridge National Lab.(ORNL), Tech. Rep., 2011.
- [30] S. Chowdhury, E. Gurpinar, G.-J. Su, T. Raminosoa, T. A. Burress, and B. Ozpineci, “Enabling technologies for compact integrated electric drives for automotive traction applications”, in *2019 IEEE Transportation Electrification Conference and Expo (ITEC)*, IEEE, 2019.
- [31] B. Ozpineci, “Annual progress report for the electric drive technologies program”, *Oak Ridge National Laboratory, Tech. Rep*, 2016.
- [32] F. Fürst, “Design of a 48 V three-phase inverter for automotive applications”, Master’s thesis, Chalmers University of Engineering, 2015.
- [33] A. D. Wearing, J. Haybittle, R. Bao, J. W. Baxter, C. Rouaud, and O. Taskin, “Development of high power 48V powertrain components for mild hybrid light duty vehicle applications”, in *2018 IEEE Energy Conversion Congress and Exposition (ECCE)*, IEEE, 2018, pp. 3893–3900.
- [34] J. Tang, Y. Liu, Y. Rastogi, N. Sharma, and T. Shukla, “Study of voltage spikes and temperature rise in power module based integrated converter for 48 V 20 kW electrically excited synchronous machines”, in *2018 IEEE Applied Power Electronics Conference and Exposition (APEC)*, IEEE, 2018, pp. 210–217.
- [35] E. Gurpinar and B. Ozpineci, “Loss analysis and mapping of a sic mosfet based segmented two-level three-phase inverter for ev traction systems”, in *2018 IEEE Transportation Electrification Conference and Expo (ITEC)*, IEEE, 2018, pp. 1046–1053.
- [36] K.-M. Fritsch, S. Christoph, B. Tobias, and C. Markus, *Challenges of a 48 V drive system with 20 kw continuous mechanical power*, 2017.

-
- [37] J. Tang, “Synchronous machines with high-frequency brushless excitation for vehicle applications”, PhD thesis, Chalmers University of Technology, 2019.
 - [38] J. Tang, Y. Liu, and N. Sharma, “Modeling and experimental verification of high-frequency inductive brushless exciter for electrically excited synchronous machines”, *IEEE Transactions on Industry Applications*, vol. 55, no. 5, pp. 4613–4623, 2019.
 - [39] A. Patzak, F. Bachheibl, A. Baumgardt, G. Dajaku, O. Moros, and D. Gerling, “ISCAD-electric high performance drive for individual mobility at extra-low voltages”, *SAE International Journal of Alternative Powertrains*, vol. 5, no. 1, pp. 148–156, 2016.
 - [40] B. Rubey and D. Gerling, “Design of high current low voltage half-bridges for multi-phase inverter application in the ISCAD drive”, in *2016 19th International Conference on Electrical Machines and Systems (ICEMS)*, IEEE, 2016, pp. 1–6.
 - [41] S. Runde, A. Baumgardt, O. Moros, B. Rubey, and D. Gerling, “ISCAD—design, control and car integration of a 48 volt high performance drive”, *CES Transactions on Electrical Machines and Systems*, vol. 3, no. 2, pp. 117–123, 2019.
 - [42] N. Brown, T. Jahns, and R. Lorenz, “Power converter design for an integrated modular motor drive”, in *2007 IEEE Industry Applications Annual Meeting*, IEEE, 2007, pp. 1322–1328.
 - [43] J. Wang, Y. Li, and Y. Han, “Evaluation and design for an integrated modular motor drive (IMMD) with gan devices”, in *2013 IEEE Energy Conversion Congress and Exposition*, IEEE, 2013, pp. 4318–4325.
 - [44] L. Verkroost, J. Van Damme, H. Vansompel, F. De Belie, and P. Sergeant, “Module connection topologies and interleaving strategies for integrated modular motor drives”, in *2019 IEEE International Electric Machines & Drives Conference (IEMDC)*, IEEE, 2019, pp. 559–564.
 - [45] H. Vansompel, P. Sergeant, L. Dupré, and A. Van den Bossche, “Axial-flux pm machines with variable air gap”, *IEEE Transactions on industrial electronics*, vol. 61, no. 2, pp. 730–737, 2013.
 - [46] H. Hakvoort and T. Olbrich, “Series application of a 48-V hybrid drive”, *MTZ worldwide*, vol. 78, no. 9, pp. 26–31, 2017.

- [47] W. Drury, C. Patel, A. Atkins, and A. Wearing, “High power density, 48V electrified drivetrain technology for future hybrid and electric vehicles”, *SAE International Journal of Advances and Current Practices in Mobility*, vol. 1, no. 2019-26-0034, pp. 55–60, 2019.
- [48] S. Skoog, “Power sources for hybrid electric vehicles”, Master’s thesis, Lund University, 2009.
- [49] “ISO6469-1:2009 - Electrically propelled road vehicles – Safety specifications – Part 1: On-board rechargeable energy storage system (RESS)”, ISO, Standard, 2009.
- [50] “Regulation No 100 - Uniform provisions concerning the approval of vehicles with regard to specific requirements for the electric power train”, Publications Office of the European Union, Standard, 2018.
- [51] “VDA 320 - electric and electronic components in motor vehicles 48 V on-board power supply”, VDA, Standard, 2014.
- [52] “ISO 21780 - road vehicles — supply voltage of 48 V — electrical requirements and tests”, ISO, Standard, 2019.
- [53] “Low-voltage electrical installations”, IEC, Standard, 2005.
- [54] “The Low Voltage Directive (LVD) (2014/35/EU)”, EU, Standard, 2014.
- [55] B. Pattipati, B. Balasingam, G. Avvari, K. Pattipati, and Y. Bar-Shalom, “Open circuit voltage characterization of lithium-ion batteries”, *Journal of Power Sources*, vol. 269, pp. 317–333, 2014.
- [56] J. Landesfeind, D. Pritzl, and H. A. Gasteiger, “An analysis protocol for three-electrode li-ion battery impedance spectra: Part i. analysis of a high-voltage positive electrode”, *Journal of The Electrochemical Society*, vol. 164, no. 7, A1773–A1783, 2017.
- [57] J. Song and M. Z. Bazant, “Effects of nanoparticle geometry and size distribution on diffusion impedance of battery electrodes”, *Journal of The Electrochemical Society*, vol. 160, no. 1, A15–A24, 2013.
- [58] M. E. Orazem and B. Tribollet, *Electrochemical impedance spectroscopy*. John Wiley & Sons, 2017.
- [59] D. Andre, M. Meiler, K. Steiner, H. Walz, T. Soczka-Guth, and D. Sauer, “Characterization of high-power lithium-ion batteries by electrochemical impedance spectroscopy. ii: Modelling”, *Journal of Power Sources*, vol. 196, no. 12, pp. 5349–5356, 2011.

- [60] J. R. Hendershot and T. J. E. Miller, *Design of brushless permanent-magnet machines*. Motor Design Books Venice, Florida, USA, 2010.
- [61] C. Tisell and U. Tariq, “Design, construction and evaluation of a distributed 48 V inverter for a mild hybrid vehicle”, Master’s thesis, Chalmers University of Technology, 2018.
- [62] B. Jude and A. Santosh, “Design and characterization of a 48V inverter for mild hybrid vehicle application”, Master’s thesis, Chalmers University of Technology, 2019.
- [63] J. Cros and P. Viarouge, “Synthesis of high performance pm motors with concentrated windings”, *IEEE transactions on energy conversion*, vol. 17, no. 2, pp. 248–253, 2002.
- [64] F. Meier, “Permanent-magnet synchronous machines with non-overlapping concentrated windings for low-speed direct-drive applications”, PhD thesis, KTH, 2008.
- [65] F. Libert and J. Soulard, “Investigation on pole-slot combinations for permanent-magnet machines with concentrated windings”, in *Proc. ICEM*, 2004, pp. 530–535.
- [66] M. Anandaguru and A. Eriksson, “Model based development of mild hybrid electrical battery systems”, Master’s thesis, Chalmers University of Technology, 2018.

Part II

Included Papers

Paper I

Parameterization of equivalent circuit models for high power lithium-ion batteries in HEV applications

Presented 2016-09-06 at
EPE2016, Karlsruhe, Germany

Published 2017-05-18 in IEEE Xplore:
<http://ieeexplore.ieee.org/document/7695340/>

Parameterization of Equivalent Circuit Models for High Power Lithium-Ion Batteries in HEV Applications

Stefan Skoog
Div. of Electrical Power Engineering
Dept. of Energy and Environment
Chalmers University of Technology
Gothenburg, Sweden
Email: stefan.skoog@chalmers.se

Acknowledgment

This work is sponsored by the Swedish Governmental Agency for Innovation Systems (VINNOVA).

Keywords

«Automotive application», «Automotive component», «Batteries», «Device characterisation», «Device modeling», «Hybrid Electric Vehicle», «Energy storage», «Impedance measurement»

Abstract

Three different linear equivalent electrical circuit models for power optimized lithium-ion batteries are parameterized and compared in a long dynamic load cycle representing typical hybrid electric vehicle usage. The goal is to estimate the voltage on the battery terminals by only using an open-loop electrical model. Model parameters are extracted through a simple discharge pulse test and the parameter results are presented for five different types of batteries. A quantification of the model fit is presented and compared with similar studies.

Nomenclature

Table I: Glossary

Acronym	Explanation
ECM	Equivalent Circuit Model
G	Graphite, anode material
LCO	Lithium-Cobalt Oxide ($LiCoO_2$), cathode material
LIB	Lithium-Ion Battery
LMO	Spinel Lithium-Manganese Oxide ($LiMn_2O_4$), cathode material
LTO	Spinel Lithium-Titanate Oxide ($Li_4Ti_5O_{12}$), anode material
MSE	Mean Squared Error
NMC	Nickel-Manganese-Cobalt Oxide ($LiNiMnCoO_2$), cathode material
NMO	Lithium-Nickel-Manganese Oxide ($Li_2Mn_3NiO_8$), cathode material
OCV	Open-Circuit Voltage
PHEV	Plug-in Hybrid Electric Vehicle
SOC	State of Charge

Introduction

Electrification of light-duty personal vehicles has the potential to offer significant fuel savings and reduction in emissions. Increasing the amount of electrification is an attractive method for vehicle manu-

facturers on reducing the fleet-average fuel consumption. This can be done with electric hybridization of the powertrain, where the key components are; a small but efficient battery, and an electric machine to assist the combustion engine. This setup typically require a power-optimized battery and several modern lithium-ion battery (LIB) chemistries can deliver the required performance in terms of power density. Since LIBs are one of the most expensive and critical components in a hybrid electric powertrain, it is very important to dimension it adequately. A good sized LIB operates close to its limits of performance, whenever needed, without taking permanent damage. Adequate sizing requires accurate and efficient model-based development simulations to run through anticipated scenarios of operation. Representing the electrical behavior of LIBs can be done with physics-based modeling, empirical modeling or a combination of the two methods. In this study, an empirical method is explained, used and applied to several commercially available LIBs. The test method is a simple but efficient method of analyzing single cells of power optimized LIBs using only square wave discharge current pulses as the main stimuli. The result is a set of parameter for an ECM, and the model is then implemented in a simulation environment and the output of the model is compared with measurements from a dynamic load cycle. The chemistries of the tested cells are NMO/LTO, LMO/LTO, NMC+LMO/G and LCO/G and the nominal capacity ranges 10-28 Ah. All test objects are new and healthy, ageing is not considered in this scope. The parameter extraction is limited to room temperature.

Previous work in fitting equivalent circuit models to LIBs from time-domain data is reported in [1, 2, 3, 4, 5, 6, 7]. However, quite few papers quantify the total variance in dynamic load cycles and rarely compare model results for more than one cell and/or cell chemistry. The main contributions of this paper is the simplicity of the test method explained, the application of the test method on several commercially available LIBs, and the quantification of model variance in a long dynamic load cycle with a wide operating window.

Method

The test is based on high-current discharge pulses with well-defined pulse length and depth. All test are performed in room temperature ($20 \pm 3^\circ\text{C}$). Any possible aging effect of the test objects is not considered. The method is suited for analysis of electrical time dynamics from 0.3 mHz to 10 Hz, focusing mainly on electrical dynamics caused by electrochemical mass transport, more precisely diffusion[8].

Discharge pulse test

It is well known that LIBs show significant polarization behavior when subjected to large changes in charge due to high currents or long pulses. To capture this phenomenon, a discharge pulse test is designed according to Fig 2 to expose a strong polarization for ten different operating points over a charge window defined as safe by the LIB manufacturer through upper and lower terminal voltage limits (V_{max} and V_{min} , see Table II). The magnitude of the discharge pulse must be strong enough to reliably capture the voltage response, but within the limits of risking permanent degradation of the cell performance by causing excessive chemical side reactions, depletion or saturation[9].

Equivalent Circuit Model

Three different equivalent circuits are considered, as seen in Fig 1. Each of the circuit alternatives are aimed to approximate the electrochemical diffusion dynamics normally represented by a Randles circuit.

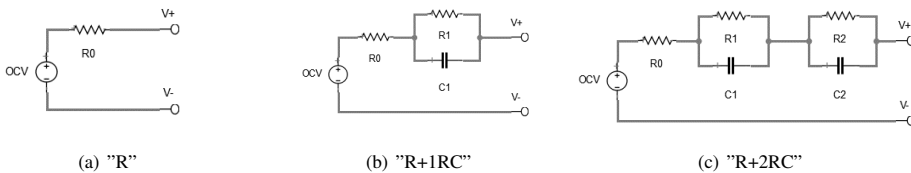


Fig. 1: Equivalent Circuit Models considered.

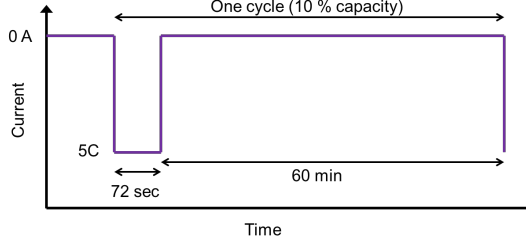


Fig. 2: A typical high-current discharge pulse. Ten consecutive pulses forms one full discharge cycle.

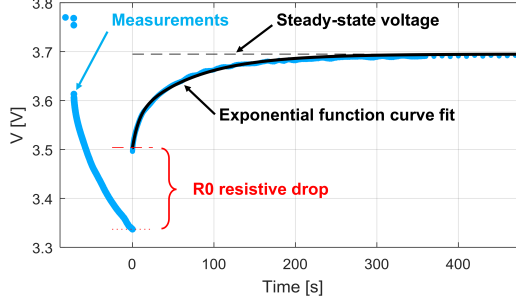


Fig. 3: Curve fit for battery E, pulse no 6 (ca 44 % SOC). The time vector is re-aligned to focus on the relaxation part of the voltage response.

However, to keep the model simple, the circuit elements are constricted to piece-wise linear electrical passives. All parameters are a function of the test objects State of Charge (SOC) and for the purpose of simulation, the parameters are stored in look-up-tables and linearly interpolated between the sampled values. The Open Circuit Voltage (OCV) represents the cells internal average electromotive force, which is also strongly dependent on SOC.

For each discharge pulse, a corresponding voltage response is expected according to Fig 3. For the more complex of the three ECMs (Fig 1(c)), the corresponding electrical parameters to be extracted is OCV , R_0 , R_1 , C_1 , R_2 , C_2 . All parameters are a function of SOC. The parameter extraction is applied on the relaxation part of the pulse only, due to simplicity of having the average cell SOC as constant as opposed to during the discharge pulse. It is assumed that fitting the model to the relaxation part will also give a representative behavior during the discharge part, which is verified later on.

R_0 is extracted by measuring the instantaneous voltage re-bounce from the discharge pulse the first few samples (within 20 ms) of the current turn-off. Knowing the magnitude of the current applied just before the turn-off and the magnitude of the voltage drop gives the resistance through Ohm's law.

The remaining relaxation pulse E_r , short of the R_0 re-bounce, is fed into a curve fitting procedure. A Non-linear Least Square method is used to fit the best curve to the measurement data assuming the following behavior:

$$E_r = a_0 - a_1 e^{-b_1 t} - a_2 e^{-b_2 t}, \quad (1)$$

where t is the time vector (t_0 is at the current interrupt), a_0 is the steady-state voltage after complete relaxation, a_x is the maximum polarization voltage at t_0 , and b_x is the time scaling for link x . a_x and b_x are positive. Time constants for the corresponding RC links are extracted as

$$\tau_x = 1/b_x, \quad (2)$$

where b_x is the time scaling and x is the index of the RC link to be identified. Extraction of the resistance parameters for the RC links is done using

$$R_x = \frac{a_x}{i(1 - e^{-b_x t_{ch}})}, \quad (3)$$

where t_{ch} is the time spend in constant-current discharge before current interrupt, and i is the magnitude of the current used for discharge. In all tests here, $t_{ch} = 72$ s and $i = 5$ C as shown in Fig 2. The exponential function in the denominator represents the amount of bias on the RC link that has been build up during the discharge pulse. Now the equivalent capacitance for the corresponding links is

$$C_x = \tau_x / R_x. \quad (4)$$

These parameters are extracted separately for all pulses and stored in tables as a function of SOC for each battery type. For the single time dynamics ECM in Fig 1(b), the parameters are extracted for two RC links, but the slower one is dismissed. The OCV is sampled at the end of the relaxation; 60 min after the current interrupt event.

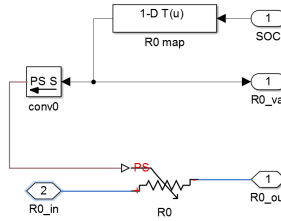


Fig. 4: Implementation of parameter variation over OCV in SimScape

Verification and Validation

After the pulse tests and data processing, a simulation model is populated with the extracted parameters. This simple LIB model is simulated with the same current input as the measurements to visualize pulse-per-pulse model fit, as illustrated in Fig 5. The validation method consists of loading the real cell with a dynamic load cycle and comparing with simulation results. The simulation model implements variable linear passive elements with Simscape as shown in Fig 4. The battery charge level is estimated by coulomb counting during the load cycle and the ECM parameters are extracted from look-up tables using linear interpolation between the discrete SOC points. The load cycle is compiled with test sections for the battery category *PHEV min* from [10]. The LIB is 90% charged at the start of the test and dynamically loaded with the *charge depletion* cycle until a SOC of about 20 % is reached, when the test switches over to the *charge sustaining* cycle. The original cycles consist of constant-power steps cycles with duration of 90 or 360 seconds. These test cycles are repeated to form a test of 2 hours. The result for cell E is shown in Fig 8. The recorded current profile from the physical test is then fed into the simulation model for each of the three ECMs so that the model accuracy for the voltage response can be evaluated. A sampling rate of 10 Hz was used for the current and voltage recording during the physical test. The instantaneous error for each model voltage output (\hat{v}) compared to the measurement (v) is defined as:

$$E = \hat{v} - v. \quad (5)$$

The variance of the voltage outputs is defined as the mean of the square of the instantaneous error

$$V = \frac{1}{n} \sum_{i=1}^n E_i^2, \quad (6)$$

where n is the number of measurement points. The standard deviation of the voltage estimation is defined

through the root-mean of the square of the instantaneous error:

$$RMSE = \sqrt{\bar{V}}. \quad (7)$$

Test Setup

Test objects

Five different LIB variants are tested in this scope, as presented in Table II. All LIBs share the common feature of being power optimized, allowing for repetitive pulse discharge rates up to 10 C. They are all used as energy sources in various kinds of mobile electric propulsion systems. The brand of cell E is obscured by the discretion of a major manufacturer of high-performance automotive cells. In Table II, Q_{nom} is the manufacturer specified charge capacity, V_{max} and V_{min} is the upper and lower cut-off voltages respectively, I_{test} is the selected 5 C test current. U_m is the measured usable energy density, derived by measuring the available constant-current energy within the voltage limits at 1 C current, divided by the volume of the smallest cuboid that can contain the active parts of the cell, i.e. excluding the tabs.

Table II: Test objects overview

Test object	A	B	C	D	E
Brand	Melasta	Electric Power	Tiankang	Tiankang	-
Form factor	Pouch	Pouch	Prismatic	Prismatic	Pouch
Chemistry	LCO/G	LCO/G	LMO/LTO	NMO/LTO	NMC+LMO/G
Q_{nom} [Ah]	10	10	26	28	26
V_{max} [V]	4.20	4.20	2.75	3.00	4.15
V_{min} [V]	3.00	2.75	1.60	2.00	2.80
I_{test} [A]	50	50	130	140	130
U_m [Wh/dm ³]	458	445	152	172	399

Test parameters

New cells are cycled at least 10 time with 1 C constant-current charge-discharge cycles to ensure a minimum of formation[11, 12]. Before each batch of discharge pulses, the cell is charged to V_{max} at 1C constant-current, followed by constant-voltage phase until current falls below C/20. The cell is rested for 1 hour. Each individual cell is tested with the current corresponding to 5 C according to the nominal capacity specified in the manufacturer datasheets, see I_{test} in Table II. All pulse tests are performed with a Digatron BTS-600 battery tester, Matlab is used for data processing and Simulink with Simscape is used for model verifying simulations. The lab setup is programmed to perform intense logging of the voltage response close to the current transients, and declining logging frequency further from current transients in order to save data storage and computational power. Temperature control of the devices under test is limited to passive convection for pulse tests and forced convection for verification load cycle tests.

Results

The exponential curve fit shows high robustness during the capacity extraction procedure. The per-pulse verification displayed in Fig 5 shows a good fit also during the discharge pulse. The initial assumption that the electrical dynamics can be represented with the same linear elements for discharge and relaxation seems to be reasonable.

Looking at the behavior of the time constants for the two RC links over SOC, there is a large variation for especially the slower of the two, as seen in Fig 6. The general behavior can be seen for all chemistries tested. The cells tested during this experiment have not only different chemical properties, but also

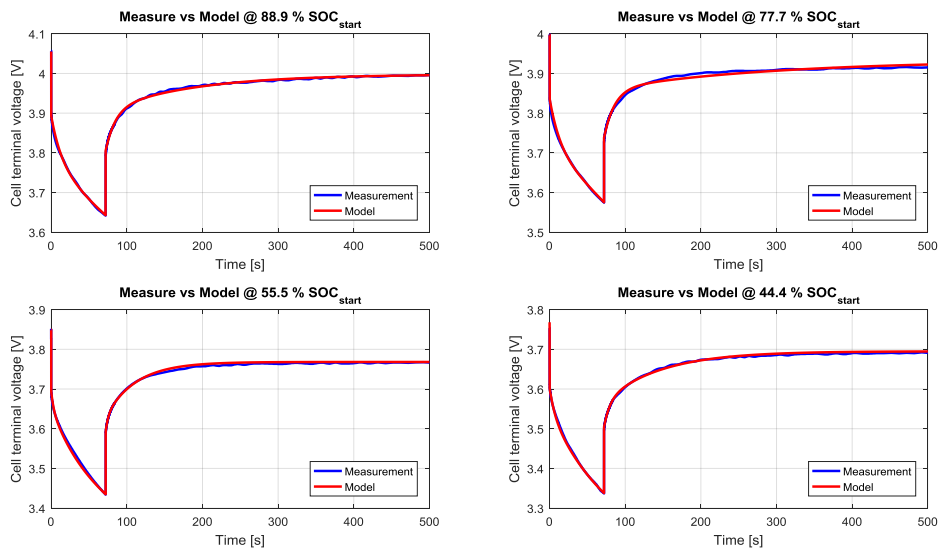


Fig. 5: Per-pulse model verification. Results from cell E.

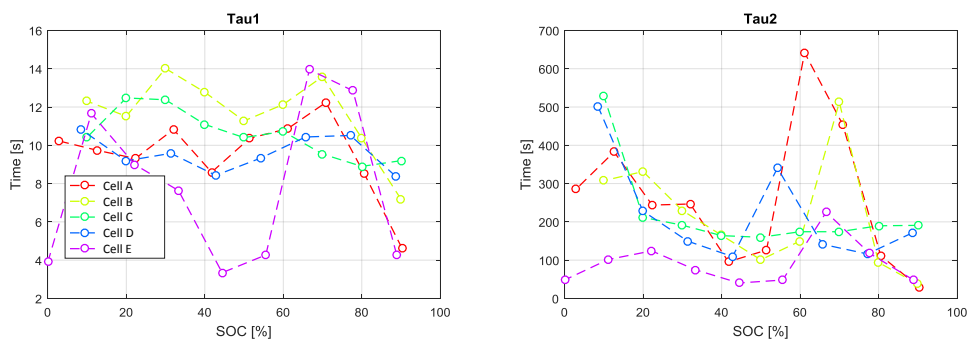


Fig. 6: Extracted time constants for a two-RC-link ECM (1(c)), results for all cells.

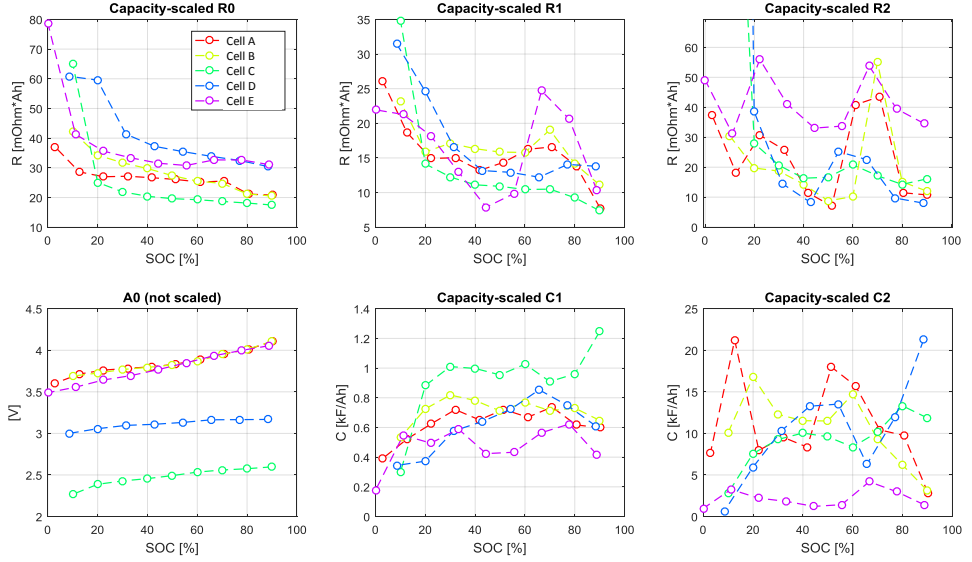


Fig. 7: ECM parameters for all tested cells, using parameter names from 1(c). The parameters are scaled with cell capacity. Circles are sample points and dashed lines are interpolated trends between sample points. A0 represents the OCV.

different physical sizes and charge capacity. In an effort to present the results in a size- and capacity-neutral manner, the parameters in Fig 7 are scaled linearly according to their nominal capacity.

Running model verification with long dynamic load cycles comprised of test sections *chargedepletion* and *chargesustaining* for *PHEVmin* type LIBs from [10] yields a results as in Fig 8. The temperature variation of the cell surface within this cycles is measured to 4.3 °C. An error analysis of the same test can be seen in Fig 9 and the key numbers for model performance for that particular cell is gathered in Table III together with results from similar studies. All of them utilize simple linear ECMs and evaluate voltage error in automotive inspired test cycles.

Conclusion

This study used a simple discharge-pulse technique as the only test method to obtain a large-signal equivalent circuit model for high-power LIBs aimed for automotive applications such as HEVs. Three different ECMs are compared and parametrized through the same test procedure. The parametrized

Table III: Model Performance Evaluation Comparison for LIB ECMs used in drive cycles

ECM type	$Max(E)$ [mV]	V [$10^{-4} V^2$]	RMSE [mV]	Source
R	321.8	8.1	28.4	This study
R+1RC	269.1	6.9	26.25	This study
R+2RC	258.8	1.1	10.65	This study
R	1623	762	276	[6]
R+1RC	296.7	220	148	[6]
R+2RC	218.3	21	45.8	[6]
R+1RC	48.9	1.199	10.9	[4]
R+2RC	-	6.76	26	[7]

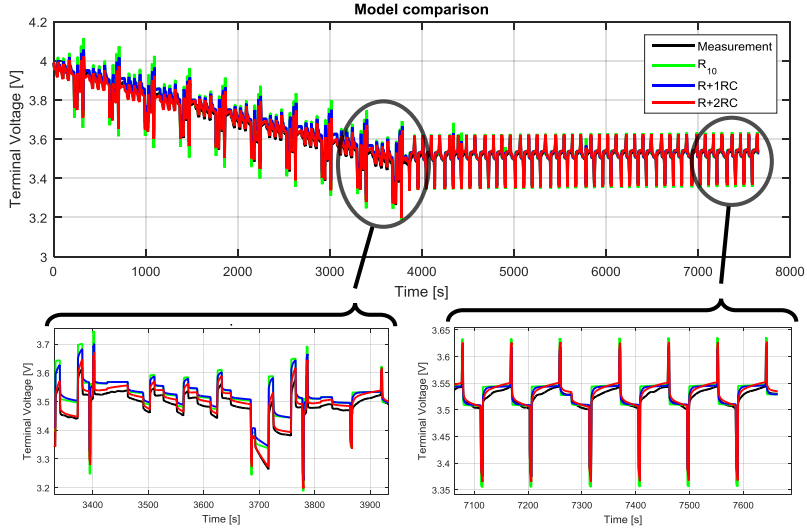


Fig. 8: Voltage response of long dynamic load cycle of cell E. Measurements compared to the three ECMs. The two zoomed-in areas displays the situation where the strongest polarization for charge depletion (lower left) and charge sustaining (lower right) mode occurs. The power scaling is 500 W per cell according to the test procedure[10].

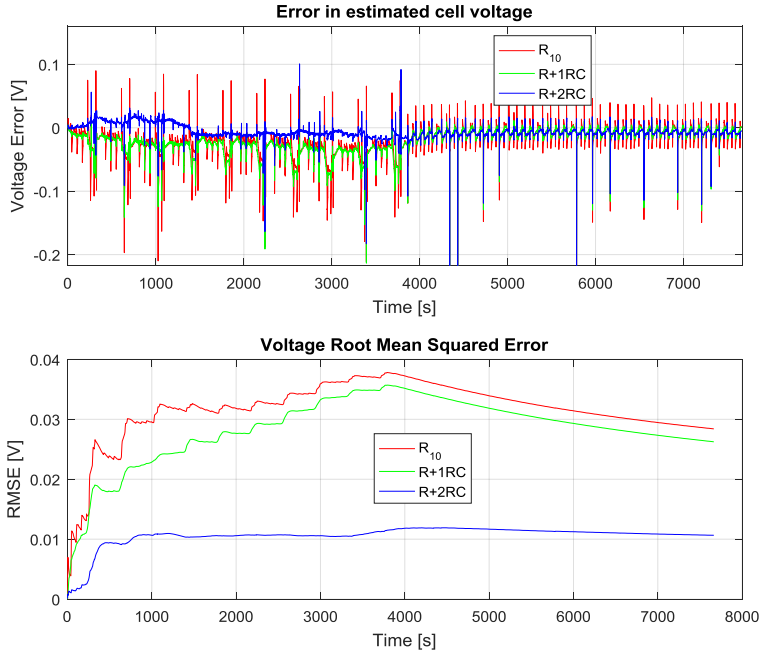


Fig. 9: Error analysis of dynamic load cycle for cell E, comparing measurements with all three ECMs.

model is then compared with measurements of a real cell in a long, dynamic load cycle representing typical HEV usage (Fig 8). The comparison shows that representing diffusion dynamics with two RC links (Fig 1(c)) rather than with a single RC link (Fig 1(b)) decreases the model voltage standard deviation (RMSE) drastically, from 36 mV to 12 mV worst-case in a long load cycle (Fig 9). The accuracy of the model is among the better when compared to other similar studies, as can be seen in Table III. This is even without having any correction for temperature included in this study. To improve the model accuracy further, the parameter extraction can be continued for different cell temperatures.

Regarding the extracted time constants presented in Fig 6, the fast time constant RC link is typically 10 seconds regardless of cell chemistry. The slow RC link tends to capture behavior with a time constant around 100-200 seconds except for cells composed with graphite anodes. It is believed that the active elements in the cell undergoes phase changes associated with graphite at about 70 % SOC that affects the electrical dynamics in this significant way (see also R and C in Fig 7). The corresponding time constant peaks are absent in cells that carries a LTO anodes in this study.

Charge transfer dynamics is not represented by the RC links in this model, but is likely included in the measurement of the R_0 parameter due to the limited bandwidth of the equipment used. The time dynamics for charge transfer for typical LIBs are concentrated to the 10-100 Hz region at room temperature and therefore not particularly interesting when simulating load cycles stretching over hours. For long load cycles that exposes the LIB for a net movement in SOC, typically charge depletion usage, the model accuracy will benefit significantly by implementing a slow time-constant RC link to represent diffusion with very slow behavior.

The limited complexity of the R+2RC equivalent circuit, as presented in Figure 1(c), is a benefit compared to more complex non-linear constant-phase element-based circuits or partial differential equation based physical models when it comes to implementing. This benefit is important when it comes to implementing algorithms to run in real-time in on-board vehicle battery management systems. Estimating the OCV accurately with this kind of model is an important first step in order to estimate the SOC and dynamic current and power limit for a battery in automotive applications.

References

- [1] J. Jang and J. Yoo, "Equivalent circuit evaluation method of lithium polymer battery using bode plot and numerical analysis," *Energy Conversion, IEEE Transactions on*, vol. 26, no. 1, pp. 290–298, 2011.
- [2] R. Bengler, H. Wenzl, H.-P. Beck, M. Jiang, D. Ohms, and G. Schaedlich, "Electrochemical and thermal modeling of lithium-ion cells for use in hev or ev application," *World Electric Vehicle Journal*, vol. 3, pp. 1–10, 2009.
- [3] R. Ahmed, J. Gazzarri, S. Onori, S. Habibi, R. Jackey, K. Rzemien, J. Tjong, and J. LeSage, "Model-based parameter identification of healthy and aged li-ion batteries for electric vehicle applications," in *Proceedings of SAE 2015 World Congress*, 2015.
- [4] F. Sun, R. Xiong, H. He, W. Li, and J. E. E. Aussems, "Model-based dynamic multi-parameter method for peak power estimation of lithium-ion batteries," *Applied Energy*, vol. 96, pp. 378–386, 2012.
- [5] T. Huria, M. Ceraolo, J. Gazzarri, and R. Jackey, "High fidelity electrical model with thermal dependence for characterization and simulation of high power lithium battery cells," in *Electric Vehicle Conference (IEVC), 2012 IEEE International*. IEEE, 2012, pp. 1–8.
- [6] H. He, R. Xiong, and J. Fan, "Evaluation of lithium-ion battery equivalent circuit models for state of charge estimation by an experimental approach," *Energies*, vol. 4, no. 4, pp. 582–598, 2011.
- [7] Y. Hu, S. Yurkovich, Y. Guezennec, and B. Yurkovich, "Electro-thermal battery model identification for automotive applications," *Journal of Power Sources*, vol. 196, no. 1, pp. 449–457, 2011.

- [8] A. Jossen, "Fundamentals of battery dynamics," *Journal of Power Sources*, vol. 154, no. 2, pp. 530–538, 2006.
- [9] K. A. Smith, C. D. Rahn, and C.-Y. Wang, "Model-based electrochemical estimation and constraint management for pulse operation of lithium ion batteries," *Control Systems Technology, IEEE Transactions on*, vol. 18, no. 3, pp. 654–663, 2010.
- [10] J. R. Belt, "Battery test manual for plug-in hybrid electric vehicles," Idaho National Laboratory (INL), Tech. Rep., 2010.
- [11] J. Vetter, P. Novák, M. Wagner, C. Veit, K.-C. Möller, J. Besenhard, M. Winter, M. Wohlfahrt-Mehrens, C. Vogler, and A. Hammouche, "Ageing mechanisms in lithium-ion batteries," *Journal of power sources*, vol. 147, no. 1, pp. 269–281, 2005.
- [12] W. van Schalkwijk and B. Scrosati, *Advances in lithium-ion batteries*. Springer Science & Business Media, 2007.

Paper II

Electro-thermal modeling of high-performance
lithium-ion energy storage systems including
reversible entropy heat

Presented 2017-03-27 at
APEC2017, Tampa, Florida, USA

Published 2016-10-27 in IEEE Xplore:
<http://ieeexplore.ieee.org/document/7931031/>

Electro-Thermal Modeling of High-Performance Lithium-ion Energy Storage Systems Including Reversible Entropy Heat

Stefan Skoog
Electric Power Engineering
Chalmers University of Technology
Gothenburg, Sweden

Abstract—Two of the major heat sources in a high-performance automotive lithium-ion battery cell are parametrized in this study: Joule heat and entropy heat. Established electrochemical models are investigated and experiments are designed to acquire the relevant parameters such as open circuit voltage, entropy coefficient and internal impedance from ohmic losses and mass transport. It is shown that the irreversible joule heat and the reversible entropy heat has a similar magnitude at many operating points for the device tested. The strong influence of irreversible entropy heat has the potential to absorb all the joule heat in currents up to 135 A (C-rate of 13.5) charging and 66 A (6.6 C) discharge in a power optimized automotive lithium-ion cell. It is also shown that, by including the entropy heat in a simple thermal model, the temperature error can be reduced down to 28 % and 44 % for under charging and discharging with high currents, respectively.

I. INTRODUCTION

For high-performance electrochemical energy storage systems (ESS) comprising lithium ion batteries (LIBs) in mobile application, thermal management is a central attribute to design for. Model-based design of battery systems accelerates the design process for complex ESSs, but requires an understanding of how the LIBs behave electrically and thermally under a range of load conditions. Very often, the thermal limits of the cell are specified from a safety point of view to prevent thermal runaway and permanent damage, and even more conservatively set in order to preserve the life time of the LIBs. Basic thermal modeling of ESSs are usually limited to include only irreversible joule losses caused by the internal voltage drop in the battery as a current is driven through the system. On the electrochemical level, more sources of heat are present, and particularly interesting is the reversible effects that can both absorb and emit heat depending on the operating point.

The basics of entropic heat modeling is described by Gibbard[1] and Bernardi[2]. The entropic effect is reported to be strong enough to cancel the joule effect, at least at very low currents (C/5), as reported in [3] and [4]. However, as the technology and performance for especially automotive LIBs is changing fast, the amount of joule heat is decreased per unit of output power the LIB is exposed for. This study aims to find, theoretically and experimentally, if the entropic effect can dominate even at reasonably large currents.

A recent and comprehensive review of the magnitude and effect of entropy heat coefficient is presented by Viswanathan et.al[5]. However, it is hard to find successful non-invasive

attempts of measuring the entropy heat coefficient on full cells in the literature. This paper offers a method to achieve a high-resolution entropy coefficient over virtually unlimited SOC points and over many temperature points.

Calorimetric measurements is a very sensitive and suitable method to measure the entropic effect at small currents, as showed in [3]. However, the limitation is that the method is generally limited to small currents only, which makes it hard to verify the effect in combination with large LIB currents.

This paper investigates the theory behind the reversible entropic heat effect and aims to establish the relevant coefficients through high-precision, non-invasive voltage measurements on commercially available automotive battery cells. The magnitude and significance of the reversible heat is set in relation to the joule heat. The joule heat is established experimentally by parametrization of a piece-wise linear electrical equivalent circuit model.

II. THEORY

A high-performance automotive battery is a delicate piece of interdisciplinary engineering. In this study, the electrochemical-thermal relations will be studied in order to quantify the reversible and irreversible heat that is generated when the battery system is used with high currents (above 1 C) and over a wide State of Charge (SOC) window.

A. Electrical modeling

There is already vast number of methods to electrically represent the behavior of the cell in the literature. The scope of this study promotes the use of empirical equivalent circuit models. A simple Thevenin equivalent circuit (Figure 1(a)) and an extended R+2RC network (Figure 1(b)) is chosen to represent the electrical properties of the cell. The Open Circuit Voltage (OCV) is represented by a variable ideal voltage source mapped with a look-up table as a function of SOC. A R+2RC network provides higher accuracy of the internal voltage drop than a simpler 1RC model, especially when using the cell with large SOC windows as proven in[6]. The time constants of the two RC networks ($\tau_x = R_x C_x$) are chose to represent two different time regions of the mass transport and diffusion part of a typical cell dynamics[7], [6]. In this case τ_1 is in the range of 5-15 seconds and τ_2 about 50-200 seconds depending on SOC and temperature. The time constants typically vary with temperature as especially the R's are highly temperature

dependent [8]. Charge transfer impedance is neglected in this scope as the time dynamics at room temperature and above is typically 1 second and not relevant in relation to the much slower thermal processes investigated here. Instead, the charge transfer dynamics is included in R_0 so that the steady-state dynamics above charge transfer becomes accurate. All electrical parameters are measured with pulse testing, also known as current interrupt method. The data is extracted from voltage responses and stored in look-up tables which can easily be implemented with piece-wise linear interpolation in on-line models.

B. Thermal modeling

A rudimentary way of describing the heat transfer between a cell and its environment is with a 1D lumped-parameter (also known as lumped-capacitance) model such as

$$\dot{q} = c_p m \frac{\partial T}{\partial t} + kA(T - T_\infty), \quad (1)$$

where \dot{q} [W] is the rate of heat generation by the cell, c_p [$J \cdot kg^{-1} \cdot K^{-1}$] is the mass-specific heat capacity of the cell, m [kg] the mass of the cell, T [K] the cell temperature, T_∞ [K] the ambient temperature, k [$Wm^{-2}K^{-1}$] the heat transfer coefficient incorporating both convection and conduction effects, and A [m^2] the equivalent heat transfer area. Radiation is not considered in battery systems since it is of no significant magnitude due to thermal difference between cells and ambient is typically low. The heat generated by the cell is defined as

$$\dot{q} = \dot{q}_J + \dot{q}_E = i^2 R_{tot} + iT \frac{\partial U}{\partial T}, \quad (2)$$

where \dot{q}_J [W] denotes joule heat, \dot{q}_E [W] entropy heat, i [A] current through the cell with charging currents as positive, R_{tot} [Ω] the total resistance of the cells' ECM (Figure 1) after considering the impedance and the history of the current. The entropy coefficient $\partial U / \partial T$ [V/K] is the temperature derivative of the open circuit voltage, which is experimentally established in this paper. The entropy coefficient can be both positive and negative and depends on the SOC of the cell [5]. The product

of the sign of entropy coefficient and current determines if the entropy heat (\dot{q}_E) becomes exothermic (positive) or endothermic (negative). For all operating points in SOC, there exist two cell currents i where the joule heat and the entropy heat cancel each other and no net heat is developed in the cell to alter its average temperature, (2) rewritten:

$$\dot{q} = 0 \Rightarrow iT \frac{\partial U}{\partial T} = -i^2 R_{tot}. \quad (3)$$

The first solution is the trivial $i = 0$, and the second solution becomes:

$$i = -\frac{T}{R_{tot}} \frac{\partial U}{\partial T}. \quad (4)$$

III. MEASUREMENTS

An automotive high-power pouch cell is used as a base for parameter identification and verification. The chemistry is based on a NMC+LMO cathode matched with a graphite anode. The nominal voltage is 3.70 V and the rated charge capacity is 10 Ah. The experimental procedure consists of four steps as described below.

A. Determine entropic coefficient

A high-precision potentiostat (Gamry Reference 3000) is used to charge and discharge the cell over the entire usable SOC window with a rate of 0.1 C (10 hour sweep). The procedure carried out in a thermal chamber in thermal steady-state and is repeated for five relevant temperatures: 5, 14, 25, 34, 45°C. For each temperature, new curves are established and a small but significant difference is expected in OCV. The charge and discharge voltage for each temperature is compared and an average curve is established as the pseudo-OCV vs SOC curve, see Figure 4. The cell manufacturer's voltage limits are slightly overridden in order to guarantee that the average curve contains data at the extreme points 0 % and 100 % SOC. The difference between any two adjacent OCV curves multiplied by the average temperature for the two curves ($T \partial U / \partial T$) forms the entropic potential, and is illustrated in Figure 5.

B. Identification of thermal parameters

The cell is equipped with an external controlled heat source consisting of enameled copper wire with known length and diameter. The assembly also contains a small aluminum plate which also is included in the calculations. Several thermocouples are attached to various points on the cell setup in order to get reliable and comparable measurements. The cell setup is thermally insulated with expanded polystyrene foam and then placed in a passive thermal chamber. The thermal parameters in (1) are successfully identified using a first order exponential curve fit to the controlled heating up process through the copper wire. The setup can be seen in Figure 2 and the resulting thermal parameters are presented in Table I.

C. Identification of electrical parameters

High-current pulse testing is carried out with a Digatron BTS-600 in order to identify electrical parameters within the relevant temperature span. Parameters are stored as 3D look-up tables (typically resistance vs Temperature and SOC), which can be interpolated for in between measurement points. The

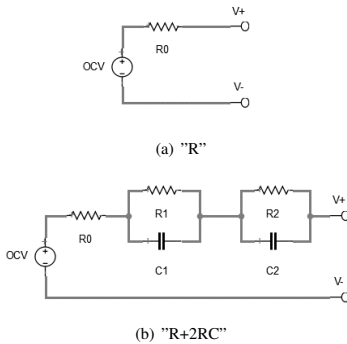


Fig. 1. Equivalent Circuit Models considered. The 2RC network model represent slow-acting diffusion, which is not captured in the simpler model.

procedure of extracting the parameters is explained in detail in [6]. The results for the simple ECM in Figure 1(a) can be seen in Figure 3.

D. Verification of electro-thermal model

The LIB is charged and discharged with a constant current of 4 C (40.0 A) with the battery testing equipment, while in the thermal setup as illustrated in Figure 2. An open-loop model is developed in Matlab Simulink to mimic the behavior defined by (1), including optionally both joule heat and entropy heat from (2). The result from the simulation and measurements is shown in Figure 8. An error analysis is performed using root-mean-square on the difference between measurement and simulation and presented in Figure 9.

E. Results

The total entropy potential, as shown in 5, has a very distinct drop between 0-15 % SOC. This area is particularly interesting to study because it means that the entropy heat at this operating point has the possibility to dominate the joule heat. Similar results are theoretically reported in [5] and measurements in [9] agree with our results. For a fixed current and internal resistance, the relation between entropic heat and joule heat can easily be theoretically established, as in Figure 6. Using (4), the net-zero heat current is calculated for a fixed R_0 at room temperature and shown in Figure 7.

IV. CONCLUSIONS

In the experiments, it is shown how large influence the entropy heat has on the net thermal development of the cell. In the case of a high-power LIB, as theoretically shown here, the cell can act net endothermic for a large portion of the SOC window and for current up to 13.5 C. Similar experiments has also been carried out in our lab on more energy-optimized cells and the result are matching, but the currents are not as high due to a relatively higher internal resistance.

Measurements to acquire the entropic coefficient are successfully carried out and the results presented in Figure 5. The shape and magnitude matches with what is reported previously[5] in the literature for this specific LIB chemistry. The results here have shown an alternative way of measuring the entropic heat coefficient by sweeping voltage with a high-precision potentiostat while keeping the cell temperature

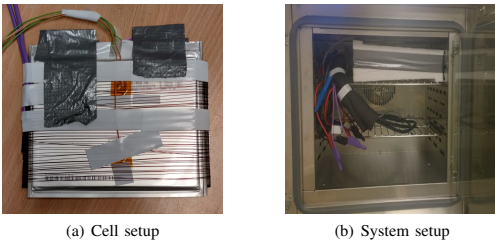


Fig. 2. Cell setup (left) with thermal sensors and including the added copper wire as a reference heat source. System setup (right) in thermal chamber with expanded polystyrene as thermal insulation around the cell.

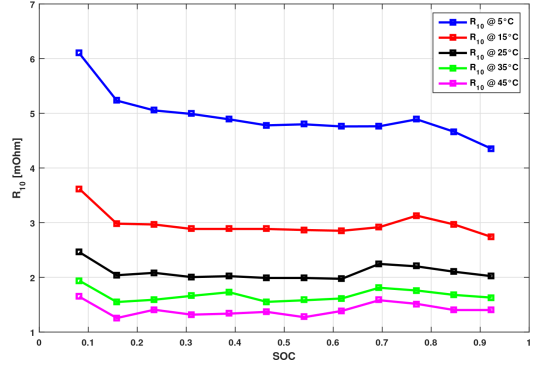


Fig. 3. Equivalent electrical internal resistance of the cell during 10-second, 2 C discharge pulses. Parameters represent the R_0 resistance in Figure 1(a).

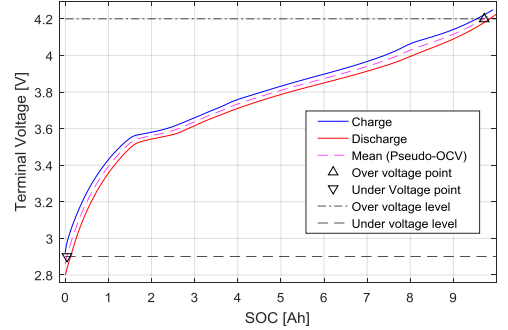


Fig. 4. The process of establishing OCV vs SOC by averaging the two curves from 0.1 C charge and discharge respectively. 0 and 100 % SOC is defined, in this scope, as where the average OCV line intersects the manufacturer voltage limits

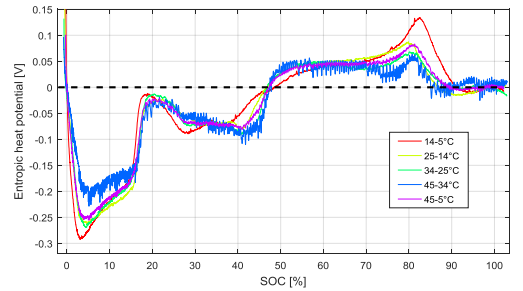


Fig. 5. The established entropic heat potential for all temperatures and all SOC: $T \frac{\partial U}{\partial T}$ in (2) for each temperature case. A negative entropic heat potential together with a positive (charging) current leads to an endothermic entropic heat reaction.

TABLE I. THERMAL PARAMETERS IDENTIFIED FROM (1)

Parameter	Value
\dot{q}	16.7 W
$c_p m$	536 J/K
kA	0.167 W/K

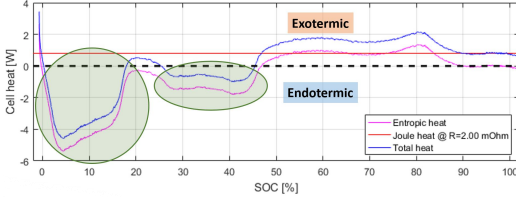


Fig. 6. A simulation with entropy and joule losses compared. The highlighted green areas are operating points where the cell has a net endothermic heat development. Joule losses developed over $R = 2.00 \text{ m}\Omega$ in this example and all heat is calculated with a 20 A steady-state charge current, which corresponds to C-rate of 2.0.

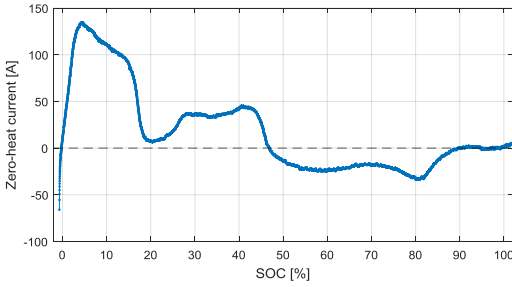


Fig. 7. Cell current where the net heat developed by the cell is zero according to (4), i.e. entropic heat cancels the joule heat. The largest charging current (positive) is 135 A at ca 5 % SOC and largest discharge current 66 A at ca 80 % SOC. The joule heat is calculated using an R_{tot} of $2.00 \text{ m}\Omega$, which is measured for 10-second pulses at 25°C and an average value for all SOC.

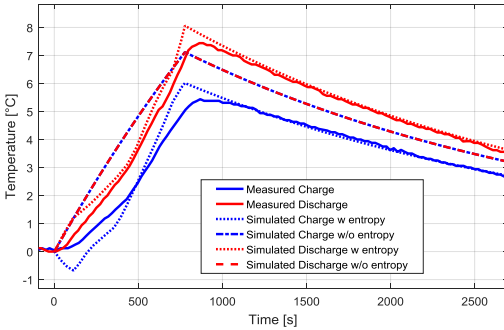


Fig. 8. A comparison of the temperature rise between a thermal simulation model and measurements. The simulation model is executed both with and without the entropy heat component, keeping all other parameters the same. The current used is 4.0 C and SOC window about 4 – 95 %

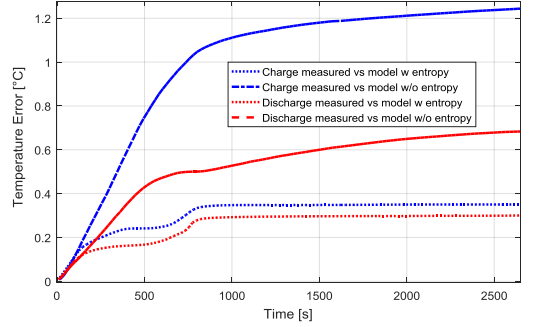


Fig. 9. An error analysis on the output showed in Figure 8. The running root-mean-squared error is displayed for each combination of simulation output, using the measurement as the reference signal.

constant, providing higher resolution over SOC than other easily accessible methods.

In the verification step (Figure 8-9), it can clearly be seen that the entropy heat explains fully why there is a asymmetry in the temperature rise of the battery in two scenarios when the LIB is charged and discharging with current of the same magnitude. When using a simulation model with entropy heat, and the parameters presented in Figure 5, the temperature RMSE is reduced from 1.24°C to 0.35°C , a decrease to 28 %. The discharge error is, under the same conditions, decreased from 0.68°C to 0.30°C , a reduction down to 44 %.

The results show that it is highly relevant to include entropic heat while designing thermal models over LIBs, especially when the operation of the battery includes movement over large SOC windows since the entropic heat coefficient vary significantly over SOC. For small SOC windows and repetitive alternating currents, the entropy change will cancel itself within a time frame represented by a thermal time constant, usually in the range of many minutes and few hours for LIBs. The entropy information can be used to optimize charge and discharge rate limiting strategies for all types of electrified vehicles where the temperature of the battery is considered as a performance limitation. A reason of why the entropy heat have not been given much attention in the literature might be that for many battery types it is an insignificant heat source compared to the joule heat. With the latest commercially mass-produced high-power LIBs, this is not the case as their internal resistance is so small that the entropic heat is dominating in many operating points. The magnitude of the entropic coefficient varies with type of chemistry rather than geometry and performance, as opposed to the joule losses. Cells with graphite anodes typically have pronounced entropy effects, as opposed to those with lithium-titanium-oxide (LTO) anodes. Further on, a combination with lithium-cobalt oxide (LCO) as cathode gives the strongest entropic effects for all common

LIBs on the market. The chemistry analyzed in this work, NMC + Graphite, has a less pronounced entropic effect than LCO + Graphite[5].

An apparent challenge to verify the entropic effect is the challenge of measuring very small changes in temperature within a time frame of seconds. The inherent high thermal inertia posed by the large heat capacity of the cell, makes temperature changes from entropic phenomena very slow and small. A better measurement setup and/or cell-internal temperature probing might be needed to achieve more robust results.

In excess of the thermal consequences of entropic heat, it has apparent consequences on the OCV as well. Variation up to 35 mV are observed during OCV measurements between the 5°C and 45°C at low SOC. At high SOC, a peak of 11 mV of difference in the other direction can be observed at the same temperature conditions. This information is very relevant when designing a high-performance SOC estimator that relies on voltage measurements, regardless of the secondary thermal phenomena.

ACKNOWLEDGMENT

This work is sponsored by the Swedish Governmental Agency for Innovation Systems (VINNOVA).

REFERENCES

- [1] H. F. Gibbard, "Thermal properties of battery systems," *Journal of the Electrochemical Society*, vol. 125, no. 3, pp. 353–358, 1978.
- [2] D. Bernardi, E. Pawlikowski, and J. Newman, "A general energy balance for battery systems," *Journal of the electrochemical society*, vol. 132, no. 1, pp. 5–12, 1985.
- [3] H. Vaidyanathan and G. Rao, "Electrical and thermal characteristics of lithium-ion cells," in *Battery Conference on Applications and Advances, 1999. The Fourteenth Annual*. IEEE, 1999, pp. 79–84.
- [4] C. Alaoui, "Solid-state thermal management for lithium-ion ev batteries," *IEEE Transactions on Vehicular Technology*, vol. 62, no. 1, pp. 98–107, 2013.
- [5] V. V. Viswanathan, D. Choi, D. Wang, W. Xu, S. Towne, R. E. Williford, J.-G. Zhang, J. Liu, and Z. Yang, "Effect of entropy change of lithium intercalation in cathodes and anodes on li-ion battery thermal management," *Journal of Power Sources*, vol. 195, no. 11, pp. 3720–3729, 2010.
- [6] S. Skoog, "Parameterization of equivalent circuit models for high power lithium-ion batteries in hev applications," in *Power Electronics and Applications (EPE'16 ECCE Europe), 2016 18th European Conference on*. IEEE, 2016, pp. 1–10.
- [7] A. Jossen, "Fundamentals of battery dynamics," *Journal of Power Sources*, vol. 154, no. 2, pp. 530–538, 2006.
- [8] C. Fleischer, W. Waag, H.-M. Heyn, and D. U. Sauer, "On-line adaptive battery impedance parameter and state estimation considering physical principles in reduced order equivalent circuit battery models: Part 1. requirements, critical review of methods and modeling," *Journal of Power Sources*, vol. 260, pp. 276–291, 2014.
- [9] C. Forgez, D. V. Do, G. Friedrich, M. Morcrette, and C. Delacourt, "Thermal modeling of a cylindrical lifepo 4/graphite lithium-ion battery," *Journal of Power Sources*, vol. 195, no. 9, pp. 2961–2968, 2010.

Paper III

Experimental and model based evaluation of
mild hybrid fuel consumption gains and electric
machine utilization for personal vehicle application

Presented 2017-08-08 at
ITEC-AP2017, Harbin, China

Published 2017-10-26 in IEEE Xplore:
<http://ieeexplore.ieee.org/document/8080842/>

Experimental and model based evaluation of mild hybrid fuel consumption gains and electric machine utilization for personal vehicle application

Stefan Skoog

Div. of Electrical Power Engineering
Chalmers University of Technology, Gothenburg, Sweden
Email: stefan.skoog@chalmers.se

Abstract—A mild hybrid electric-diesel powertrain for personal vehicles is modeled with respect to longitudinal vehicle dynamics in real-world recorded drive cycles. The potential in terms of fuel consumption reduction in an ideal P0 and P2 mild hybrid electric system is evaluated in order to define the outer boundaries of how much the hybrid topologies can offer. The results are compared with logged data from real-world driving with a prototype vehicle in rural/highway and city drive cycles. The near-ideal powertrain model based simulations offer higher fuel consumption reductions than the prototype vehicle due to the ability of aggressively shutting off the combustion engine during low power requests. The largest reduction of fuel consumption calculated is 41% for a P2 configuration in city driving with a micro hybrid topology as reference. While quantifying the potential gains from an ideal P2 system, the resulting load profile for the traction assist electric machine is also extracted, giving valuable information for the detailed design process of a such machine. Fast cranking of the combustion engine is a key feature for mild hybrids, torque and energy requirements for this procedure is quantified: 1.1 kJ is needed during 300 ms, which is also verified by measurements.

I. INTRODUCTION

A very appealing topology is to combine the relatively high efficiency of a diesel powered internal combustion engine (ICE) with a mild hybrid electric system, to offer a fuel efficient system both at high-speed and at transient city driving[1]. A general study about the effect of electrification through the deployment of a parallel hybrid powertrain in a personal vehicle is presented in [2] and [3], yielding promising results. In [4], a diesel powertrain is electrified with mild hybrid components offering large CO_2 savings and using drive cycle simulation and evaluation. Similar case with a small gasoline ICE is presented in [5] and [6], but the latter without any quantified fuel or performance improvements. According to [7], 48 V P2 systems have the potential to be very cost-effective solutions in increasing the drive cycle efficiency of combustion engine based powertrains compared to the otherwise mainstream solution of incremental technology enhancements of the combustion engine such as downsizing, overcharging and friction reduction of ICE components. While plug-in hybrid end electric vehicle will most likely offer larger environmental alleviations than mild hybrids during the use phase, they are not yet mature enough to reach appealing mass-market prices while maintaining the availability of long-range

driving with fast re-fueling through a widely standardized energy delivery network (i.e. fuel stations).

A. Motivation

In order to successfully design an automotive traction assist electric machine (EM), it is crucial to in detail understand the intended operation, otherwise requiring an unnecessary number of design iteration loops[8] or a compromise in end system performance. A common way of designing electric machines is with incremental improvements; to start with something known and tweak the geometry and performance until it fits the application with acceptable performance. The intent of this paper is to, instead, initiate a top-down approach; to try to quantify the power requirements on the ideal traction-assist EM will behave in a mild hybrid system, serving as input requirements for further design studies of EM, power electronics and energy storage. As a measure of finding EM properties that gives compelling system properties, the vehicle fuel consumption is compared as the figure of merit.

B. Contributions of this work

A model-based design of a parallel hybrid powertrain is investigated, and its results is compared to log data from a prototype car equipped with a 48 V hybrid P0 mounted system. The energy and torque cost of cranking is quantified and put into relation to other hybrid features. Fuel consumption reductions are calculated and compared.

C. Mild hybrid topology

A mild hybrid electric powertrain is in this scope designed as a parallel hybrid with one EM assisting a diesel ICE. The electric power distribution net is limited to 48 V and supported by a high-performance lithium-ion battery. By assuming a practical upper limit of ± 310 A peak in the 48 V electric system, a peak power of ± 15 kW is established, which is an important key figure included in the definition of mild hybrid powertrain in this context. The EM is assumed to be a multiphase machine controlled by an adequately sized inverter capable of high-performance current feedback control. The electrical round-trip system efficiency is assumed to be 90%. Different topologies for mild hybrids (P0, P1, P2) are explained in[9] and [10]. Fig. 1 shows an overview of the

two configurations studied in this scope. C1 and C2 are controlled clutches, which in the case of a P2 setup offers the ability to disconnect the combustion engine and run solely on electric power for as long as the energy storage and power limits permits. Table I shows a summary of hybrid powertrain features that can be expected from three different layouts. A micro hybrid is the baseline and represents most modern premium cars today equipped with automatic start/stop of the ICE. A P0 mounted EM has the disadvantage of being permanently connected to the crankshaft of the ICE, hence forced to overcome the considerable internal friction of the ICE during regeneration and motoring of the wheels. However, the P0 position offers significant benefits during installation and integration of the powertrains from the vehicle OEM perspective, making it an attractive topology to implement mild hybridisation. The P2 topology is the single-machine setup that offers most functionality and the only setup within this scope that offers limited-power full hybrid features such as electric driving and extensive regenerative braking. These features are summarised in Table I.

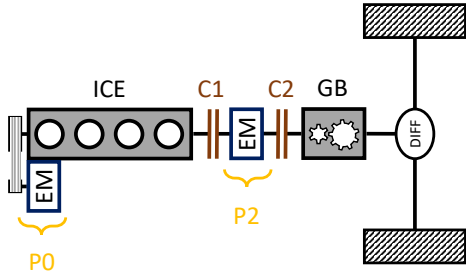


Figure 1: Two parallel hybrid electric topologies suitable for mild hybrids: P0 and P2 are possible positions for one electrical machine. C1,2 notes possible position of controlled clutches.

II. MODEL

A numerical model covering the fundamental longitudinal vehicle dynamics of a typical personal vehicle using Matlab Simulink is utilized in this study. The concept is described in [11] and an open version of the toolbox is available [12]. The main inputs to the model is a driving cycle describing driving speed versus time profile. For each component represented in the vehicle model, relevant speeds, torques and losses are calculated from input parameters. A backward model approach is used for simplicity, implying that for each sample point, the requested drive cycle speed explicitly represent a vehicle force and hence an engine torque. This setup is suitable for early concept studies when the component models only represent limited dynamics. The backwards vehicle model does not require a driver model nor a vehicle feedback controller, as long as the requested speed profile is reasonably aggressive, which is the case during the used drive cycles.

A. Vehicle powertrain topologies and features

In order to quantify energy gains with the two different mild hybrid topologies, a small number of features are specified as seen in Table I. One important differentiation between a P0 and a P2 topology is that the ICE friction losses makes the P0 inappropriate to propel the vehicle with electric power only. For the same reason, only a fraction of the regenerative power will be available during soft vehicle deceleration. Further on, the P2 hybrid assumes to have most of the essential vehicle support functions transferred to electrical power, e.g. power steering and brake servo. For a P0 hybrid, it is inconvenient to shut off the ICE at higher speeds than 50 km/h due to these essential auxiliary loads. In the feature definition in Table I, Torque (τ^*) and Power (P^*) refers to the request at the input of the gearbox seen from the ICE, and the speed (v) is the linear vehicle speed. The $*$ in the table means very limited regeneration capabilities through the 12 V system. For all models, an ancillary average electrical load of 1.0 kW is assumed as a reference load to the hybrid functions, see Fig. 3. ICE shutdown and re-start is assumed to be fast and seamless in the simulation, however, a filter is implemented to guarantee that the ICE is only shut down when it can remain so for the upcoming two seconds.

B. Internal Combustion Engine Modeling

The fuel consumption of the target vehicle's five-cylinder in-line diesel ICE is represented by proprietary fuel consumption map supplied by the vehicle manufacturer. Maximum torque limits as well as internal friction maps are also represented, making the engine model work in two quadrants for positive speeds. The negative torque component, corresponding to base friction in the engine, is an important factor during evaluation of possible regenerative power, see Fig. 2.

C. Gearbox and its controller

A six-speed automatic gearbox is implemented together with a controller. The efficiency is fixed at 94 %, which is in line with the literature for similar systems [13], [14], [15]. The gearbox controller consists of a rule-based approach which selects the gear that will put the ICE as close as possible to its ideal operating speed, given that it is able to supply the requested torque output and stay within an allowed band of rotational speed. The ideal operating speed is a fixed value as illustrated in Table II.

D. Electric Machine and Energy Storage

The electric machine (EM) performance in the model is determined by two high-level parameters: The maximum power ($EM P_{max}$), and the field weakening range (EM_{FWR}). A P2 position implies direct coupling to the crankshaft, hence the rotational speed dynamics is closely coupled with the limitations in the ICE performance. The EM performance is illustrated in Fig. 2 with the parameters from Table II. In the simulations, the EM is allowed an infinite energy storage. At the end of the drive cycle, any energy deviation in the energy storage is converted to fuel, taking the drive cycle mean

efficiency of the ICE and the electrical efficiency into account. This scheme represents an efficient predictive control of energy storage charge balance.

E. Cranking and rotational inertia

The ICE can be shut down in order to save fuel otherwise lost in idle losses. One of the major benefits with a mild hybrid system is that the ICE can be re-activated automatically fast enough without causing noticeable torque delays for most drivers. In warm ICE conditions, a fast cranking of the combustion engine requires an average torque τ_{crank} to accelerate the ICE and all ancillary rotating mechanical components from standstill up to ignition speed ω_i within target cranking time t_c . This includes overcoming internal friction in the ICE, τ_f , as well as priming considerable rotating inertia I with kinetic energy:

$$\tau_{crank} = I \frac{d\omega}{dt} + \tau_f. \quad (1)$$

The total amount of energy needed to fulfil the crank E_{crank} can be estimated assuming a linear increase of speed from 0 to ω_i as

$$E_{crank} = \frac{I \omega_i^2}{2} + \int_0^{t_c} \tau_f \omega dt = \frac{I \omega_i^2}{2} + \frac{\tau_f \omega_i t_c}{2}. \quad (2)$$

The model used for ICE is based on mean torque over one combustion cycle, hence assuming a fixed number for the base friction τ_f to overcome. The inertia of the ICE is assumed as 60 gm^2 , torque converter pump and impeller and flexplate total 159 gm^2 and lastly the EM rotor inertia translated to equivalent ICE inertia through the belt gearing: 12.7 gm^2 . The total crankshaft-equivalent inertia equals 0.232 kgm^2 . For the specific case of cranking, the inertia must be considered, however, the rest of the vehicle model ignores rotating inertia with the motivation that mass inertia of the vehicle is dominating the driving dynamics.

III. TEST VEHICLE

A premium mid-size (C-segment) premium station wagon with a five-cylinder 2.0 l diesel engine and a 6-way automatic gearbox is equipped with a 48 V mild hybrid system consisting of a P0 mounted (see Fig. 1) EM with integrated controller and inverter, a high-performance li-ion battery and a DC/DC converter. The ladder component replaces the task of a 12 V generator. The hybrid control system allows to emulate a baseline micro hybrid for the sake of reference comparisons, which has been utilized to create the reference fuel consumption presented in Table III. The vehicle is equipped with extensive logging capabilities concerning powertrain signals. For this study, mainly the energy flow to and from the EM is studied. The car model is design to represent the test vehicle and the key properties for vehicle dynamics are summarized in Table II.

A. Drive Cycles

The expected driving behavior has a large impact on the requirements on the design of the electric machine. The prototype car is driven in two different drive cycles; rural/highway

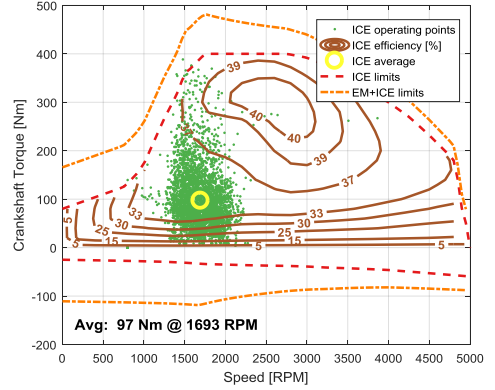


Figure 2: Overview of the torque requested from the ICE during driving of the city cycle according to P2 system simulations. Only a small portion of the ICE rotational speed dynamics is used due to an efficient gear shifting strategy. No negative ICE torques appears due to immediate ICE shutdown during braking.

and city driving as seen in Fig. 3. Each drive cycle is driven twice for micro hybrid and P0 hybrid reference measurements and the repeatability is analysed for consistency. The logged vehicle speed is used as input to the model based calculations for a fair comparison. The speed and aggressiveness of the logged drive cycles is comparable with official drive cycles such as Worldwide harmonized Light vehicles Test Procedure (WLTP) and New European Driving Cycle (NEDC).

IV. RESULTS

Despite allowing an infinite amount of energy buffer in the electrical distribution net, the limited power range and aggressive re-gen strategy, the energy storage energy buffer needed is in the range of 1 MJ (0.28 kWh) when complemented with a re-charge strategy as soon as the ICE is enabled by high propulsion power request by the drive cycle speed profile. However, the amount of energy turnaround during a drive cycle is many times the required capacity: 7.0 MJ (1.9 kWh) in P2 highway/rural according to Fig. 3c. This makes the design requirements of the energy storage quite different to those in electric and plug-in electric vehicles.

The fuel savings for logged P0 and modeled P0 powertrain presented in Table III are within 0.4 and 1.4 percent unit for rural/highway and city cycle respectively. This is considered good modeled accuracy for such a complex mechatronic system as a full car. However, the modelled controller allows for much more aggressive start and stop of the ICE compared to the real car, explaining the larger fuel saving for the model. The remarkable feature is, however, the P2 system performance in terms of fuel saving of 27% and 41% for rural/highway and city driving respectively. This is aligned with previous reported results for a similar system running

Table I: Hybrid topologies and features

Feature	Micro hybrid	Mild P0	Mild P2	Rule
Auto-crank	✓	✓	✓	$v < 10 \text{ km/h}$, $\tau^* \leq 0$
Limited re-gen	*	✓	✓	$P_f < P^* < P_{EMmax}$
Extensive re-gen	-	-	✓	$P^* < 15 \text{ kW}$
ICE shutoff in speed	-	-	✓	$v > 50 \text{ km/h}$, $\tau^* \leq 0$
E-driving	-	-	✓	$P^* < 0.7 P_{EMmax}$

Table II: Vehicle specifications

Property	Value
Car weight	1700 <i>kg</i>
Aero drag (C_dA)	0.661
Rolling friction	0.009
Wheel rolling radius	0.312 <i>m</i>
ICE displacement	2.0 <i>l</i>
ICE max torque	400 <i>Nm</i>
ICE max power	140 <i>kW</i>
ICE idle speed	800 <i>RPM</i>
ICE ideal speed	1250 <i>RPM</i>
ICE max speed	4700 <i>RPM</i>
ICE base friction	28 <i>Nm</i>
EM P_{max}	15 <i>kW</i>
EM _{FWR}	3.0

NEDC[4], and for a gasoline engine in NEDC[3]. The large savings can be addressed to the controllable clutch C1 in Fig. 1, the ICE can be disconnected and disabled at any time during the drive cycle when it is not needed. The mild hybrid system is able to propel the vehicle for the majority of the time in both drive cycles with the allowed 70% of EM max power (10.5 kW). The electrical energy needed to perform this work must be generated at the operating points when the ICE need to start due to high propulsion demand, and the EM adds a generator load of 37 Nm and 3.6 Nm for highway/rural and city cycle respectively.

The decrease of fuel consumption is explained by two factors, using the ICE efficiency as a support variable. During idling (wheel axle propulsion request equals or below zero), the propulsion efficiency of the ICE is per definition zero due to the need of overcoming considerable amounts of internal friction. The mild hybrid system is able to eliminate the vast majority of those operating points by immediately shutting down the ICE. Secondly, when the ICE is enabled due to high propulsion demand, the load is higher due to the additional generator load to re-charge the energy storage, increasing average ICE efficiency generally.

Fig. 4 shows the power profile of the P2 mounted EM compared to the total requested propulsion power. The first observation is that zero and very low power requests are the most common operating points in drive cycles. Next, it can be seen how efficiently the EM is capturing all braking power within its operating range. Positive power requests are also

covered by the EM well, but the small glitch of uncovered, low power request are likely missed due to the persistence rule of not shutting down the ICE too often as explained in Section II-A. Lastly, each graph displays two extra spikes in occurrence. The leftmost at full regenerative power is due to the EM is absorbing braking power at its power limits, and the remaining is taken care of with friction brakes. The second spike in occurrence is due to the need of re-charging the energy storage once the ICE is enabled by the request of high propulsion power.

A. Cranking and ICE base friction

Assuming the ICE idle speed as ignition speed ($w_i = 800 \text{ RPM} = 83.8 \text{ rad/s}$), a target crank time duration $t_c = 300 \text{ ms}$, and an ICE base friction of $\tau_f = 28 \text{ Nm}$, (1) yields $\tau_{crank} = 92.8 \text{ Nm}$ using crank shaft reference frame, and (2) equals 1166 J. Analysis of the logged data during cranking by the 48 V EM results in cranking energies of $1060 \pm 270 \text{ J}$ (one standard deviation). Hence, the base friction power of the ICE equals 2.35 kW at $\tau_f \omega_i$. Through the evaluation of the drive cycles, the number of cranking events and the required energy to support those are analyzed and presented in Table III. The accumulated crank energy over the drive cycle is too small to be displayed in Fig. 3 together with the other hybrid functions.

The mechanical energy needed to overcome engine friction at ICE idle speeds surpasses the cranking energy already after 0.50 seconds of stand-still. Ideally, it means that ICE shut-off should be utilized as soon as the control system can anticipate a driving situation where the ICE is not needed for the next 0.5 seconds. At higher ICE speeds than idle with low loads, the break-even shut-down can be even shorter due to higher friction losses, which motivates an aggressive strategy of ICE shut-down. However, in the physical test vehicle, many obstacles exists which inhibits aggressive in-speed ICE shut-down.

It is also obvious that the amount of energy needed to crank the engine in speed is far below what can be recuperated within the same drive cycle: The extreme example is city driving: 202 crank occurrences (7 times per minute of driving in average) consuming 214 kJ for a P2 model, while the ideal recuperation energy is 3.84 MJ: 18 times the needed cranking energy.

V. CONCLUSION

The results here shows that a mild hybrid system with a P2 configuration has a large potential for energy saving, and even pure electric driving, if it is deliberately designed to overcome functions that might otherwise inhibit the shutdown of the ICE.

Table III: Hybrid topologies and features

Drive scenario	Cranking instances	Total crank energy	Amount of time with ICE off	Fuel consumption
Micro hybrid log rural/highway	7	N/A	6.4 %	5.529 l/100 km
P0 log data rural/highway	6	6.36 kJ	4.8 %	-5.92 %
P0 model rural/highway	25	26.5 kJ	15.0 %	-6.30 %
P2 model rural/highway	163	173 kJ	69.1 %	-26.7 %
Micro hybrid log city	13	N/A	8.4 %	7.217 l/100 km
P0 log data city	26	27.6 kJ	9.2 %	-5.89 %
P0 model city	95	101 kJ	28.1 %	-7.28 %
P2 model city	202	214 kJ	76.9 %	-40.7 %

It makes sense from a fuel consumption perspective to, even in a mild hybrid vehicle, design the propulsion system as an electrical vehicle assisted by a powerful ICE for all dynamic driving situations. The adopted design principle in the industry is likely the opposite.

Implementation of very aggressive start-stop systems can be challenging with respect to ancillary systems and transmission systems, and the performance reserve required by the EM to perform cranking while still fulfilling vehicle propulsion duties must be taken into account as well, not covered in this study. Especially the transmission system control need to be optimized to take advantage of the EM properties instead of only focusing on supporting limitations of the ICE. Further on, to maximise the regenerative braking, an intelligent blending system between EM and friction brakes is needed, which is hard to implement in real vehicles, but very easy in models. This study is focused on a control strategy for minimising fuel consumption, although it should be noted that some aspects of the strategy might be in conflict with minimum emissions or perceived driving performance[16].

All electrical energy needed in the vehicle for auxiliary functions, in our case 1 kW, can be absorbed by maximising the regenerative braking capabilities. This is only possible by implementing a P2 topology together with an aggressive ICE disconnect-and-shutdown control strategy with the options considered here. The remaining energy needed to propel the vehicle electrically during ICE off mode can easily be replenished through an added generator load once the ICE is enabled through high propulsion demand without violating power limits of the ICE or the EM. With the drive cycles used here, the ICE is never enabled through the request from the electrical system other than to assist at higher power propulsion requests.

ACKNOWLEDGMENTS

This work is sponsored by the Swedish Governmental Agency for Innovation Systems (VINNOVA).

REFERENCES

- [1] G. Fontaras, P. Pistikopoulos, and Z. Samaras, "Experimental evaluation of hybrid vehicle fuel economy and pollutant emissions over real-world simulation driving cycles," *Atmospheric environment*, vol. 42, no. 18, pp. 4023–4035, 2008.
- [2] S. M. Lukic and A. Emadi, "Effects of drivetrain hybridization on fuel economy and dynamic performance of parallel hybrid electric vehicles," *IEEE Transactions on Vehicular Technology*, vol. 53, no. 2, pp. 385–389, 2004.
- [3] D. Bücher, W. Meyer, and H.-G. Herzog, "Simulation of the electrical machine's fuel saving potential in parallel hybrid drive trains," in *Electric Machines and Drives Conference, 2009. IEMDC'09. IEEE International*. IEEE, 2009, pp. 653–660.
- [4] D. Gagliardi and C. Wren, "diesel hybrid powertrain for passenger and light commercial vehicles," *MTZ worldwide eMagazine*, vol. 72, no. 3, pp. 4–10, 2011. [Online]. Available: <http://dx.doi.org/10.1365/s38313-011-0022-4>
- [5] P. Bütterling, B. Benders, and L. Eckstein, "Efficient 48-v drivetrain and power net architectures," *MTZ worldwide*, vol. 77, no. 9, pp. 48–53, 2016. [Online]. Available: <http://dx.doi.org/10.1007/s38313-016-0085-3>
- [6] Z. Yafu and C. Cheng, "Study on the powertrain for isg mild hybrid electric vehicle," in *Vehicle Power and Propulsion Conference, 2008. VPPC'08. IEEE*. IEEE, 2008, pp. 1–5.
- [7] J. M. German, "Hybrid electric vehicles, technology development and cost reduction," *International Council on Clean Transportation*, vol. 1, 2005.
- [8] F. Marquez, "Electric traction machine design for an e-rwd unit," Ph.D. dissertation, Lund University, Lund, Sweden, 2014. [Online]. Available: <http://www.iea.lth.se/publications/Theses/LTH-IEA-1072.pdf>
- [9] Y. Yang, X. Hu, H. Pei, and Z. Peng, "Comparison of power-split and parallel hybrid powertrain architectures with a single electric machine: Dynamic programming approach," *Applied Energy*, vol. 168, pp. 683–690, 2016.
- [10] M. U. Lampérth, A. C. Malloy, A. Mlot, and M. Cordner, "Assessment of axial flux motor technology for hybrid powertrain integration," *EVS28*, pp. 202–210, 2015.
- [11] L. Guzzella, A. Sciarretta *et al.*, *Vehicle propulsion systems*. Springer, 2007, vol. 1.
- [12] L. Guzzella and A. Amstutz, "The qss-toolbox v2.0.1," <http://www.idsc.ethz.ch/research-guzzella-order/downloads.html>, accessed March, 2017.
- [13] A. Irimescu, L. Míhon, and G. Pădure, "Automotive transmission efficiency measurement using a chassis dynamometer," *International Journal of Automotive Technology*, vol. 12, no. 4, pp. 555–559, 2011.
- [14] D. H. Park, T. S. Seo, D. G. Lim, and H. B. Cho, "Theoretical investigation on automatic transmission efficiency," SAE Technical Paper, Tech. Rep., 1996.
- [15] A. Moawad and A. Rousseau, "Impact of transmission technologies on fuel efficiency final report," *National Highway Traffic Safety Administration (NHTSA): Washington, DC, USA, Report No. DOT HS*, vol. 811, p. 667, 2012.
- [16] K. Ç. Bayındır, M. A. Gözükküçük, and A. Teke, "A comprehensive overview of hybrid electric vehicle: Powertrain configurations, powertrain control techniques and electronic control units," *Energy Conversion and Management*, vol. 52, no. 2, pp. 1305–1313, 2011.

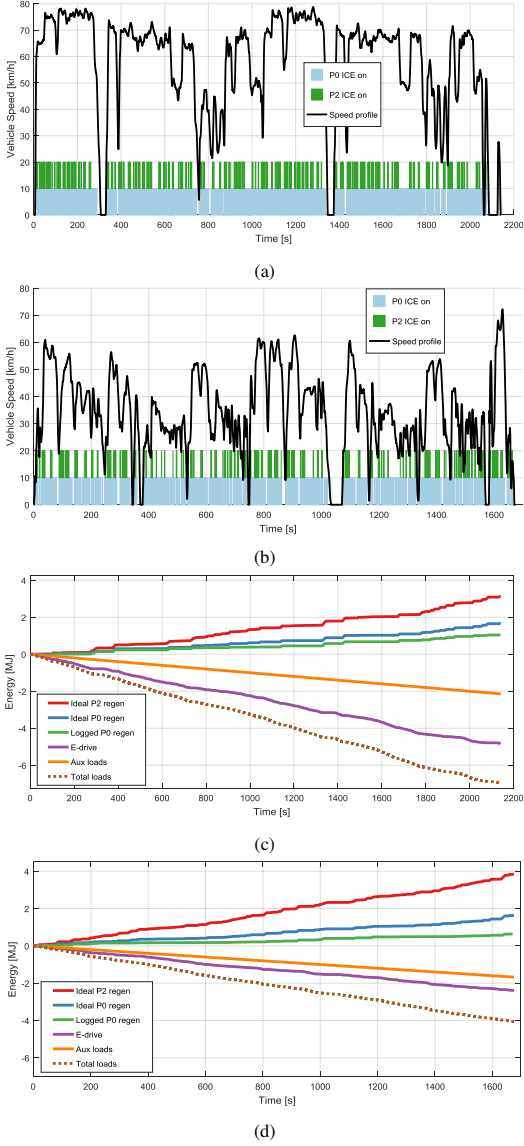


Figure 3: Speed profile for the two logged driving cycles rural/highway (a) and city (b) and their corresponding electrical energy profile (c) and (d). The speed profile is marked with the instances the ICE is needed to operate in P0 and P2 modelled topologies.

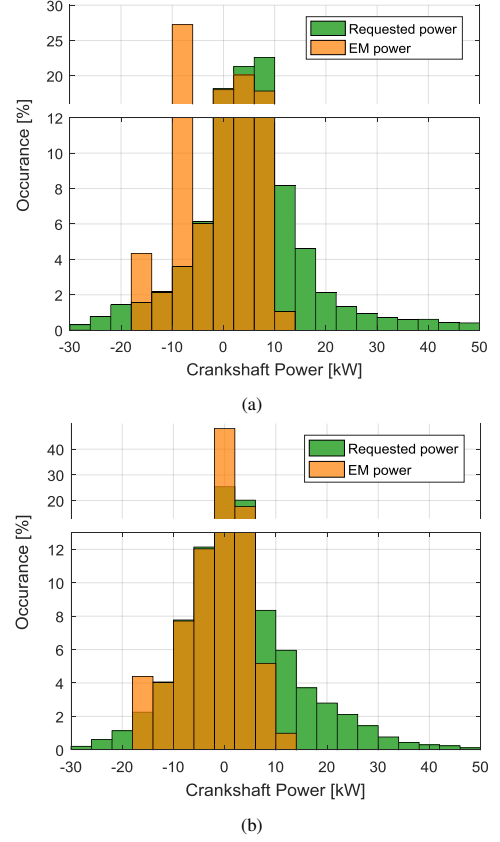


Figure 4: Power distribution during entire drive cycle for highway/urban (a) and city (b). The green background data is requested propulsion power by the vehicle in order to fulfil the drive cycle speed profile. The orange data is requested power by the P2 mounted EM.

Paper IV

Parameterization of linear equivalent circuit models
over wide temperature and SOC span for
automotive lithium-ion cells
using electrochemical impedance spectroscopy

Submitted 2016-10-06 to Elsevier Journal of Energy Storage

Published in Volume 14, Part 1, December 2017

Published 2017-09-22 in ScienceDirect:

<https://doi.org/10.1016/j.est.2017.08.004>

First author contributions

Idea generation, experiment design, paper structure and content,
data processing and analysis, figure generation, corresponding author.

Second author contributions

Data acquisition, EIS data analysis, model fitting and plots.

Parametrization of Linear Equivalent Circuit Models over Wide Temperature and SOC spans for Automotive Lithium-Ion Cells using Electrochemical Impedance Spectroscopy

Stefan Skoog^{a,*}, Sandeep David^a

^a*Electric Power Engineering,
Chalmers University of Technology,
Horsalsvagen 11, 412 96 Gothenburg, Sweden*

Abstract

Three different types of automotive lithium-ion pouch cells are analyzed with electrochemical impedance spectroscopy over a wide range of operating points in SOC (10-90 %) and temperature (-10 to +40°C) with the goal of establishing parameters for an accurate linear equivalent circuit model. The impedance vs frequency is analyzed and attributed to physical behaviors from current collectors, electrode and electrolyte, charge transfer and diffusion. The change of resistance is statistically analyzed as a function of SOC and temperature in an effort to quantify if there is any monotonic patterns. Results show that the charge transfer resistance versus temperature represent the largest relative change of resistance, followed by diffusion resistance versus temperature and the electrolyte resistance over temperature. Only weak correlations with resistance versus SOC are found irregardless of

*Corresponding author

Email address: stefan.skoog@chalmers.se (Stefan Skoog)

frequency range. Frequency-domain fitted equivalent circuit model parameters are evaluated by comparison of physical measurements in long dynamic load cycles using root-mean-squared of the voltage error between model and physical measurements as performance index. A simple $R+2RC$ model capturing diffusion dynamics performs best at RMSE 15.46 mV , better than most similar studies and better than the more complex $R+6RC$ also evaluated.

Keywords: Battery impedance, Electric impedance spectroscopy, Automotive lithium ion battery, Equivalent circuit model, Charge transfer

1. Introduction

1.1. Background

Vehicle electrification is a powerful method of reducing greenhouse gases emissions while preserving the availability of personal mobility. A key component in an electric or hybrid electric vehicle is the Energy Storage System (ESS), which in most modern cases is constructed by a plurality of lithium ion cells forming a Lithium Ion Battery (LIB). An important challenge in mobility applications is to maximise the reliability and electrical performance of the LIB at the same time as minimising the size and weight. The vehicle installation cost of a LIB can be kept at competitive levels if the number of cells as well as the size of each cell is kept at its minimum for the given use case. In order to optimize the electrical usage of the battery in terms of power and allowed energy window during the design process, a model based design methodology is advantageous. Selecting the right model and populating it with parameters through reference measurements is critical for the

design process of the ESS. Knowing how the battery cells will behave as an electrical component over a wide range of temperatures and State of Charge (SOC) levels is therefore very relevant early in the design process. When the LIB is operating in the vehicle, an on-line Battery Management System (BMS) must be employed in order to guarantee safety and preservation of performance of the cells. Real-time, accurate electric models are needed to execute as a part of the BMS software to fulfil its objectives.

Equivalent Circuit Models (ECMs) are commonly used to represent the electrochemical behavior of a LIB. ECMs are suitable as an alternative to physics-based partial-differential equation (PDE) modeling. If the elements in the ECM are chosen as standard linear elements, and its parameters stored in look-up-tables (LUT) or simplified linear relationships, they are much more suitable to run on-line in vehicle applications for the purpose of estimating SOC and maximum power. One challenge with this setup is to keep the complexity of the parameters on a reasonable level, as they vary with frequency, temperature and SOC as shown in this study. Even though ECMs would normally be considered as black-box models without any physical representation of its parameters, careful investigation and analysis can lead to connecting the circuit elements to the electrochemical properties of the cell. Electrochemical Impedance Spectroscopy (EIS) is a powerful, non-invasive method of measuring the internal impedance of a LIB. The data acquired from EIS can be analyzed and used to populate circuit elements in ECMs in parallel with identifying high-level electrochemical phenomena. An obvious challenge for real-time implementation is the balance between complexity of the model (execution time) and the amount of parameters stored in look-up

tables (storage memory).

1.2. Previous work

EIS has been used for LIBs previously in the literature for various purposes. A nice introduction to EIS for the purpose of analyzing LIBs can be found in [1, 2, 3, 4, 5]. Fitting EIS data to ECMs are discussed in [6, 1] for linear models and [7, 8, 5, 1] for non-linear models. A comprehensive review of utilizing EIS for LIB state-estimation can be found in [9, 10]. However, there is room for debate in the literature between the complexity of the ECM used and the performance in terms of minimizing the estimated mean voltage error of the LIB model.

Low temperature performance of LIBs have been investigated in [11, 12], and specifically for NMC/G in [13]. An overview of the specifics of charge transfer dynamics for a few variants of LIBs is presented in [11]. However, little information is found about the electrolyte and diffusion dynamics for commercial cells as a function of temperature.

Ageing is not considered in our scope, however, good sources for impedance implications of ageing in high-performance lithium-ion cells in automotive applications exist for NMC[14, 15], LFP[16], LNO[17], LTO[18]. Also, specific calendar ageing for several commercially available cell types (NMC, LMO/NMC, NCA, LFP) are evaluated in [19].

In [14], measurements on high-performance automotive cells and their change in impedance over large variations in both state of charge and temperature are evaluated. It is, however, still rare in the literature to present results on different variants within the lithium-ion family of batteries, using the same methods, analysis and tools to measure impedance, acquire ECM

parameters and state estimation. Due to the high sensitiveness of EIS equipment, it is according to our understanding and experience hard to compare measurement results from different labs using slightly different methods and machinery.

1.3. Contributions of this paper

1. Measurement and analysis of LIB impedance behavior over a wide range of frequencies (10 mHz to 10 kHz), SOC (10-90 %) and temperatures (-10 to +40°C) relevant for automotive usage
2. Performance comparison of three mass-produced automotive LIBs, using identical methods and evaluation techniques
3. Quantification of the impact from SOC and temperature on resistance, and addressing it to the three main physical phenomena simplified through frequency range decomposition: Electrolyte, Charge Transfer and Diffusion
4. Parametrisation of linear ECMs through EIS measurements, validation of model error through long drive cycles with successful results compared to literature.

2. Cell impedance modelling in the frequency domain

2.1. Electrochemical Impedance Spectroscopy (EIS)

EIS is a valuable tool for non-destructively observing and quantifying various phenomena occurring within a electrochemical cell. It involves imposing a small sinusoidal voltage at a given frequency on the cell, while measuring the resulting current. With the fair assumption of a linear impedance response, the fundamental impedance signal with both phase and magnitude

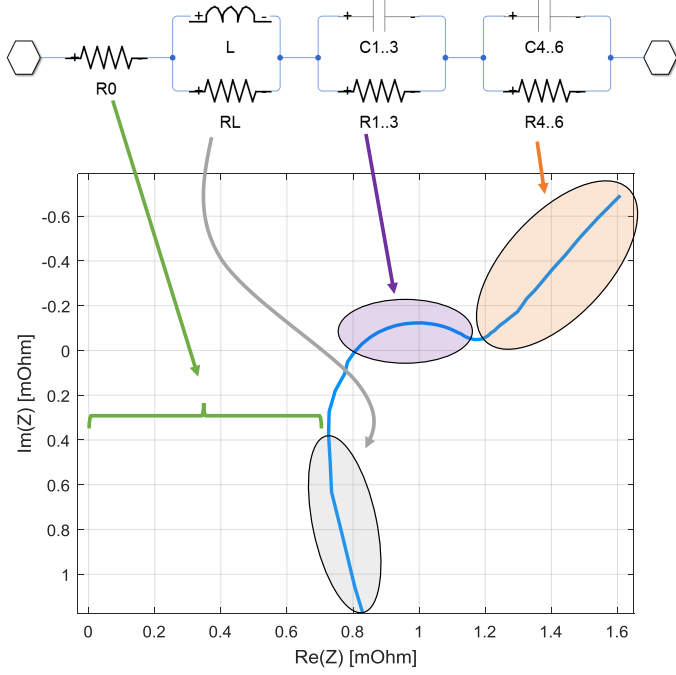


Figure 1: Linear equivalent circuit model used to fit the measured impedance of the cells. By including only a sub-set of the RL and CL links, the two models used in this study can be formed. The blue curve is a measurement from cell A at 51 % SOC, 24°C

can be extracted for any given excitation frequency. By sequentially applying a wide range of frequencies, normally a few millihertz to a few kilohertz, a characteristic impedance spectrum can be obtained and illustrated through a parametric frequency response plot (Nyquist plot), see Figure 1 on page 6. This method is time consuming but can be automated with modern tools and equipment.

An ECMs structure using a plurality of linear circuit elements to mimic the measured frequency response from LIBs is also illustrated in Figure 1

on page 6. Several circuit elements are generally needed in order to cover the wide frequency dynamics of LIBs. Both linear and non-linear circuit elements can be used to model the behavior depicted by the spectroscopy measurements.

2.2. Linear vs non-linear models for the frequency domain

While trying to design ECMs which replicate EIS measurements accurately in the frequency domain, researchers generally include at handful of Zarc elements. Each Zarc element consists of a Constant Phase Element (CPE) in parallel with a resistor[7, 12, 16, 15]. The resulting non-linear models used in the frequency domain are not trivial to transfer in time-domain simulations. Approximation using several linear elements can be used[7, 1, 4]. In order to be able to use detailed models on-line in vehicle battery-management systems, it is favorable to keep them simple with as few parameters as necessary. However there is no accurate and simple representation of CPEs in the time domain and therefore most researchers utilizing EIS find it hard to physically interpret their results, especially at lower frequencies (below 2 Hz). Understanding cell behavior from EIS measurements at lower frequencies is crucial for automotive applications where drive cycles which typically lasts dozens of minutes.

Buller[4] found that it is possible to find approximations for a Zarc using only resistive (R) and capacitive (C) elements. He suggests both five RC and three RC link based networks whose values when chosen suitably become equivalent to a Zarc. The five RC link based model is more accurate in the frequency domain, but the three RC link based one is more computationally

efficient since it involved lesser number of parameters. In addition, Buller validates both models in his work and suggests that the three RC network is recommended as the general simulation tool for replicating the behavior of a Zarc. With these conclusions, our template for a general ECM as shown in Figure 1 on page 6 consists of six RC links in total, wherein links 1 to 3 are used to model the mid frequency range and links 4 up to 6 are used to model the low frequency range. This $R + 6RC$ model is an approximation of a 2-Zarc circuit.

The resulting six RC link based ECM still contains a lot of information if one consider that all the parameters can depend on both SOC and temperature, and according to some studies, also current[9, 4]. In [7], the authors introduce a simple ECM based on three RC links. Their work concludes that even though their simple ECM is not able to accurately reproduce the impedance in the frequency domain, it performs very well in predicting cell voltage and cell performance in the time domain. Working along the similar lines of linear simplified ECMs, a further simplified $R + 2RC$ link based model is proposed in this paper, wherein a fixed resistance R_{DC} and two RC links are together used to represent the EIS measurements at low frequencies alone, since frequencies higher than 2 Hz are not very relevant in automotive applications. Here, the first three RC links from the $R + 6RC$ model are removed and their resistances alone are added to the value of the ohmic resistance, so that the previously denoted R_0 is replaced by R_{DC} . The capacitances which are associated with the first three links are representative of the double layer capacitance (C_{dl}) [16, 15] and charge transfer, and

are neglected in this simplified low-frequency model. Time constants of the diffusion dynamics in the cell are significantly slower than the double layer and charge transfer dynamics, but matches better with the fundamental frequency content of automotive drive cycles. Hence two RC links are dedicated to replicate this region of the spectra. The proposed simplified ECM consisting of a series combination of a single resistor and a pair of RC links is commonly referred to as the dual polarisation (DP) model. The DP model is generally parametrised using time domain techniques such as pulse testing. However the contribution from this paper is using EIS data within a limit frequency range from the spectra to parametrise it.

2.3. Comparing impedance points

When comparing impedance points of interest within a cell for different operating points (SOC, temperature), a statistical approach is used using the arithmetical mean (μ) and the associated standard deviation, which is defined for N number of x_i individual sample values as

$$\sigma = \sqrt{\frac{1}{N-1} \sum_{i=1}^N (x_i - \mu)^2}. \quad (1)$$

2.4. Quantifying model-fitting

In order to quantify the model fit or in other words the error between the measured (x_i) and modelled (\hat{x}_i) results, the root-mean-squared error (RMSE) is calculated as

$$RMSE = \sqrt{\frac{1}{N} \sum_{i=1}^N (\hat{x}_i - x_i)^2}. \quad (2)$$

3. Measurements

3.1. Test setup

All measurements are performed on single li-ion cells. Three different, automotive classed, high-performance li-ion cells are evaluated. All of them are pouch form factor with both tabs on a short side of the pouch. The list of the Devices Under Test (DUT) for the experiments performed in this paper, together with their basic properties is shown in Table 1 on page 10. Unfortunately, only a limited set of data can be shared about the cells due to supplier confidentiality. Previous ageing of these cells is limited to calendar ageing during storage. Apart from that, the cells are assumed to be at their beginning of life state, and no considerations have been done to address the aging effects into the interpretations of our measurements.

EIS measurements on the selected cells are performed using a high-precision potentiostat; Gamry Reference 3000. The thermal chamber used is a Pol-Eko ILW53. High current tests are done with a Digatron BTS-500.

Table 1: Test objects used

DUT	Capacity [Ah]	Nominal Voltage [V]	Form factor	Chemistry
A	30.0	3.7	Pouch	NMC/G
B	25.7	3.7	Pouch	NMC+LMO/G
C	19.5	3.3	Pouch	LFP/G

3.2. Procedure

EIS is performed with 61 frequency points distributed evenly in a logarithmic scale between 10 mHz to 10 kHz. The potentiostat excitation is

typically 1.5-2.0 mV RMS and below 3 A. Before the EIS experiments, the cells to be tested were subjected to basic forming which consisted of at least 10 full charge-discharge cycles at 1 C at room temperature. Each EIS sweep is performed at about 12 SOC points per temperature, and for ca 7 different temperatures between -10°C and +40°C for each cell, resulting in 259 EIS curves, in total 16000 individual impedance sampling points.

Before each experiment, the cell is placed in a dedicated holder and then housed in the thermal chamber, which maintains the desired temperature, and is allowed up to six hours of rest to ensure thermal equilibrium. A constant-current charge/discharge at C/10 is performed to reach either the upper or lower voltage limits specified by the cell supplier. An electrical resting period of 30 minutes is necessary before the actual EIS sweep starts. After each frequency sweep, the cell is charged or discharged at C/10 to reach a new desired SOC level, and then again rested for 30 minutes, and the sequence of tests is repeated until it reaches the cut-off voltage. EIS sweeps are subsequently alternated between high SOC to low and from low to high between different temperature set points, which saves test time. Since the capacity is expected to change slightly with temperature, a new SOC and capacity was estimated and corrected for each sweep by automated scripts by correlating the Open Circuit Voltage (OCV) measurements.

The geometric details of the electrodes are identified by, after the completion of all electrical test, opening up the cell packages and measure the sizes of the current collectors with a micro meter.

4. Analysis

All EIS measurements share a similar impedance behavior, as can be seen in Figure 1 on page 6. The general behavior as an inductance ($Im(Z) > 0$) at higher frequencies, above 1 kHz, arise mainly from geometrical properties of the electrodes. For medium frequencies, 1-1000 Hz, a half-circle in the complex impedance plane is generally found that originates from double layer effect such as charge transfer in the electrodes[2], which originates from porous electrodes[20]. Only one half circle is observed in all test cases in this study. From the literature, some cells display one smaller and one larger half-circle in this frequency range, where the smaller half-circle originate from SEI layer effects on one of the electrodes [3, 15]. For warmer temperatures, above 30°C, the only half-circle observed is generally so depressed that it is indistinguishable from other impedance patterns and not easily identifiable with the methods used here.

After the charge transfer half-circle, moving down in frequency and to the right in the complex impedance plane, a tail shows up which seems to be growing with an angle approximately at 45 degrees until the lowest measurement frequency occurs, in our case 10 mHz. Mass transport such as ion diffusion is responsible for the sloping tail behavior. The frequencies and the absolute impedance values of where all of these typical phenomenas occurs depends strongly on temperature and weakly on SOC.

4.1. Points of interest

An effort has been made in order to quantify the SOC and temperature dependence of the impedance for all cells specified in this work. For

all measurements, the most interesting points in the impedance spectrum have been automatically identified and analyzed. Each impedance point (Z) contains information of frequency (f), resistance ($r = Re(Z)$) and reactance ($x = Im(Z)$). Re and Im symbolizes, respectively, the real and the imaginary operator on an impedance (Z) represented by a complex number. In a similar fashion, r_a represent the real (resistive) part of Z_a , which in hand represents the impedance at frequency point a . The points of interests are graphically represented in Figure 2 on page 16 and are explained here:

- Z_{cc}

The resistance of the metal parts of the electrodes; the current collectors. In this study, this resistance cannot be measured separately but is instead modeled from the known geometry of the electrodes, see section 4.2.

- Z_a

Minimum resistance measurement point, occurs typically around 1-3 kHz according to our experience. The resistance at this point is physically represented by the contact resistance in the current collectors (r_{cc}), the electrode active material, separator and the electrolyte [11, 3]. For ECMs including high frequency dynamics, this point should be used to extract the minimum resistance while simultaneously respecting the resistance contributed from equivalent capacitors and inductor networks. It is identified in the EIS sweep as $min(Re(Z))$

- Z_b

Zero-reactance point. This is the only point within the evaluated fre-

quency range where the impedance crosses the imaginary axis, i.e. translates from inductive to capacitive behavior with decreasing frequency. Many ECMs in the literature focus on low to medium frequencies use this point as the lowest resistance. This point is also often referred to as R_Ω by others. Identified as $Im(Z) = 0$.

- Z_c

The local maximum in (capacitive) reactance for the charge transfer half-circle. This point does not exist for all cells at all temperatures, but it is generally prevalent at room temperatures and below. The physics behind this point is impedance in SEI layer and charge transfer impedance which occurs when the Li^+ ions move from the electrolyte to the electrode[11]. Identified as $max(-Im(Z))$, $f(b) < f(c) < f(d)$.

- Z_d

Local minimum (reactance) of charge transfer half-circle. This valley in the complex impedance plane is usually wide from a frequency perspective, where a lot of EIS sampling points are focused. It physically represents the transition between double layer effects and mass transport effects and it is known to vary widely with temperature and age[15]. Identified as $min(-Im(Z))$, $f(d) < f(c)$.

- Z_e

This point is a fixed-frequency point rather than coupled to a specific physical phenomena or breakpoint. The 100 mHz impedance can be of significance for rudimentary Thevenin-based ECMs comprising of only one internal resistance. This would represent the fundamental

frequency of a 10-second current pulse. The 10 second time window is particularly interesting in vehicle applications since it represents the length of a typical acceleration or deceleration of the vehicle. Since this is a fixed-frequency point, it might end up on either side of point d in the Nyquist diagram depending on temperature and SOC of the cell.

- Z_f

The slow-diffusion impedance is interesting particularly when compared in relation to point d . The slope and length of the diffusion tail typically varies with SOC and temperature. The point is identified as $\min(f)$, in our case 10 mHz.

In addition to the measurement points, composite variables are formed that will form the basis of our analysis.

- $r_{ele} = r_a - r_{cc}$

This represents the resistance in the electrolyte, SEI layer and active material in the electrodes. It is based on the minimum-resistance measurements in point a, but with the modeled current collector metallic resistance subtracted.

- $r_{ct} = r_d - r_a$

Charge transfer resistance is defined as the diameter of the half-circle along the real axis in the Nyquist diagram[21, 10].

- $r_{diff} = r_f - r_d$

The resistance of the diffusion tail is formed by taking the difference between the lowest frequency impedance measurement (point f) and the end of the charge transfer half-circle (point d).

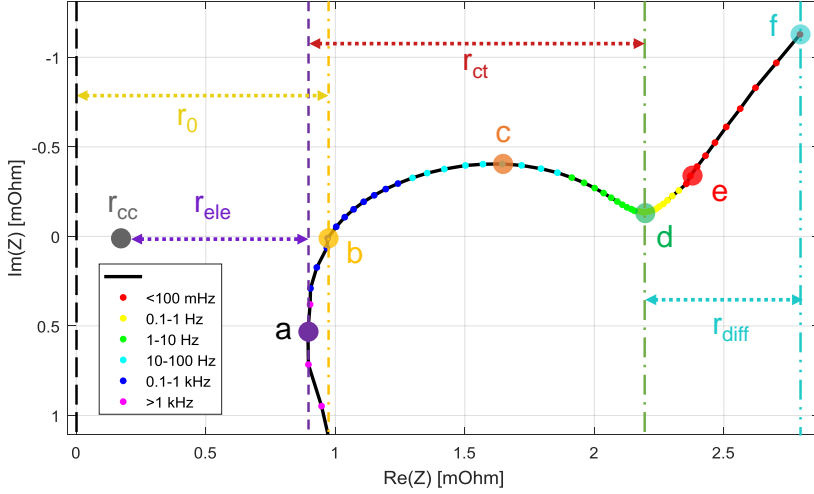


Figure 2: Point of interests on a typical EIS sweep. Measurement are for cell B at 41 % SOC and 6 °C with linear interpolation between sample points.

4.2. Electrode and Current Collector

As mentioned in section 4.1, the current collectors constitute a part of the measured r_a resistance. By analyzing the internal geometry of the DUTs and assuming an even current distribution along the current collector, the resistance for the current collectors (r_{cc}) can be estimated. It is assumed in this scope that the current collectors have no impedance change with the level of charge in the cell and no impedance change over the relevant frequency range. The exact sizes of the current collectors used for calculation cannot be disclosed due to discretion of the manufacturers. However, common thicknesses for automotive pouch cells is 20 μm for positive aluminum cathode[22] and 12 - 14 μm for negative copper anode[23, 22] are relevant numbers to use. Dozens of layers of full electrochemical cells are usually stacked within

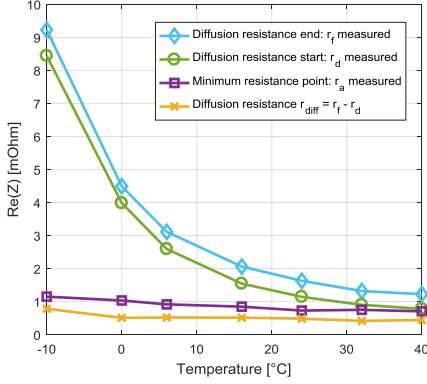
one pouch, forming many parallel strands of individual current collectors. The temperature dependence of the current collectors are included in the resistance estimation as

$$r_{cc} = \rho_{20} \frac{l}{As} \left(1 + \alpha_{20}(T - 20) \right), \quad (3)$$

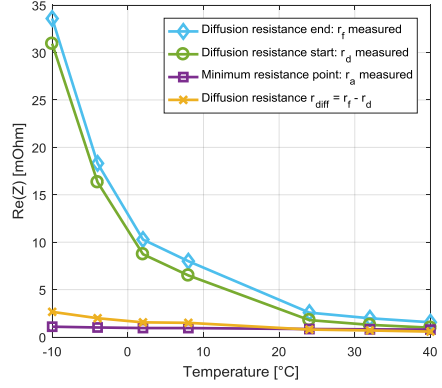
where ρ_{20} is the material resistivity at $20^\circ C$, l is the equivalent length of the current conductor, A the cross section area, s the number of stacked full-cells in one pouch package, α_{20} the material temperature coefficient at $20^\circ C$, and T is the material temperature. For the two relevant materials, $\rho_{20} = 4.30 \cdot 10^{-3} K^{-1}$ and $\rho_{20} = 3.90 \cdot 10^{-3} K^{-1}$ are used for aluminum and copper respectively. The material resistivity numbers used are $2.65 \cdot 10^{-8} \Omega m$ and $1.72 \cdot 10^{-8} \Omega m$ for aluminum and copper respectively. For the equivalent length, it is assumed that half of the current collector height is effectively used to transport current to the tab(s). Since two full cells inside a typical pouch cells share one electrode and current collector, the effective thickness is halved in the calculation of the cross area A . The calculated current collector resistance at room temperature constitutes about 19 % of the total measured r_a .

4.3. Diffusion resistance

The difference in resistance between the 10 mHz sample point f and the end of charge transfer point d in Figure 2 on page 16 symbolises the isolated diffusion resistance of the cell: r_{diff} . Analysing the impedance trend of point f only gives little understanding of diffusion dynamics, since the charge transfer dynamics r_{ct} is dominating for most operating points.



(a) Cell B at 49.3 ± 1.61 % SOC



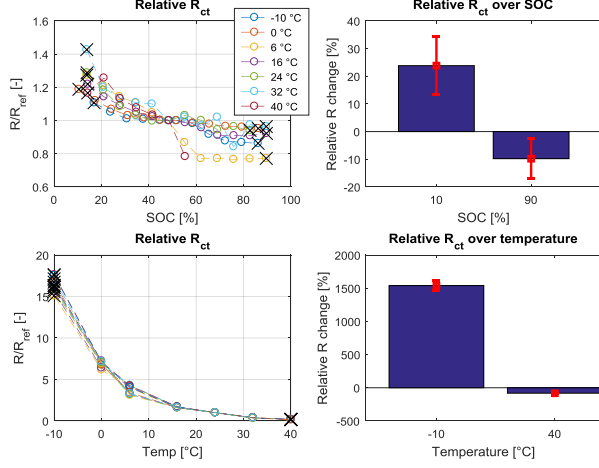
(b) Cell C at 49.4 ± 3.02 % SOC

Figure 3: Resistance measurements for point of interest a,d and f. Charge transfer can also be found in this diagram as $r_d - r_a$.

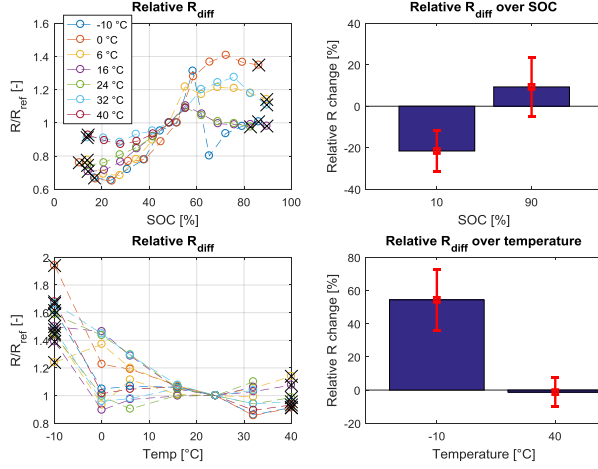
The diffusion phenomena forms as the mobility of ions in the electrochemical cell is limited. The longer a charge or discharge pulse is applied (i.e. lower fundamental excitation frequency), the further the movement needed for the average ion to form the necessary reactions. Example results are shown in Figure 3 on page 18 for cell B and C, which have quite different absolute magnitudes of resistance despite being similar rated in charge capacity and power. It can be seen that the magnitude of diffusion resistance is in the same range as the minimum resistance measured at point *a*. The temperature has very small influence on the resistive part of the diffusion impedance, although in closer analysis the temperature dependence is clearly according to an Arrhenius behavior with a negative temperature correlation.

4.4. Relative resistance change

In order to analyze and quantify how much temperature and SOC is contributing to the change of resistance, a relative increase scenario is set up. The operating point of 24°C and 50 % SOC is selected as the reference and from here the relative change of resistance is calculated for all composite resistances; r_{cc} , r_{elec} , r_{ct} and r_{diff} . All measurement values outside the SOC window 10-90 % are disregarded as they are not very relevant operating points for normal automotive usage and it is known that resistance and reactance increases drastically at these extreme points. Four specific operating points are selected to analyze the impact of temperature and SOC: 10 %, 90 %, -10°C and +40°C. For each operating points, the arithmetic mean and the standard deviation from (1) is calculated with all available measurement points in order to differentiate measurement noise from variable relation. An example of the process is shown in Figure 4 on page 20. In this example, it also be seen that the SOC has an impact as the resistance monotonically decreases with increasing SOC for r_{ct} (Figure 4a). It can also be seen that temperature has the largest impact on resistance change for r_{ct} , irregardless of SOC level. For diffusion resistance, r_{diff} as seen in Figure 4b on page 20, resistance increase for low temperatures is unambiguous. Diffusion resistance versus SOC, however, has only a weak trend flawed with random measurement noise. The process of isolating operating points in this manner is repeated for all cells and all composite resistances and displayed in Figure 6 on page 23. Bars represents the mean value (μ) and error bars indicate one standard deviation ($\pm\sigma$) as defined in (1).



(a) Cell B: r_{ct}



(b) Cell B: r_{diff}

Figure 4: Statistical analysis relative change for r_{ct} and r_{diff} . 24°C and 50 % is the reference operating points. The measurement points closest to 10 %, 90 %, -10°C and +40°C are selected (cross marked) to be included in the mean and standard deviation calculations.

4.5. Analysis Results

Plotting the absolute resistance for the different regions, as showed in Figure 2 on page 16, per cell and temperature gives an overview that clearly shows how the charge transfer resistance is negligible at the higher temperatures, see Figure 5 on page 22. However, at 0°C and below, the charge transfer resistance is dominant. Figure 6 on page 23 shows that for some of the trends, there is no simple relation between resistance, SOC and temperature, or the measurement noise is larger than the trend, indicated by very large error bars. Trends for cell A (not displayed here) are aligned with cell B (Figure 6a on page 23).

Current collector resistance (r_{cc}), represented by the metallic temperature coefficient in the non-chemically active parts of the electrodes, has the smallest impact over the measured temperature span for all cells. Since it is ideally modeled, there is no error bars included in the displayed data.

Minimum-resistance point r_a has a small, but vaguely significant impact from SOC. However, a significant impact from temperature, increasing typically 20-50 % at -10°C compared to the reference at 24°C.

Charge transfer resistance, r_{ct} , shows large and significant change of both SOC and temperature. r_{ct} is decreasing with increasing SOC for all cells. The largest impact is from temperature, where r_{ct} increases with 1500-3300 % from 24°C to -10°C. At higher temperatures, the resistance typically decreases to a degree where it virtually disappears in comparison to the other resistances.

Diffusion resistance, r_{diff} has no statistically significant correlation with SOC when looking over all the battery types. There is a clear resistance

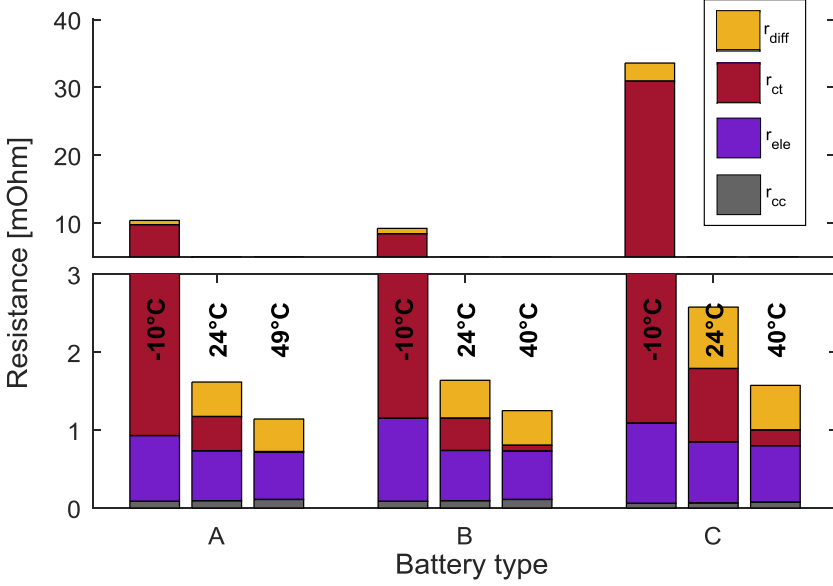
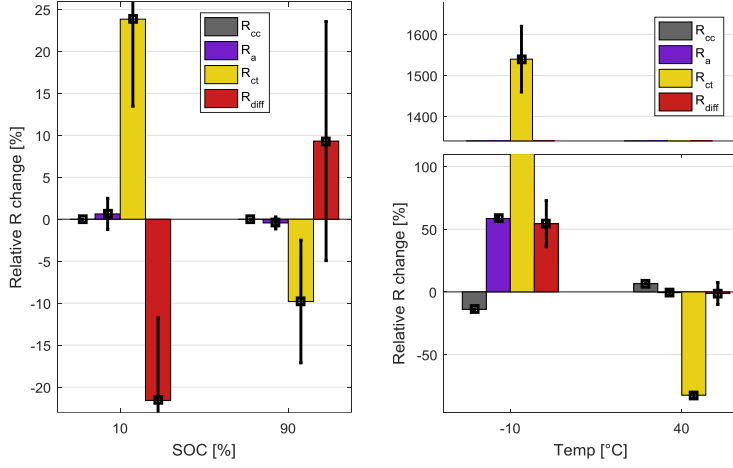


Figure 5: Distribution of absolute resistance between the defined circuit elements at 50 % SOC, for all three cells. The y axis is broken to capture the large difference between r_{ct} and the other elements at low temperatures. Cell A has an extended temperature range of 49°C compared to the other cells.

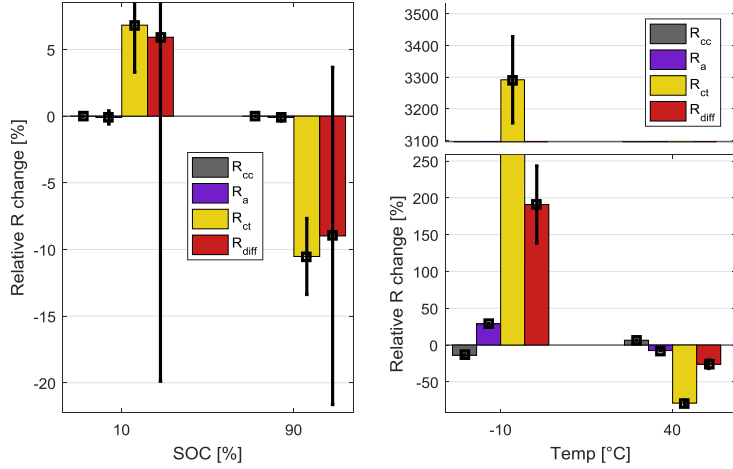
decrease with increasing temperature. r_{diff} can be 20-200 % higher at -10°C than at reference room temperature.

5. Model fitting

As described in Section 2, the two approaches to linear model fitting of the frequency domain impedance data is to use $R+2RC$ and $R+6RC$ based models. The ECMs are fitted to the measured data in the frequency domain using numerical optimization in MATLAB. For each spectrum, a nonlinear curve-fitting optimization based on the method of least-squares was used.



(a) Cell B



(b) Cell C

Figure 6: Analysis results of relative resistance change with 24°C and 50 % SOC as reference point for each cell individually. Legend order from left to right in each bar group: R_{cc} , R_a , R_{ct} , R_{diff} . Error bars show ± 1 standard deviation.

The estimated parameters are then implemented into the corresponding cell model, verified in the frequency domain and finally validated through a time-domain drive cycle test. Figure 7 on page 25 shows a few examples of the accuracy of impedance replication of the models to the original measurement data. The RMSE of the impedance is used to quantify the accuracy of the model in the frequency domain. The $R + 6RC$ based model results in a RMSE of $610 \mu\Omega$ over the SOC and temperature range covered in the tests. For the $R + 2RC$ or DP model, upper frequency range is limited to 2 Hz considering the intended usage in vehicle applications. This type of confined model, wherein the effort was made only to characterise the low frequency aspects of the cell behaviour results in RMSE of $970 \mu\Omega$. It is evident that the $R + 2RC$ model performance much worse when trying to reproduce the spectra. The RMSE based verification in the frequency domain still showed that the parametrised ECMs could be further used for validation with automotive drive cycles in the time domain. The RMSE values can be compared with measured r_e (100 mHz resistance) at 24°C and 50 % SOC for cell B and cell C respectively: $1.26 m\Omega$ and $1.96 m\Omega$.

6. Model validation in time domain

Since there is a lack of established dynamic load cycles to be performed on automotive cells on cell level, a combination of load cycles for performance test defined in [24] are used. Physical tests are performed with cell B and cell C at 8°C and 24°C in a climate chamber with forced air ventilation. An additional large thermal mass in the form of a aluminum cell holder firmly attached to the cell body in order to keep the temperature variations to

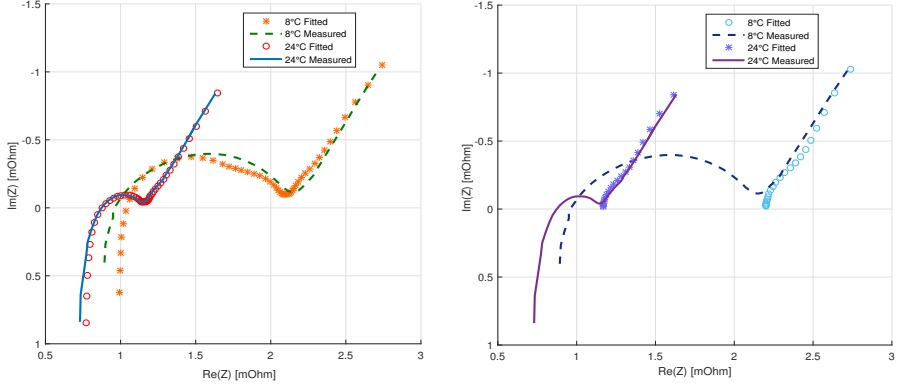


Figure 7: Model fitting with measurement data in the frequency domain using the $R+6RC$ model (left) and $R+2RC$ model (right). Data used is with reference to cell B at 50 % SOC at two different temperatures

a low level. The cells starts at 90 % SOC and are loaded with dynamic power profile, *charge depletion* from the profile *PHEV min* until a SOC of about 20 % is reached. At this point, the battery tester switches to a *charge sustaining* profile. The power level of the load cycles is scaled to the maximum power the cells can handle during all operating points in the test, according to the cell supplier, see Table 2 on page 26. The total load cycle is just short of 100 minutes long. The cell test equipment records voltage, current and temperature. The recorded current is fed into a Matlab Simulink model corresponding to the three ECMs studied. In addition to the two explained in Section 5, a rudimentary Thevenin model is also included in the comparison, where the R_{10} value is extracted from point *e* (Figure 2 on page 16 and Section 4.1) as a function of SOC for the relevant temperature. An example of the load cycle results is shown in Figure 8 on page 27. The final results in terms of maximum instantaneous voltage error estimation

between model and measurements, as well as the final RMSE according to (2) is summarized in Table 2 on page 26, where the resulting errors can be compared with similar studies.

Table 2: Setup and results from validation load cycle from this study (upper part) and comparable RMS voltage errors from similar studies (lower part).

Test object	Temp [$^{\circ}C$]	Power [W]	ECM	$max(E)$ [mV]	RMSE [mV]
B	24	630	R_{10}	160.3	33.38
			$R + 2RC$	89.15	15.46
			$R + 6RC$	108.2	18.77
C	24	500	R_{10}	192.9	33.93
			$R + 2RC$	139.3	20.31
			$R + 6RC$	158.1	24.58
Source	Method	ECM		$max(E)$ [mV]	RMSE [mV]
[10]	Self-calibrating	Non-linear R+2RC		-	63
[25]	Pulse	Linear R+2RC		-	26
[26]	Pulse	Linear R+2RC		259	10.65
[27]	Pulse	Linear R+2RC		218	45.8

7. Conclusions

7.1. Temperature trends

The largest resistance during operation of the tested cells between 10-90 % SOC and $-10^{\circ}C$ to $+40^{\circ}C$ is due to charge transfer resistance, r_{ct} . As shown in Figure 5 on page 22, it can vary from being virtually zero at

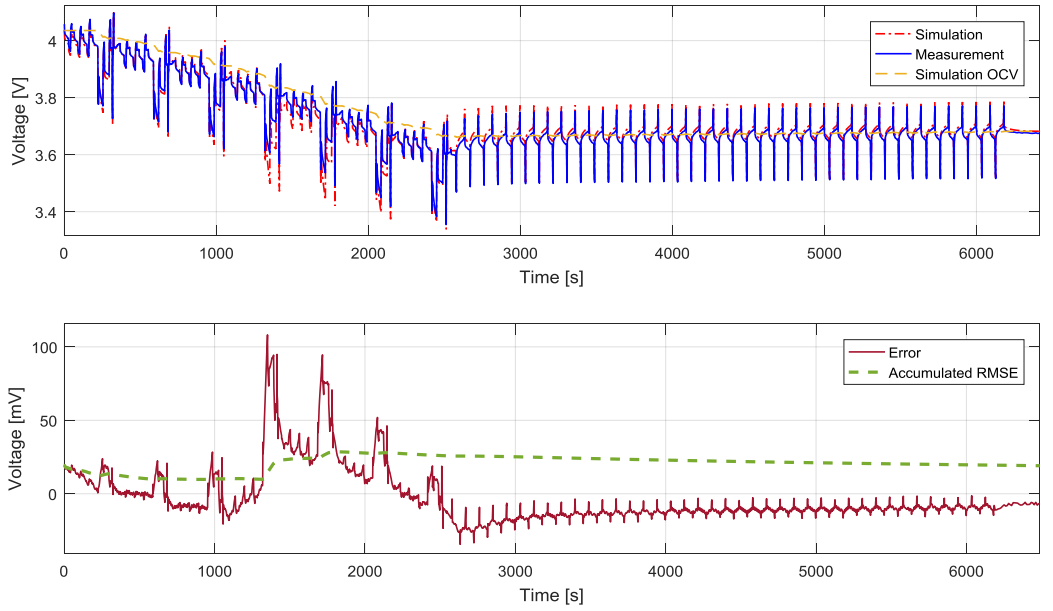


Figure 8: Load cycle measurements versus $R+6RC$ model for cell B at 24°C. Final RMSE is 24.58 mV, see Table 2 on page 26

+49°C, to 90 % of the total resistance at -10°C, using cell A as an example. This general behavior is common for all tested cells and well-known in the literature. For low temperature performance, cell C displays an increase of 3 time, whereas cell A only displays 2 times higher r_{ct} at -10°C with room temperature as reference. Figure 3a on page 18 shows the strong Arrhenius-like increase of r_{ct} with falling temperature. Both electrolyte resistance r_{ele} and diffusion resistance r_{diff} display similar Arrhenius trends, just not as strong. According to our observations, the absolute value of the minimum-resistance point r_a is increasing significantly with decreasing temperature, despite being partly canceled by the current collector’s positive temperature coefficient. This might be in contrary to reported assumptions[10] about the minimum-resistance point.

7.2. SOC trends

Studying the change of resistance over SOC, the only statistically significant trend that can be generalized over all cell types tested is a reduction of r_{ct} with increasing SOC. Other patterns are either too noisy (not statistically significant) to draw a conclusion, or the trends show opposite slopes between cell types due to chemical composition.

7.3. ECM design guidelines

When designing electrical equivalent circuits for general automotive lithium-ion applications, our recommendation is to prioritizing the efforts of parametrisation is:

1. $r_{ct}(T)$: The charge transfer resistance is dramatically increasing with a decrease of temperature, here measured at 1500-3300 %.
2. $r_{diff}(T)$: Diffusion resistance is strongly increasing with a decrease of temperature; 20-200 % compared to room temperature in our cases.
3. $r_a(T)$: The minimum resistance at high frequency increases 25-60 % at low temperatures, room temperature reference.
4. $r_{ct}(SOC)$: Charge transfer changes in a linear fashion from 7-37 % at low SOC to between -6 to -11 % at high SOC compared to mid-SOC.

No other trends with statistical significance is identified through our analysis that is common for all tested cells. For the purpose of designing low-frequency ECMs, the properties described by r_a and r_{ct} can favorably be lumped together in one circuit element as long as the SOC and temperature dependence is included.

Using EIS to extract ECM parameters to represent diffusion behavior of the cell with a $R + 2RC$ model is the most successful among the studied. For the purpose of achieving low RMSE voltage error in automotive load cycles, it makes more sense to focus model time constants towards the diffusion part of the equivalent circuit. This is confirmed by the validation cycles in Section 6 by a reduction of both peak error and RMSE by 40-80 % compared to a rudimentary R_{10} model. These findings math similar setups using pulse excitation for parameter extraction[26]. Similar results are also found in [10, 25], but using more complex methods or models. Yet, the model accuracy presented in this paper performs generally better in terms of average voltage estimation accuracy than similar results found in literature, see Table 2 on

page 26.

A somewhat surprising finding is that an increase of the model complexity by using a $R+6RC$ model to capture both charge transfer and diffusion very accurately in the frequency domain (Figure 7 on page 25), did not result in better time-domain model accuracy (Table 2 on page 26).

7.4. Drive cycle validation

Large proportions of the literature within BMS algorithms is focused on estimating open-circuit voltage or charge transfer impedance, which is indeed relevant for modeling in short time frames or as a tool to estimate temperature or age of the cells[16, 4]. Since typical usage of large automotive LIBs involves dynamical loads for 20-60 minutes, where it is more beneficial for estimation accuracy to include diffusion dynamics for the kind of open-loop models used in this work.

The impedance measurements presented here are gathered from direct measurements on mass-produced state-of-the-art automotive cells. The results can be directly transferred to industry applications to enhance initial model based design approaches and BMS algorithm design for electric or hybrid electric powertrains.

Acknowledgment

This work is sponsored by the Swedish Governmental Agency for Innovation Systems (VINNOVA) in cooperation with Volvo Car Corporation. Additional thanks to CEVT and Volvo Group ATR for their support with test material.

References

- [1] A. Lasia, Electrochemical impedance spectroscopy and its applications, in: Modern aspects of electrochemistry, Springer, 2002, pp. 143–248.
- [2] A. Jossen, Fundamentals of battery dynamics, Journal of Power Sources 154 (2) (2006) 530–538.
- [3] D. Andre, M. Meiler, K. Steiner, C. Wimmer, T. Soczka-Guth, D. Sauer, Characterization of high-power lithium-ion batteries by electrochemical impedance spectroscopy. i. experimental investigation, Journal of Power Sources 196 (12) (2011) 5334–5341.
- [4] S. Buller, Impedance based simulation models for energy storage devices in advanced automotive power systems, Ph.D. thesis, RWTH Aachen University (2002).
- [5] P. Mauracher, E. Karden, Dynamic modelling of lead/acid batteries using impedance spectroscopy for parameter identification, Journal of Power Sources 67 (1-2) (1997) 69–84.
- [6] H.-s. Song, T.-H. Kim, J.-B. Jeong, D.-H. Shin, B.-H. Lee, B.-H. Kim, H. Heo, Modeling of the lithium battery cell for plug-in hybrid electric vehicle using electrochemical impedance spectroscopy, in: Proceedings of the FISITA 2012 World Automotive Congress, Springer, 2013, pp. 563–571.
- [7] D. Andre, M. Meiler, K. Steiner, H. Walz, T. Soczka-Guth, D. Sauer, Characterization of high-power lithium-ion batteries by electrochemi-

- cal impedance spectroscopy. ii: Modelling, *Journal of Power Sources* 196 (12) (2011) 5349–5356.
- [8] T. Osaka, T. Momma, D. Mukoyama, H. Nara, Proposal of novel equivalent circuit for electrochemical impedance analysis of commercially available lithium ion battery, *Journal of Power Sources* 205 (2012) 483–486.
- [9] C. Fleischer, W. Waag, H.-M. Heyn, D. U. Sauer, On-line adaptive battery impedance parameter and state estimation considering physical principles in reduced order equivalent circuit battery models: Part 1. requirements, critical review of methods and modeling, *Journal of Power Sources* 260 (2014) 276–291.
- [10] C. Fleischer, W. Waag, H.-M. Heyn, D. U. Sauer, On-line adaptive battery impedance parameter and state estimation considering physical principles in reduced order equivalent circuit battery models part 2. parameter and state estimation, *Journal of Power Sources* 262 (2014) 457–482.
- [11] T. R. Jow, M. B. Marx, J. L. Allen, Distinguishing Li^+ charge transfer kinetics at nca/electrolyte and graphite/electrolyte interfaces, and nca/electrolyte and lfp/electrolyte interfaces in li-ion cells, *Journal of The Electrochemical Society* 159 (5) (2012) A604–A612.
- [12] T. Momma, M. Matsunaga, D. Mukoyama, T. Osaka, Ac impedance analysis of lithium ion battery under temperature control, *Journal of Power Sources* 216 (2012) 304–307.

- [13] Y. Ji, Y. Zhang, C.-Y. Wang, Li-ion cell operation at low temperatures, *Journal of The Electrochemical Society* 160 (4) (2013) A636–A649.
- [14] W. Waag, S. Käbitz, D. U. Sauer, Experimental investigation of the lithium-ion battery impedance characteristic at various conditions and aging states and its influence on the application, *Applied Energy* 102 (2013) 885–897.
- [15] Y. Olofsson, J. Groot, T. Katrašnik, G. Tavčar, Impedance spectroscopy characterisation of automotive nmc/graphite li-ion cells aged with realistic phev load profile, in: *Electric Vehicle Conference (IEVC), 2014 IEEE International*, IEEE, 2014, pp. 1–6.
- [16] J. Groot, State-of-health estimation of li-ion batteries: Cycle life test methods, Ph.D. thesis, Chalmers University of Technology (2012).
- [17] Y. Zhang, C.-Y. Wang, Cycle-life characterization of automotive lithium-ion batteries with linio2 cathode, *Journal of the Electrochemical Society* 156 (7) (2009) A527–A535.
- [18] P. Svens, Methods for testing and analyzing lithium-ion battery cells intended for heavy-duty hybrid electric vehicles, Ph.D. thesis, KTH Royal Institute of Technology (2014).
- [19] A. Eddahech, O. Briat, J.-M. Vinassa, Performance comparison of four lithium-ion battery technologies under calendar aging, *Energy* 84 (2015) 542–550.

- [20] M. Keddam, C. Rakotomavo, H. Takenouti, Impedance of a porous electrode with an axial gradient of concentration, *Journal of applied electrochemistry* 14 (4) (1984) 437–448.
- [21] O. Bohlen, Impedance-based battery monitoring, Ph.D. thesis, RWTH Aachen University (2008).
- [22] P. Taheri, A. Mansouri, B. Schweitzer, M. Yazdanpour, M. Bahrami, Electrical constriction resistance in current collectors of large-scale lithium-ion batteries, *Journal of The Electrochemical Society* 160 (10) (2013) A1731–A1740.
- [23] P. A. Nelson, K. Bloom, D. I Dees, Modeling the performance and cost of lithium-ion batteries for electric-drive vehicles., Tech. rep., Argonne National Laboratory (ANL), Argonne, IL (United States) (2011).
- [24] J. R. Belt, Battery test manual for plug-in hybrid electric vehicles, Tech. rep., Idaho National Laboratory (INL) (2010).
- [25] Y. Hu, S. Yurkovich, Y. Guezennec, B. Yurkovich, Electro-thermal battery model identification for automotive applications, *Journal of Power Sources* 196 (1) (2011) 449–457.
- [26] S. Skoog, Parameterization of equivalent circuit models for high power lithium-ion batteries in hev applications, in: *Power Electronics and Applications (EPE'16 ECCE Europe)*, 2016 18th European Conference on, IEEE, 2016, pp. 1–10.

- [27] H. He, R. Xiong, J. Fan, Evaluation of lithium-ion battery equivalent circuit models for state of charge estimation by an experimental approach, *Energies* 4 (4) (2011) 582–598.

Paper V

Pole-Slot Selection Considerations for Double Layer Three-phase Tooth-Coil Wound Electrical Machines

Presented 2018-09-03 at
ICEM2018, Alexandroupoli, Greece

Published 2018-10-25 in IEEE Xplore:
<http://ieeexplore.ieee.org/document/8506772>

First author contributions

Idea generation, literature review, theoretical evaluation,
data processing and analysis, FEA figures, corresponding author.

Second author contributions

Idea development, model verification.

Pole-Slot Selection Considerations for Double Layer Three-phase Tooth-Coil Wound Electrical Machines

Stefan Skoog, *Member, IEEE* and Alessandro Acquaviva, *Member, IEEE*

Abstract—This work presents a combination of top-down and bottom-up design procedures to select a suitable pole-slot combination for a tooth-coil wound machine (TCWM), also known as non-overlapped fractional slot concentrated winding synchronous machine. Top-down features such as size and speed are determined by the intended application and affect the selection of slot and pole number. Bottom-up properties are quantified through key performance indicators (KPI) such as fundamental winding factor, periodicity, cogging multiplier and MMF harmonic leakage factor (HLF). Furthermore a compact and intuitive graphical way of presenting the properties of the double layer TCWMs is shown in this paper for slot number up to 39, highlighting the similarities among machines through the key winding factor concept. Analytical formulas for KPIs are presented and the results are compared and visualized with FEM simulations.

Index Terms—Electric machines, AC machines, Brushless machines, Rotating machines, Permanent magnet motors, Electromagnetic modeling, Magnetic flux

I. INTRODUCTION

A. Tooth-coil wound machines

Tooth-coil wound machines (TCWM) [1], [2], also known as non-overlapped fractional slot concentrated winding (FSCW) synchronous machines, offer several benefits compared to machines with a distributed winding [3], but they also present some special characteristics resulting in design challenges not typical for classical distributed winding machines.

One of the main challenges with TCWMs is that the stator induced MMF wave contains both sub- and super-harmonics spatially along the air gap. Space harmonics affect the machine inductance and can induce significant losses in the rotor iron and in the rotor permanent magnets (PMs). This kind of rotor losses is studied in detail in [4], [5].

Among the benefits of using a TCWM, is generally higher torque density, which is a direct effect of achieving higher stator slot fill factor, and minimization of end windings length and hence lower losses and lower parasitic effects. The lack of end windings becomes a significant advantage in radially magnetized, axially short machines, which is the

machine topology studied in this paper. A non-overlapping stator winding, as offered by TCWM, allows for pre-winding of stator coils before installing them on the machine [6]. TCWMs are well suited for stator segmentation, and winding coils directly on stator segments can offer fill factors of 60–78% [3]. Combining TCWM with soft magnetic composites and pre-pressed windings, fill factors beyond 80% can be reached [3], [7].

Performance indicators for high-performance TCWM are presented in [6], [8]–[11]. The inductance in TCWMs due to harmonics is studied in [12] and [1]. In [13], a comprehensive set of analytical equations are presented to analyze TCWMs, independent of number of layers and number of phases, in terms of finding the optimal rotor pole number for a given stator slot number by acquiring the winding factors for all reasonable harmonics. An overview with some examples of key winding factors, periodicity and torque ripple is given in [14], [15].

This paper combines the most relevant performance indicators from the literature together with the basic analysis and presents it graphically together with a FEM verification for a vast number of machine designs. The concept of *coil grouping*, *base machine* and *key winding factor* is highlighted in order to group machines together in families with identical key performance indicators (KPIs).

TCWMs are mainly used for Brushless DC (BLDC) and Brushless AC (BLAC) applications, where one characteristic difference between the two is the effective shape of the back electromotive force (BEMF) due to the magnetic-geometric design. BLDC typically offer high flux linkage, but a BEMF with significant harmonic content, approaching trapezoidal shape. BLAC designs typically offer very pure sinusoidal BEMF, which is possible by harmonic elimination when matching stator tooth tip and rotor pole geometries.

B. Pole-slot selection

The aim of this paper is to guide the electrical machine designer in the selection of a suitable pole/slot combination for a specific application. The process is divided into two main steps:

- From application specifications, such as torque rating and speed, determine the acceptable range of pole pairs and slots. This is the top-down process.
- Verify which is the most suitable pole slot combination based on KPIs, grouping design families together and

This work is sponsored by the Swedish Governmental Agency for Innovation Systems (VINNOVA) and The Swedish Energy Agency
S. Skoog and A. Acquaviva are both with Chalmers University of Technology, Gothenburg, Sweden (e-mail: stefan.skoog@chalmers.se and alessandro.acquaviva@chalmers.se).

visualizing them in an intuitive manner. This is the bottom up process.

II. THEORY

A. Pole-slot structures

A simple method of determining whether a machine with a certain pole - slot combination qualifies as an TCWMs for a machine with n_{ph} phases is to look at the slot per pole per phase number

$$q = \frac{Q_s}{2p n_{ph}}. \quad (1)$$

where Q_s is the number of slots and p is the number of pole pairs. If $q \geq 1$, the machine is a traditional distributed winding type, e.g. $q = [1, \frac{3}{2}, 2]$ are common setups for overlapping distributed winding machines. Most 3-phase TCWMs offering high performance fulfill $\frac{1}{4} \leq q \leq \frac{1}{2}$, a comprehensive explanation of this is given throughout the paper. The TCWMs defining this boundary, $q = [\frac{1}{2}, \frac{1}{4}]$, are often referred to as traditional brushless PM machines, which have single-tooth per phase windings $W = 1$ (defined in (3)) and with the highest possible periodicity (t_{sym}) for any given number of slots. Machines with $q = \frac{1}{2}$ are the only TCWM where the working harmonic is also the lowest harmonic, i.e. all other combinations of Q_s and p will generate MMF subharmonics, which will limit their electromagnetic performance.

B. Base machine, periodicity and key winding factor

Although there is a very large set of possible combinations of slot and poles, only a small fraction of these combinations can produce a viable machine. The winding structure for many TCWMs are often repeated within a mechanical revolution, creating symmetry with the smallest symmetrical part referred to as *phase belt* [13] or as *base machine* [12]. This is the smallest pole-slot structure that defines the basic properties of the machine. Most parts of the machine analysis can preferably be performed on the base machine instead of the full machine, including FEM analysis when using the right boundary conditions.

The machine electrical *periodicity*, or *mode order* [16], defines how many symmetric parts the machine can be split into from an electromagnetic perspective. The periodicity also states the maximum number of parallel connections of coils possible. Machines can be both symmetric and anti-symmetric, where the latter example means that each second phase belt is repeated with the coils phase shifted 180 degrees, e.g. with coils electrically reversed. The greatest common divisor (GCD) between pole pair number p and slot number Q_s is used to establish how many phase belts that are possible in a balanced machine setup, i.e. the periodicity for complete symmetry t_{sym} or anti-symmetry t_{asym} is defined as

$$t_{sym} = GCD(p, Q_s) \quad (2a)$$

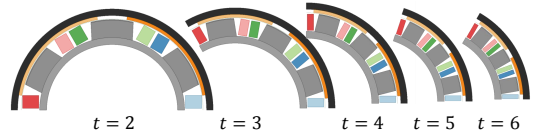
$$t_{asym} = GCD(2p, Q_s). \quad (2b)$$

How the periodicity affects the winding structure is illustrated in Figure 1a. Note that the value of t shown in the picture can be either t_{sym} or t_{asym} depending on the winding configuration. Any viable TCWM need a t number above unity in order to cancel radial forces induced in the rotor, creating excessive noise and vibrations [14], [17].

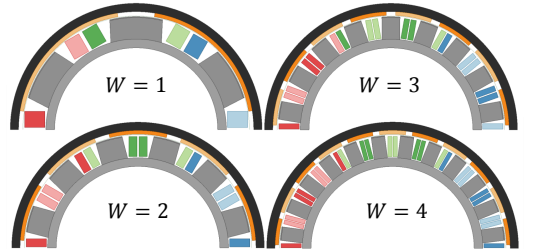
The high-level key performance indicator *key winding factor* [10], [16] W , defined as

$$W = \frac{Q_s}{n_{ph} t_{asym}} = \frac{Q_s}{n_{ph} GCD(2p, Q_s)}, \quad (3)$$

fulfills two functions. W must be a positive integer to realize a balanced machine with n_{ph} number of phases, W also defines the number of coils from the same phase in each phase belt. In most high-performance machines (see Table I) with $Q_s < 30$, all coils from the same phase within a phase belt are positioned on adjacent stator teeth, as illustrated in Figure 1b. Typically for high-power-density (high speed, low pole number) and production-friendly TCWMs, the key winding factor is low.



(a) Machine layouts with unity key winding factor and varying periodicity.



(b) Machine layouts with periodicity $t_{sym}=2$ and varying key winding factor.

Fig. 1: Winding layouts for an outer-rotor TCWM. The phase windings are represented by colored rectangles in blue, red, green for phase A,B,C respectively. The geometry corresponding one electrical period is drawn for each variant, i.e. the *base machine*.

C. Cogging torque

Specifically for TCWM, a way of reducing the magnitude of cogging torque is to design for high cogging frequency, so that the produced cogging torque is damped by the rotor inertia. The cogging frequency multiplication M_f depends

on the least common multiplier (LCM) between number of slots and number of poles [10], [16], [18]:

$$M_f = \text{LCM}(2p, Q_s). \quad (4)$$

D. Winding layout

Methods to derive the optimal winding layout for a given pole, slot and layer number is widely covered in literature. The main methods are the star of slots method [8], [9] or the method presented in [10], [19], [20]. The latter is used in this work and some examples are presented in Figure 1 and Figure 2.

E. Winding factor

The winding factor k_w decides the linkage between the coil current and any specific spatial MMF harmonic in the airgap. Once the stator winding is designed, the rotor pole number locks to the matching spatial MMF harmonic which is defined as the *working harmonic* or the *fundamental harmonic* $k_{w,f}$. To make detailed estimations of stator MMF and total stator inductance, the winding factor have to be calculated for all harmonics. Methods for this are reported in [8], [9], [13] and are all similar in their structure. Generally, the winding factor k_w consist of the product of winding distribution factor k_d and winding pitch factor k_p , which must both be evaluated for each spatial harmonic number. The skewing [18] factor is ignored in this scope.

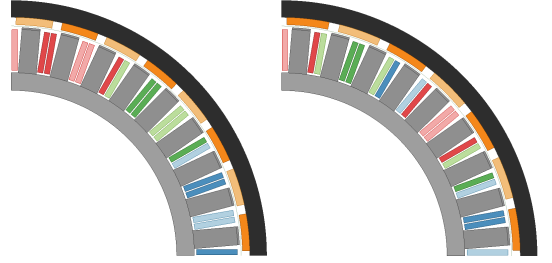
$$k_w = k_d k_p \quad (5)$$

F. Grouped coils within phase belt

Most TCWM combinations of Q_s and p that offer high performance will automatically group together coils from the same phase so that they are placed next to each other within any symmetric or anti-symmetric phase belt that forms the base machine, Figure 1b and Figure 2a shows examples of this. However, there is also examples of machines where coils from the same phase are spread out over the phase belt in a seemingly random manner, but still providing high winding factor and reasonable losses as in Figure 2b. A condition presented in [21] is ameliorated into a simpler form by directly recognizing asymmetry as defined in (2) and included in (3):

$$\text{round}\left(\frac{Q_s}{2p}\right) W = \text{round}\left(\frac{Q_s}{2p} W\right). \quad (6)$$

This condition holds true only when the machine can form a winding where all coils from a phase are placed on adjacent stator teeth within the smallest symmetric or asymmetric phase belt.



(a) Q36p16, $k_w = 0.945$

(b) Q36p14, $k_w = 0.902$

Fig. 2: Two TCWMs with $W=3$, with phase coils (a) grouped, and (b) non-grouped.

G. Stator generated MMF

With the assumption that the machine is fed by a symmetric multiphase current, that stator slots can be represented as point like sources and the magnetic materials are acting linearly, several methods can be used to estimate the stator induced airgap MMF [21]–[23], which are all similar by utilizing spatial Fourier series while keeping the time frozen for the multiphase phase input. By using the same assumptions, a simplified numerical approach to draw the MMF waveform can be used. Once the layout of the winding is defined, starting from any of the slots, the number of ampere-turns that are met around the mechanical angle are added up for each slot (summing up the ampere turns within the slot) and then the average value is subtracted. With some further care the effect of the slot opening on the stator generated MMF can be added.

H. Magnetization inductance

The total stator coil inductance L_s can be split into airgap inductance L_δ and stator leakage inductance L_σ . The airgap inductance represents all linked stator flux that travels over the airgap, whereas L_σ are all parasitic inductance generated from slot, tooth tip and end winding lumped together. The airgap inductance can, specifically for TCWMs be divided into synchronous magnetizing inductance through the fundamental harmonic L_{ms} which is involved in the net torque production, and a parasitic magnetization of harmonics L_h which does little for net torque production [2]. Since the magnetic circuit for fundamental and harmonics are equal, it is feasible to express the harmonic inductance as proportional to the fundamental air gap inductance, introducing the harmonic air gap leakage factor δ_σ .

$$L_s = L_\delta + L_\sigma \quad (7a)$$

$$L_\delta = L_{ms} + L_h = L_{ms} (1 + \delta_\sigma) \quad (7b)$$

The harmonic air gap leakage factor can be calculated by summing together the relative amplitude of all harmonics h , either by using winding factors [2], [24] or the harmonic

spectrum [12] derived from distribution- and pitch factors or by applying Fourier analysis on the winding function:

$$\delta_\sigma = \sum_{v \neq v_f} \left(\frac{v_f}{v} \frac{k_{w,v}}{k_{w,f}} \right)^2 = \sum_{v \neq v_f} \left(\frac{h_v}{h_f} \right)^2, \quad (8)$$

where v is the harmonic number, v_f is the fundamental (working) harmonic of the base machine. With this said, the MMF harmonic spectrum will directly affect the performance of the TCWM by increasing its inductance without linking any torque producing flux. Increased inductance can be useful in some particular cases, such as limited short-circuit current or increased field weakening range. Generally, increased inductance is an undesired property due to increased reactive voltage drop of the machine at high speeds, decreased maximum torque and decreased power factor. The harmonic air gap leakage factor is a particularly interesting indicator of the spatial harmonic content. This scaling effect with the harmonic order well represents the effect of the airgap, which acts as a low pass filter, when evaluating the flux density harmonics generated by the stator MMF that in turn generate eddy current losses in the rotor iron and PMs. Hence, δ_σ can be used as an indicator of rotor losses. Note that the harmonic leakage factor is calculated with the assumption that the coil pitch equals to slot pitch, i.e. a virtual tooth tip design with infinitesimally small slot opening.

III. METHOD

The selection of slot and pole number begins with the knowledge of the intended application of the machine.

A. Pole-slot range from top-down requirements

Brushless machines are by definition inverter fed, this means there are no limitation tied to grid frequency or voltage. From a system perspective, the pole selection affects the frequency of the fundamental which directly affects iron losses and the switching frequency of the converter. High power density machines typically aim for high mechanical speed, which makes it suitable to select a low rotor pole number in order to keep the fundamental electrical frequency within a certain range. This because standard laminated materials result in reasonable losses with an excitation frequency of 0.1-1.0 kHz. Furthermore, to have an acceptable current ripple, the switching frequency should be at least 20 times the fundamental but it also directly affects switching losses. By setting the maximum fundamental frequency $f_{f,max}$ the maximum number of poles is established as

$$p_{max} = \frac{4\pi f_{f,max}}{\omega_m}, \quad (9)$$

where ω_m is the mechanical angular speed.

The machine size constraint also plays a role in the maximum number of poles that can be selected. A small sized machine with a high pole number equals small slots. This leads to challenges in the winding procedure, and together

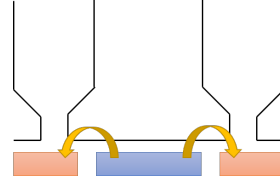


Fig. 3: PM flux shunting effect.

with reserving space for a slot liner and isolation between the two coils, the resulting gross fill factor will drop.

The opposite example with a large size machine and low pole number results in few but large slots. This should be avoided because the thermal design of the slot becomes critical, the end-windings are longer, and the overall design of the machine becomes more problematic. Generally, a good TCWM stator design presents slots that have a height and length that are within a ratio of 2.

B. KPIs and bottom-up design criteria

A step-by-step design procedure of how to establish a suitable slot-pole combination for a two-layer, three-phase TCWM is summarized in Table I, with the most basic and important design criteria in the top of the table, including references to the relevant formulas. Additionally, some guidelines about the conditions are given. Machines with very high number of poles compared to the slots ($q < 0.25$) might show good KPIs, however due to the flux shunting effect shown in Fig. 3, their performance is limited beyond what is reflected in the theory in this paper.

TABLE I: TCWM design procedure

Attribute	Characteristic	Condition
Fractional slot pitch	Slot/pole/phase (1)	$q \leq 1$
Phase symmetry possible	Symmetric windings (3)	$W \in \mathbb{Z}^+$
Avoid radial EM forces	Periodicity (2)	$t \geq 2$
High torque per ampere	Fund. winding factor (5)	$k_{w,f} > 0.85$
Low parasitic inductance	Harmonic leakage (7b)	Low δ_σ
Low rotor losses	Low space harmonics (7b)	Low δ_σ
Avoid PM shunting effect	Slot/pole/phase (1)	$q \geq 0.25$
Low cogging torque	Periodicity (4) (2)	High M_f & t
Low torque ripple	Large phase belts (3)	$W > 1$
Modular windings	Grouped phase coils (6)	Equality

\mathbb{Z}^+ = positive integer

IV. RESULTS

For bottom-up design, a table with formulas on how to form high-performance pole-slot combinations with grouped coils up to key winding factor seven is presented in Table II, together with their corresponding fundamental winding factor. Other TCWMs with satisfactory performance do exist outside the range of this table, but with non-grouped coils (see Figure 2b) or key winding factor above seven.

In Figure 5, a graphical representation of all slot-pole combinations up to Q39p17 rendered. Distributed windings

TABLE II: Base machine and their derivatives for dual-layer, three-phase TCWM.

W	Winding factor $k_{w,f}$	Possible slot number Q	Possible pole number $2p$	Base Machine $Q_s/2p$	Example q
1	0.8660	$3x$	$Q(1+2y) \pm x$	$3/2$ $3/4$	$1/2$ $1/4$
2	0.9330	$12x$	$Q(1+2y) \pm 2x$	$12/10$ $12/14$	$2/5$ $2/7$
3	0.9452	$9x$	$Q(1+2y) \pm x$	$9/8$ $9/10$	$3/4$ $3/8$
4	0.9495	$24x$	$Q(1+2y) \pm 2x$	$24/22$ $24/26$	$4/11$ $4/13$
5	0.9514	$15x$	$Q(1+2y) \pm x$	$15/14$ $15/16$	$5/14$ $5/16$
6	0.9525	$36x$	$Q \pm 2x$	$36/34$ $36/38$	$6/17$ $6/19$
7	0.9531	$21x$	$Q(1+2y) \pm 2x$	$21/20$ $21/22$	$7/20$ $7/22$

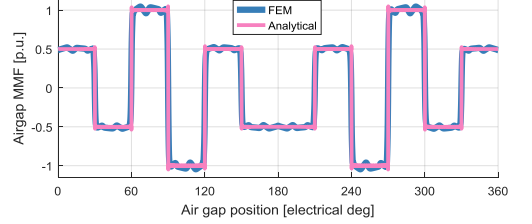
$x \in \mathbb{N}^+$ (all real non-zero numbers)
 $y \in \mathbb{N}_0$ (all real non-negative numbers)

of $q = [1, 2]$ are included as a reference. For each slot-pole combination, four of the KPIs are displayed: Fundamental winding factor $k_{w,f}$, harmonic leakage factor $\delta_\sigma(8)$, asymmetric periodicity $t_{assym}(2b)$ and cogging frequency multiplication $M_f(4)$. Red boxes indicate that conditions from Table I are not fulfilled. Yellow boxes signals passed conditions, and more green means excellent performance in each KPI. A dashed HLF number means that the machine coils are unevenly grouped according to (6), which renders the analytical procedures behind (8) inaccurate. Gray boxes are disqualified due to flux shunting and very high HLF numbers, which means that they will likely display inferior performance, but also that the analytical methods presented here are less accurate. Out of 208 possible design candidates marked by the grid in Figure 5, 49 designs pass rule one through four from Table I, most of them grouped coil designs belonging to any of the combinations possible from Table II.

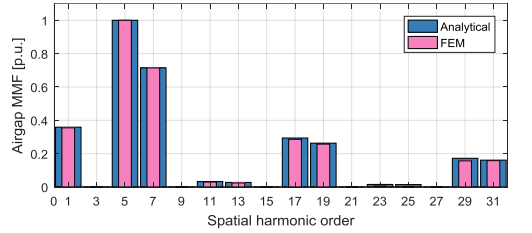
A. FEM verification of HLF

A Q36 outer-rotor is selected and modeled in Ansys Maxwell in order to verify HLF. The machine is normally equipped with surface-mount permanent magnet, however, for the study of stator induced magnetic field in the airgap, the magnets are not included. A slot number of 36 is selected since it offers many different machine variations with varying W numbers without changing the stator geometry apart from winding configuration. The machine is excited with a stator current below saturation level of the magnetic iron and the radial component of the magnetic flux density is evaluated along an arc in the middle of the air gap, as displayed in Figure 4a. The machines used for FEM analysis present a very small slot opening in order to match the analytical method to calculate HLF, assuming a coil pitch that equals the slot pitch. From Figure 4c one can see how the tooth tips saturate at nominal stator current which will result in a slot opening effect. It should be noted that HLF can differ substantially with wide slot openings and some care must be

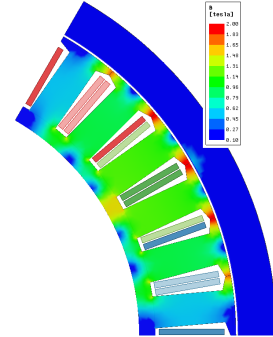
taken when evaluating the harmonic content based on this coefficient. The results of HLF between analytical and FEM method is presented in Table III, the time series and FFT of the spatial MMF wave can be seen in Figure 4. The results from the two methods match very good, verifying that the winding configuration alone, and the selection of fundamental harmonic influence the HLF to a large degree and that the analytical method gives a fair and accurate representation of the stator induced MMF. Note that the MMF waveform is derived from the flux density in the airgap.



(a) Spatial MMF waveform in airgap for one symmetric electrical period.



(b) FFT spectrum of spatial MMF waveform in airgap. Working harmonic is 5.



(c) Magnetic flux density plot when C winding (green) is carrying peak current with a balanced 3-phase supply.

Fig. 4: Analysis of MMF by analytical Fourier series and air gap spatial flux density from FEM for a Q36p15 machine.

TABLE III: Comparison of harmonic Leakage factor established by FEM versus analytical method.

Machine	W	Analytical	FEM	Diff
Q36p12	1	0.462	0.545	+18%
Q36p15	2	0.966	0.925	-4.3%
Q36p16	3	1.178	1.217	+3.3%
Q36p17	6	1.417	1.415	+0.1%

V. CONCLUSIONS

A procedure to select pole and slot combinations has been presented in this paper. Clear guidelines are provided to assist the machine designer in this selection depending on the application. The key performance indicators presented in Figure 5 match the results found in literature (for fundamental winding factor [12], [18], [20], harmonic leakage factor [2], periodicity [14] and cogging multiplier [15]).

The analytically calculated harmonic leakage factor has been compared with FEM simulations for several machines Q36 in Table III showing good agreement. The effect of slot opening on the MMF shape, and hence also HLF, due to selective space harmonic elimination, is not considered in this work but forms an interesting basis for further work.

REFERENCES

- [1] J. Pyrhonen, T. Jokinen, and V. Hrabovcova, *Design of rotating electrical machines*. John Wiley & Sons, 2009.
- [2] P. Ponomarev, Y. Alexandrova, I. Petrov, P. Lindh, E. Lomonova, and J. Pyrhonen, "Inductance calculation of tooth-coil permanent-magnet synchronous machines," *IEEE Trans. Ind. Electron.*, vol. 61, no. 11, pp. 5966–5973, 2014.
- [3] A. M. El-Refaie, "Fractional-slot concentrated-windings synchronous permanent magnet machines: Opportunities and challenges," *IEEE Trans. Ind. Electron.*, vol. 57, no. 1, pp. 107–121, 2010.
- [4] N. Bianchi, S. Bolognani, and E. Fomasiero, "A general approach to determine the rotor losses in three-phase fractional-slot pm machines," in *Electric Machines & Drives Conf.*, 2007. *IEMDC'07. IEEE Int.*, vol. 1. IEEE, 2007, pp. 634–641.
- [5] H. Zhang and O. Wallmark, "Limitations and constraints of eddy-current loss models for interior permanent-magnet motors with fractional-slot concentrated windings," *Energies*, vol. 10, no. 3, p. 379, 2017.
- [6] A. Masmoudi, J. Souldard, and F. Meier, "Design guidelines and models for pmsms with non-overlapping concentrated windings," *COMPEL: The int. journal for computation and mathematics in electrical and electronic engineering*, vol. 30, no. 1, pp. 72–83, 2011.
- [7] A. G. Jack, B. C. Mecrow, P. G. Dickinson, D. Stephenson, J. S. Burdett, N. Fawcett, and J. Evans, "Permanent-magnet machines with powdered iron cores and prepressed windings," *IEEE Transactions on Industry Applications*, vol. 36, no. 4, pp. 1077–1084, 2000.
- [8] N. Bianchi, M. Dai Pre, L. Alberti, and E. Fornasiero, "Theory and design of fractional-slot pm machines," in *Conf. Rec. IEEE IAS Annu. Meeting*, 2007, p. 196.
- [9] N. Bianchi and M. Dai Prè, "Use of the star of slots in designing fractional-slot single-layer synchronous motors," *IEE Proc. Electric Power Applications*, vol. 153, no. 3, pp. 459–466, 2006.
- [10] J. Cros and P. Viarouge, "Synthesis of high performance pm motors with concentrated windings," *IEEE transactions on energy conversion*, vol. 17, no. 2, pp. 248–253, 2002.
- [11] A. M. El-Refaie and T. M. Jahns, "Optimal flux weakening in surface pm machines using concentrated windings," in *Industry Applications Conf.*, 2004. *39th IAS Annual Meeting. Conf. Record of the 2004 IEEE*, vol. 2. IEEE, 2004, pp. 1038–1047.
- [12] P. Ponomarev, P. Lindh, and J. Pyrhönen, "Effect of slot-and-pole combination on the leakage inductance and the performance of tooth-coil permanent-magnet synchronous machines," *IEEE Trans. Ind. Electron.*, vol. 60, no. 10, pp. 4310–4317, 2013.

- [13] Y. Yokoi, T. Higuchi, and Y. Miyamoto, "General formulation of winding factor for fractional-slot concentrated winding design," *IEEE Electric Power Applications*, vol. 10, no. 4, pp. 231–239, 2016.
- [14] S. G. Min and B. Sarlioglu, "Investigation of electromagnetic noise on pole and slot number combinations with possible fractional-slot concentrated windings," in *Transportation Electrification Conf. and Expo (ITEC)*, 2017. *IEEE*, 2017, pp. 241–246.
- [15] H. Jussila, P. Salminen, M. Niemela, and J. Pyrhonen, "Guidelines for designing concentrated winding fractional slot permanent magnet machines," in *Power Engineering, Energy and Electrical Drives, 2007. POWERENG 2007. Int. Conf. on*. IEEE, 2007, pp. 191–194.
- [16] S. G. Min and B. Sarlioglu, "Investigation of electromagnetic noise on pole and slot number combinations with possible fractional-slot concentrated windings," in *Transportation Electrification Conf. and Expo (ITEC)*. IEEE, 2017, pp. 1–7.
- [17] B. Aslan, E. Semail, J. Korecki, and J. Legranger, "Slot/pole combinations choice for concentrated multiphase machines dedicated to mild-hybrid applications," in *IECON 2011-37th Annual Conf. on IEEE Industrial Electronics Society*. IEEE, 2011, pp. 3698–3703.
- [18] F. Magnussen and C. Sadarangani, "Winding factors and joule losses of permanent magnet machines with concentrated windings," in *Electric Machines and Drives Conf.*, 2003. *IEMDC'03. IEEE Int.*, vol. 1. IEEE, 2003, pp. 333–339.
- [19] F. Meier, "Permanent-magnet synchronous machines with non-overlapping concentrated windings for low-speed direct-drive applications," Ph.D. dissertation, KTH, 2008.
- [20] F. Libert and J. Souldard, "Investigation on pole-slot combinations for permanent-magnet machines with concentrated windings," in *Int. Conf. on Electrical Machines (ICEM 04)*, 2004, pp. 5–8.
- [21] H. Zhang, O. Wallmark, M. Leksell, S. Norrga, M. N. Harnefors, and L. Jin, "Machine design considerations for an mh/spb-converter based electric drive," in *Industrial Electronics Society, IECON 2014-40th Annual Conf. of the IEEE*. IEEE, 2014, pp. 3849–3854.
- [22] B. Zhao and G. Li, "The analysis of multiphase symmetrical motor winding mmf," *Electrical Engineering and Automation*, vol. 2, no. 2, 2013.
- [23] H. Zhang, "On electric machinery for integrated motor drives in automotive applications," Ph.D. dissertation, KTH Royal Institute of Technology, 2017.
- [24] G. Huth, "Permanent-magnet-excited ac servo motors in tooth-coil technology," *IEEE Transactions on Energy Conversion*, vol. 20, no. 2, pp. 300–307, 2005.

VI. BIOGRAPHIES

Stefan Skoog was born in 1985 and hold a M.S. degree from Lund University, Sweden in Industrial Electronics and Automatic Control. He has been working professionally with embedded systems, electronics and vehicle electrification for 10 years. Stefan is currently a PhD student at the Division of Electric Power Engineering, Chalmers University of Technology, Sweden. His research project is affiliated with Volvo Cars with the ambition to accelerate the electrification of passenger vehicle powertrains through the use of low voltage mild hybrid systems.

Alessandro Acquaviva received his M.S. degree at Politecnico di Torino in 2012 and is a PhD student at the Division of Electric Power Engineering, Chalmers University of Technology since 2016. From 2012 to 2016 he has been working in the traction electrification industry. His current research interests include electric drives, electrical machine design and multiphysics modeling of electrical machines.

Paper VI

Design and Verification of In-slot Oil-Cooled Tooth Coil Winding PM Machine for Traction Application

Submitted 2019-12-20 to IEEE Transactions on Industrial Electronics

Published 2020-04-07 in IEEE Xplore:

<https://ieeexplore.ieee.org/document/9059039>

First author contributions

Lead machine design FEA, thermal and mechanical,
data processing and analysis, FEA figures, CFD and CHT analysis,
figure generation.

Second author contributions

Lead in design, construction and calibration of measurement setup,
idea development, verification of machine design with FEA,
corresponding author.

Third author

Paper review, paper structure, idea revision, supervision,
administration, resource allocation, funding.

Design and Verification of In-slot Oil-Cooled Tooth Coil Winding PM Machine for Traction Application

Alessandro Acquaviva, *Student Member, IEEE*, Stefan Skoog, *Student Member, IEEE*, and Torbjörn Thiringer, *Senior Member, IEEE*

Abstract—Tooth coil windings, in particular when using a double layer structure, present opportunities for in-slot liquid cooling. Since the windings are not overlapping, access to the slot from the end section for coolant liquids is enabled. In this paper, a solution for in-slot and in-stator direct oil cooling for a tooth coil winding machine is presented. The coils are pre-wound on bobbins and inserted on the stator teeth. The novelty of the design consists in the integration of the cooling, using a thermally conductive epoxy resin to create the channels within the slot as well as the positioning of the stator yoke cooling channels. A 50 kW machine for an automotive traction application is designed, manufactured and tested. Conjugate heat transfer simulations are used in the design process in combination with finite element analysis for the loss mapping. The thermal model is verified with measurements at 6 l/min oil flow and 17.5 A/mm² continuous and 35 A/mm² 30 s peak. The thermal model is then used to establish a continuous operating point of 25 A/mm².

Index Terms—Cooling, Permanent magnet motors, Modeling

I. INTRODUCTION

The development of electric drivetrains is primarily dominated by the permanent magnet synchronous machine (PMSM) [1], characterized by their high efficiency, high power and high torque density [2]–[4]. Liquid cooling is necessary to enable high torque density for continuous operation. Extensive engineering efforts are devoted to develop automotive traction machine cooling solutions, as summarized well in [5]–[7].

Design of electrical machines is a multiphysics (electric-magnetic-thermal-mechanic) challenge. The thermal modeling is essential to establish the continuous and transient maximum performance. In classical machines, cooling jackets are used, which can be modelled with a simplified lumped-parameter approach [8], [9]. However, with increased complexity of the cooling solution, conjugate heat transfer (CHT) simulations are needed during the design process to evaluate the thermal performance. This is the case for the machine presented in

this article, where the stator end sections of the machine are immersed in the cooling fluid and designed to generate turbulence and distribute the fluid in the slot and iron cooling channels.

Tooth coil winding machines, also defined as non-overlapping fractional slot (pitch) concentrated winding (FSCW) machines, are particularly interesting when it comes to high power density, high efficiency and flexibility in manufacturing [10]–[12]. Furthermore, they present several opportunities also when it comes to cooling. Theoretical investigations on direct cooling in concentrated laminar windings are presented in [13]. The laminar winding, however, presents manufacturing challenges and the solution is lacking experimental validation. In [14] a double layer tooth coil winding machine concept with in-slot cooling between the coils is presented and partly evaluated. This solution uses the space in the slot not filled with copper to create cooling channels by using water-soluble mould cores, a concept that is hard to adopt for mass production. Directly cooled axial flux PMSM using hollow conductors, and coolant flow in the axial direction, can also be found in literature [15]. The prototype presented uses Litz wire with a tube for liquid inside each turn, which is complicated to manufacture and yet the maximum feasible current density 14 A/mm² at 2 l/min is reported. A comparison between tooth coil winding PM machines with cooling jacket and direct cooling using hollow conductors is presented in [16]. A very interesting concept is used in [17], where a direct winding heat exchanger is used in between the coils of a double layer tooth coil winding machine. This setup allows for direct, in-slot water-cooling of the windings without exposing water to the winding copper wires. Current densities of 25 A/mm² continuous and 40 A/mm² peak operation are reported with this solution, with coolant flow rates up to 5.3 l/min and 5.1 kPa pressure drop. Copper heat exchangers in the slot, however, can be challenging when it comes to slot insulation and manufacturing, and the authors have not presented a complete rotating machine in hardware with their cooling concept. The authors of [18], [19] presents an in-slot cooling for a SRM, with dramatically increased cooling performance using water mantle cooling as reference. The concept is tested with DC current up to 22 A/mm² and a flow rate of 6 l/min, but this concept comes with some challenges regarding coolant leakage to the rotor.

The authors gratefully acknowledge the financial support from the Swedish Energy Agency and the Swedish Governmental Agency for Innovation Systems (VINNOVA).

A. Acquaviva, S. Skoog and T. Thiringer are with the Division of Electric Power Engineering at Chalmers University of Technology, Gothenburg, Sweden (e-mail: alessandro.acquaviva@chalmers.se, stefan.skoog@chalmers.se, torbjorn.thiringer@chalmers.se).

The purpose of this paper is to demonstrate effective and manufacturable high-performance cooling solution for a traction machine. The cooling solution presented in this paper, which combines direct iron and direct in-slot oil cooling, and experimentally verifying operation at very high current densities, is prior not found in the literature. The novelty consists in the integration of the cooling within the stator, using a thermally conductive epoxy resin to create the channels within the slot as well as the positioning of the stator yoke cooling channels. Neither of these solutions have been found in the literature. Additionally, the design of the end section to properly distribute the oil flow forms a high turbulence region which leads to very high cooling capability of the end windings. This is a clear advantage compared to an external cooling jacket, where end winding cooling is typically an issue. Regarding manufacturability, the machine is designed such that it is possible to use a linear winding machine to pre-wind the coils on a bobbin, leading to a significantly reduced manufacturing cost for high volume production. Also, the procedure to create the cooling channels within the slot, and extract the channel shapers, can be automated.

A calorimetric setup is used to measure the iron losses and to validate the CHT model of the machine and cooling at different flow rates. The convection heat transfer coefficients (HTC) from the CHT simulation are extracted and used in a transient thermal finite element simulation to evaluate the operation of the machine in worst-case conditions. Measurements are performed on the machine in thermal steady state operation at 17.5 A/mm^2 showing good agreement with the thermal simulations. The continuous operation at 25 A/mm^2 is verified in the worst case conditions with a thermal simulation. Results from both the transient simulation and measurements show that a current density of 35 A/mm^2 can be kept for 30 s peak operation without exceeding the thermal limits of the machine components.

II. MACHINE DESIGN

The electrical machine in this paper is designed as a traction machine for a small passenger vehicle, assuming it will operate with a fixed-gear reduction gearbox powering either of the vehicle wheel pairs. It is assumed that a liquid cooling circuit is available in the car, as in the vast majority of modern passenger electric vehicles on the market, and no additional cooling infrastructure is therefore needed for this cooling concept.

A. Electromagnetic sizing and design choices

The electromagnetic design is based on an analytical sizing method combined with a finite element mapping and verification. A 12 slot 10 pole (Q12p10) machine is chosen based on characteristics presented in [11]. Prioritized features are: high efficiency, high fundamental winding factor (0.933), low harmonic leakage inductance factor (0.97), low cogging torque, and low torque ripple. The machine is designed for the specifications listed in Table I.

The analytical sizing procedure used is based on split ratio optimization [20]. The split ratio, defined as the ratio between

internal to external stator diameter, is established to 0.62 to maximize the efficiency. The rotor geometry is chosen as an internal V-shaped PM with air barriers to enable high saliency which improves the field weakening characteristic. Embedding the magnets in the rotor also limits magnet losses caused by harmonics in the airgap MMF [21], [22]. Magnet segmentation axially is also utilized to further reduce the losses [22], [23]; each rotor slot is axially filled with 20 equal units of Vacodum 745DHR NdFeB-magnets.

A stator design without tooth tips is selected to improve manufacturability by allowing the coils to be pre-wound and inserted radially. The cogging torque and torque ripple are minimized by adjusting the PMs angle the pole pitch width and the tooth width. The resulting machine geometry is presented in Table II. The maximum phase current corresponds to a current density of 35 A/mm^2 . The stator and rotor lamination geometries as well as the coil disposition are shown in Fig. 1. In Fig. 2 the disposition of conductors and the shape of the stator are shown, including the cooling channels and the plastic support (bobbin) used to pre-wind the coils. PT100 temperature sensors (4 in the slots placed mid-axially and 3 on the end windings) are all placed before the potting process. The end winding temperature sensors are placed as follows with the same naming as in Fig. 1 and the legend in Fig. 16:

- one between slot 1 and 2 on the drive end side (EW1-DE)
- two between slots 5 and 6, one on the drive end (EW5-DE) and one on the non-drive end (EW5-NDE)

The coils of each phase are connected in parallel with the ones on the opposite side of the stator, as illustrated in Fig. 3. This choice is made in order to allow a higher number of turns, and therefore reduce the size of each conductor, which helps improving the manufacturing process as thinner and fewer parallel conductors are easier to wind.

B. Slot fill factor and cooling channels

The cooling channels are derived from unused space in the slot. The total slot area is 350 mm^2 . The cooling channel area in the slot is 100 mm^2 which gives a net slot area of 250 mm^2 . The copper area is 113 mm^2 , yielding a net fill factor of 0.45, while considering the total slot area yields a bulk fill factor of 0.32. The stator winding before and after potting is shown in Fig. 4. A wire diameter of 1.6 mm is the largest possible wire size that can be fitted in 28 turns when using manual winding process for this prototype.

The material used for the potting is an epoxy resin, Lord CoolTherm EP-2000, with a thermal conductivity of $1.9 \text{ W/(m} \cdot \text{K)}$.

TABLE I: Electrical machine design specifications.

Quantity	Symbol	Value	Unit
Peak torque	τ_{max}	140	Nm
Peak power	P_{max}	50	kW
Base speed	n_b	3 600	rpm
Max speed	n_{max}	11 000	rpm
Coolant max temperature	$\Theta_{max,c}$	60	$^{\circ}\text{C}$
Max winding temperature	Θ_{max}	180	$^{\circ}\text{C}$
DC bus voltage	V_{DC}	600	V
Maximum RMS current	I_{max}	140	A

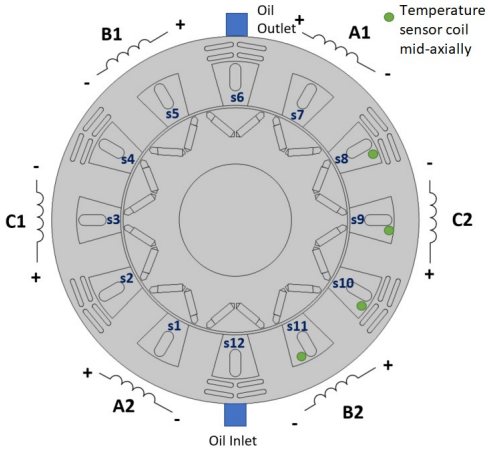


Fig. 1: Stator and rotor laminations geometry, slot naming, coil and temperature sensors disposition.

C. Stator yoke cooling channels

A machine with an even key winding factor [11] (e.g. two adjacent tooth-coils belonging to the same phase winding), such as the Q12p10 machine, presents negligible mutual inductance. This means that the flux generated by a single phase is enclosed between the two adjacent tooth coils and the yoke in between. A plot of the flux generated by 100 A in phase A and the PMs considered as air is shown in Fig. 5. The yoke in-between coils of different phases has a very low flux density. However, when the PM flux is added, parts of the PM flux would also flow in between coils of different phases but still with flux densities below 1.3 T. To sum up, the yoke in between phases is oversized in this design and some barriers for direct iron cooling can be created as shown in Fig. 5.

A similar solution with stator yoke barriers is adopted in

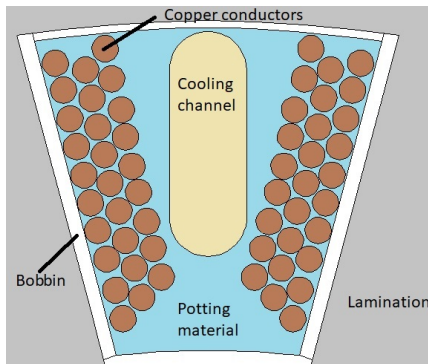


Fig. 2: Overview of a cross-section of the slot design showing in-stator cooling channel, winding layout, steel and potting material.

TABLE II: Electrical machine main dimensions and data.

Quantity	Symbol	Value	Unit
Outer Stator diameter	D_e	180	mm
Inner Stator diameter	D	111.4	mm
Active length	L	100	mm
Tooth width	w_t	17	mm
Stator Yoke width	w_{sy}	13	mm
Magnet thickness	h_m	3.5	mm
Diameter of each conductor	d_N	1.6	mm
Number of turns per coil	N	28	-

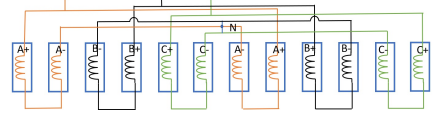


Fig. 3: Winding disposition and connection for the tooth-wound Q12p10 machine for balanced three-phase operation.

[21] to reduce sub-harmonics, which in turn would reduce both iron and PM losses in the Q12p10 machine. The main difference is that the position of the yoke barriers in [21] are shifted one slot and hence blocking part of the main magnetic flux within the adjacent coils in one phase. The drawback is a torque reduction, which for the Q12p10 used in this paper would be substantial according to several FEA cases where the yoke barrier thickness is varied as a parametric variable. The chosen thickness presents no torque reduction at full current compared to the solution without barriers.

D. End section

The stator end sections are filled with oil and flow stoppers are inserted as shown in Fig. 6 to redirect the oil in the two parallel paths, as illustrated in Fig. 7. The oil flow splits evenly thanks to the symmetry of the geometry on the two sides of the machine. The inlet and outlet are placed in correspondence to the iron cooling channels, which are a parallel fluid path with corresponding slot channel. This is done mainly to minimize the pressure drop from the whole flow passing through those channels.

III. NUMERICAL EVALUATION

The electromagnetic performance of the machine, including loss mapping, is evaluated using FEA. The losses are used as input for evaluating the thermal performance. A flow chart presenting how the models are built is shown in Fig. 8.

A. Electromagnetic FEA and loss mapping

The machine is mapped using equidistant operating points on the d-q current plane, and for each of those a set of 2D quasi-static magnetic FEA is performed. The losses are computed as in [24]. The eddy current and hysteresis loss factors are extracted from the lamination data sheet (M235-35). Copper losses are calibrated by measuring the total phase resistance with a high-current 4-wire setup. The iron losses are calibrated by measuring the heat generated while motoring



Fig. 4: Wound stator non-drive-end before (left) and drive-end after (right) potting. The oil cooling channels can clearly be seen as formed by the empty space between coils.

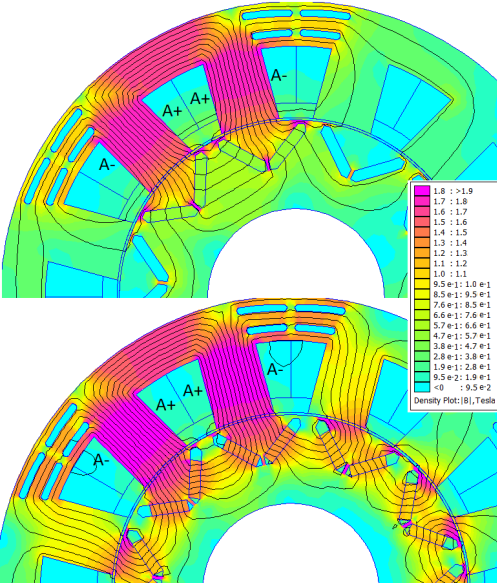


Fig. 5: Magnetic flux density generated by 100 A in phase A with and without PMs, respectively lower and upper sub-figure. The stator yoke cooling channels are actually assisting in lowering mutual flux between phases. The rotor position is chosen such that PMs are generating flux in the same direction as phase A.

the machine, with the dynamo at 3000 rpm and no electrical load, with the calorimetric set up described in Section IV. This resulted in an iron loss scaling coefficient of 2.0, meaning that the measured values of iron losses are twice the ones estimated with FEA using the interpolated loss coefficients from the soft iron manufacturer. Typical values of iron loss scaling coefficients found in the literature [25] are in the range between 1.5 and 2.0.

The torque-speed iron and copper loss maps, after the adjustments, are presented in Fig. 9.

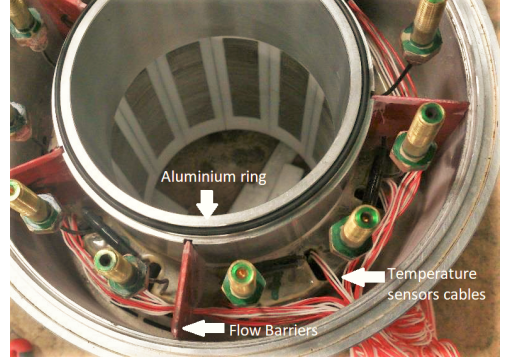


Fig. 6: Details of manufactured machine end section at non-drive-end showing the flow barriers between the slots and the phase connection terminals.

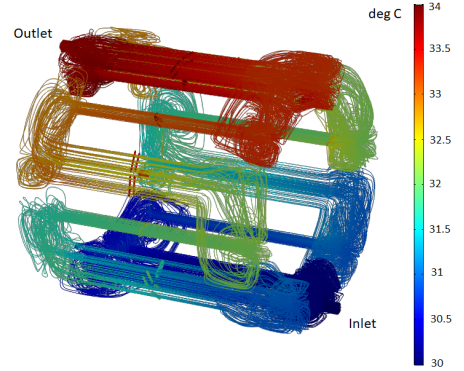


Fig. 7: Velocity streamlines showing the coolant flow path and the temperature increase from inlet to outlet at 6 l/min, inlet oil temperature of 30 °C and winding loading of 60 A_{DC} (15 A/mm²).

B. Conjugate heat transfer model

To verify the steady-state thermal performance of the machine, a 3D CHT model is built and solved for different flow rates. This multiphysics model combines CFD and thermal FEA. The losses are assigned as domain distributed heat sources and all the materials are assigned with thermal properties. Using a similar approach as in [8], the material modeling includes

- Anisotropic thermal conductivity of iron lamination stack
- Anisotropic thermal conductivity of coils
- Dynamic viscosity, heat capacity and thermal conductivity of the coolant is considered as a function of temperature
- The air in the airgap is modelled with an equivalent thermal conductivity to account for the convection effect at a given speed based on [26]

The winding and slot insulation/filler are modelled as a

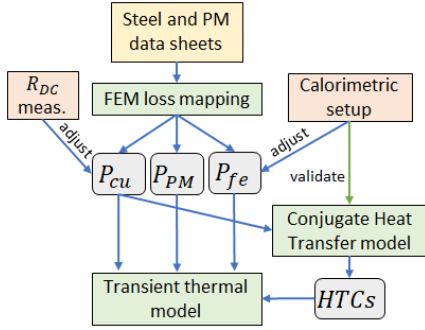


Fig. 8: Flow chart of development and calibration of FEA and CHT simulation models.

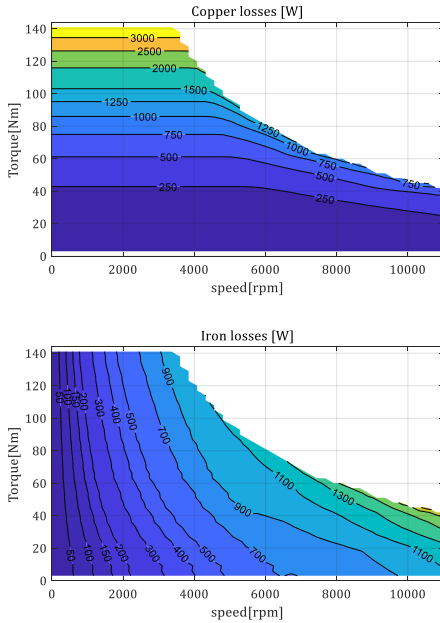


Fig. 9: Iron and copper losses from FEA machine mapping.

unified material. In [27] a model is derived that predicts the equivalent thermal conductivity of a composite material consisting of aligned, infinitely long, equi-sized, rigid, circular cylinders (i.e., the copper conductors) randomly distributed in a medium with lower conductivity (i.e. slot filler). This value depends on the fill factor and the thermal conductivity of the two materials. The value obtained is $4.8 \text{ W}/(\text{m} \cdot \text{K})$, and this value of thermal conductivity is used for the plane parallel to the lamination (referred as x and y directions), while a weighted thermal conductivity of copper and epoxy-resin, resulting in $118 \text{ W}/(\text{m} \cdot \text{K})$, is used in the axial direction (referred as z direction). This method allows to avoid modeling

each conductor and to decrease the complexity of the model. A similar approach, with different material proportions, is used for the end winding, resulting in a $\lambda_{slot,xy}$ of $63 \text{ W}/(\text{m} \cdot \text{K})$ and $\lambda_{slot,z}$ of $3 \text{ W}/(\text{m} \cdot \text{K})$.

The resulting surface temperature distribution, at 2 l/min and assuming only copper losses with a current of 60 A_{DC} , is presented in Fig. 10. For the same loading condition the temperature distribution in the middle of the axial length of the machine for different flow rates is presented in Fig.11.

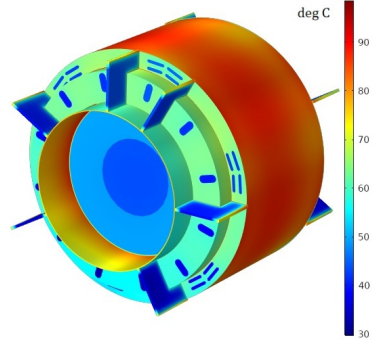


Fig. 10: Surface temperature distribution with 60 A_{DC} (15 A/mm^2), oil inlet temperature of 20°C and 2 l/min flow rate.

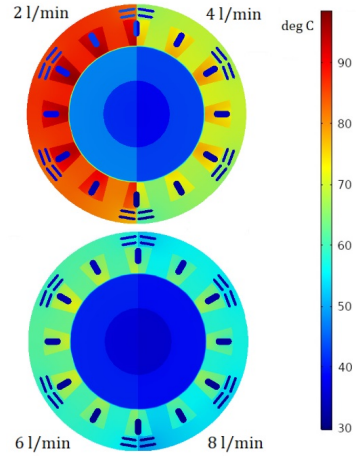


Fig. 11: Motor temperature distribution with 60 A_{DC} (15 A/mm^2), oil inlet temperature of 20°C and four different oil flow rates. The simulated temperatures are symmetrical for the two motor halves and hence only one half is shown per oil flow rate.

The CHT model accounts for the effect of increasing resistance with temperature. The distributed heat source is a

function of the local temperature using the equation

$$P_{cu,T} = P_{cu,T_0}(1 + \alpha(T - T_0)) \quad (1)$$

where P_{cu,T_0} and $P_{cu,T}$ are respectively the copper losses at the reference temperature T_0 at which the phase resistance is estimated and at the temperature T of the winding which is updated at each time step of the simulation; α is the temperature coefficient of copper. End winding joule losses are distributed to the corresponding domain.

C. Transient thermal model

The CHT model is computationally very demanding, about 9 hours to solve a single steady state operating point on a workstation with an Intel i7-6700K CPU operating at 4 GHz. Transient analysis using a standard workstation is not feasible. However, it is possible to extract the convection HTC's for the different solid to fluid surfaces and use them as a boundary condition for a thermal FEA simulation (without the CFD part), which has orders of magnitude lower computational effort. A 60 s transient simulation, with 0.1 s time stepping, can be solved in less than 10 minutes with the same workstation mentioned above. The transient thermal model has the same geometry, meshing, material characterization and loss distribution of the CHT model solid parts, but no fluid modelled.

The HTC's, extracted from the CHT simulation, at different flow rates are presented in Fig. 12. These are calculated as average over the surface of the specific part and in reference to the inlet temperature. The two halves of the machine are symmetrical, and hence the HTC's of the slots on the left and right side of the machine are equal.

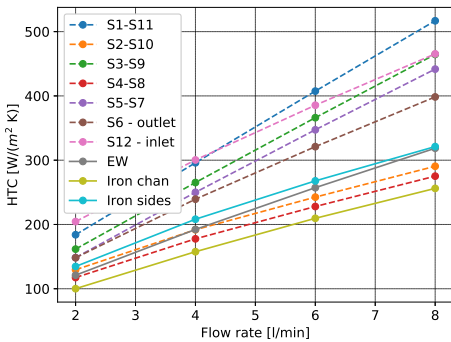


Fig. 12: Convection heat transfer coefficients from coils in slot number S to coolant oil, established by CHT simulation at different flow rates.

The software used for the different physics as well as the number of mesh nodes for the models built are presented in Table III.

TABLE III: Software and mesh data

Physics	Software	Dimensions	n. mesh nodes
Electromagnetics	FEMM	2D	41575
Complete CHT	COMSOL	3D	231370
Trans. therm. Model	COMSOL	3D	121179

IV. TEST SET UP

The machine is tested in a lab environment consisting of a electric dynamometer, power electronics, and a custom made oil-to-water cooling system. The setup is illustrated in Fig. 13 and a photo is also shown in Fig. 14. Appropriate sensors are installed and calibrated to measure rotational torque (τ), rotational speed (n), rotational position (θ), oil flow (\dot{m}), oil temperatures (T), oil pressures (p) and electrical voltages (v) and electrical currents (i). The custom cooling system utilizes tap water which is flow-controlled with a feedback PI-controller into a heat exchanger to cool the oil circulated in the machine. The low-viscous oil is circulated by a 100 W controlled gear pump capable of generating 3 bar overpressure or 7 l/min flow rate. An oil reservoir and a 10 μ m particle filter is also part of the oil cooling circuit. The direct heat measurement is based on measuring the temperature difference of the inlet and outlet oil in the prototype machine together with the oil flow. Redundant Swissflow SF-800 sensors are used for flow measurements, several NTC sensors as well as 16 4-wire PT-100 class A sensors are redundantly measuring oil temperatures to offer high accuracy and high reliability for the prototype setup. The entire test system is controlled and monitored through a dSpace SCALEXIO-system. The prototype machine is fed with a three-leg IGBT-based inverter at 400 V_{DC}, operating at 5 kHz Space Vector Modulation closed-loop current control. The dynamometer is operating at closed-loop speed control.

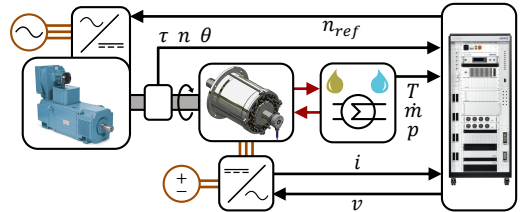


Fig. 13: Measurement system setup with dynamometer to the left, prototype machine in the middle connected to a calorimetric oil-to-water cooling system and controlled by a dSpace rack.

The coolant oil used for the prototype machine is provided by ExxonMobil and specifically developed for electrical machine cooling, featuring low viscosity and good thermal properties as shown in Table IV.

V. RESULTS

In order to validate the CHT model, the temperatures of the different slots and end windings are compared with the

TABLE IV: Oil coolant properties (data from ExxonMobil).

	40 °C	80 °C	100 °C
Kinematic viscosity (cSt)	2.31	1.28	1.02
Specific heat (J/kgK)	2.15	2.28	2.35

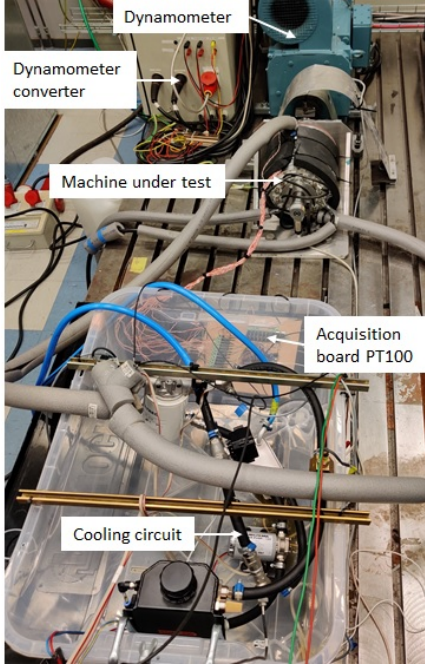


Fig. 14: Photo of calorimetric and dynamometer setup.

temperature sensors available in the machine. In the CHT model the sensors are placed in a position which corresponds to the ones presented in Fig. 1.

A. DC current measurements and CHT validation

Both CHT simulations and physical measurements are performed at 60 A_{DC} (ca 800 W copper losses) as the only heat source, rotor at stand still, and with three different oil flow rates. Results comparing the CHT simulation and the measurements are presented in Fig.15 for the slot sensors, and in Fig.16 for end winding sensors. The measurements-to-simulations relative error in percent is presented in Tab. V, defined as

$$dT_{\%} = \frac{T_{meas} - T_{sim}}{T_{meas} - T_{inlet}} * 100 \quad (2)$$

where T_{meas} and T_{sim} are respectively the measured and simulated values and T_{inlet} is the oil inlet temperature (20°C).

The winding temperature prediction is in good agreement considering that there has been no correction factor of geometry or material properties to fit the measurements. The temperature sensors are buried in the potting material (in contact with the coil) and the thickness of the epoxy resin

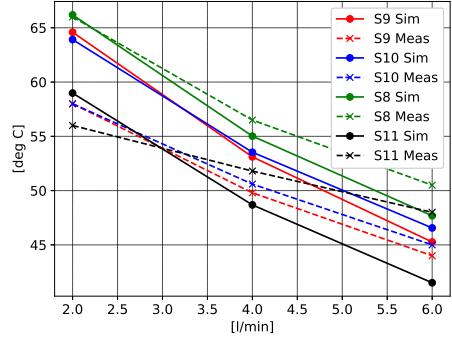


Fig. 15: Measured and simulated slot temperatures.

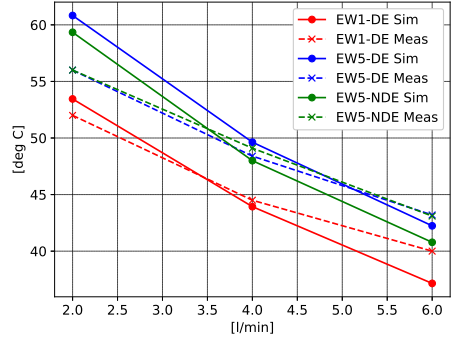


Fig. 16: Measured and simulated end winding temperatures.

between the sensor and the surface of the cooling channel greatly affects the temperature measurement. The uncertainty on the placement of these sensors is the major source of error. A similar measurement was performed in [8] on a machine with cooling jacket reporting errors between simulation and sensor readings in the order of 3-5%. For the cooling solution adopted in this paper, the highest temperatures are found at high machine load are found in the molded coils axially mid-way through the slot. The end-windings are extremely well cooled according to measurements and simulation results.

To evaluate the pressure drop, a CFD simulation of the cooling path is built, considering the oil viscosity at 20°C and modeling the bolts, which are generating turbulence in the end section. The pressure drop from the CFD simulation and the measurements (pressure sensors placed at inlet and outlet of the machine) are presented in Tab. VI. The measured pressure drop is significantly higher than the simulated values. This is due to the fact that the CFD simulation does not include all the parts in the end section, such as adjacent coil connection joint, and the invasive presence of the temperature sensors cables which are being partly routed through the cooling channel.

TABLE V: Percentage relative error temperature sensors.

Sensor	2 l/min	4 l/min	6 l/min
S8	-0.4	4	9.2
S9	-17.3	-11	-5.3
S10	-15.5	-9.5	-6.2
S11	-8.3	9.7	23
EW1-DE	4.5	2.3	14.2
EW5-DE	-13.4	-4.3	4.1
EW5-NDE	-9.3	3.8	10

These can significantly affect the turbulence, and consequently the pressure drop. The measured pressure drop at the highest flow rate of 6 l/min, is considered low enough for a standard 12 V automotive oil pump to be used. The electrical power required by the pump at 6 l/min and oil temperature of 20°C is ca 10 W.

TABLE VI: Oil pressure drops comparison.

	2 l/min	4 l/min	6 l/min
CFD [kPa]	2.9	6.6	12.7
Measured [kPa]	4.9	18.4	37.6

B. Continuous operation validation

Having the oil flowing in close proximity to the winding and directly in the stator iron significantly reduces the thermal transient of the stator. Two thermal time constants can be identified; the stator thermal steady state is reached after 30 minutes of operation, however due to the high thermal resistance of the airgap the rotor thermal transient is about twice as long. A thermal transient simulation is carried out to verify the continuous operation condition with the following conditions: initial oil temperature of 60°C, constant oil flow rate 6 l/min, rated speed 3600 rpm, and 100 A_{RMS} (25 A/mm²). As seen in Fig. 17, all temperatures are below the 180°C limit which validates the continuous operating condition in worst case circumstances.

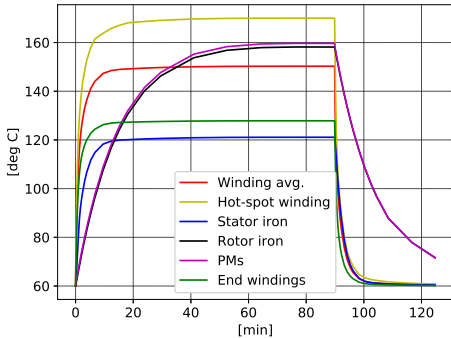


Fig. 17: Transient simulation for continuous operating condition at initial and oil temperature of 60°C, constant flow of 6 l/min, 3600 rpm and 100 A_{RMS} (25 A/mm²).

Measurements for continuous operation have been carried out with 70 A_{RMS} (17.5 A/mm²) and a constant speed of 1000 rpm, input oil at 20°C and oil flow rate at 6 l/min. The simulated and measured temperature rise are presented in Table VII.

TABLE VII: Steady state temperature rise at 17.5 A/mm², speed of 1000 rpm and oil flow rate of 6 l/min

	Measured	Simulated
End Winding	26.0°C	32.6°C
Mid-Slot	35.2°C	42.1°C

C. Peak operation validation

To verify the peak operation condition, a transient simulation is carried out at an initial temperature of 90°C and oil temperature of 60°C, constant flow of 6 l/min, rated speed 3600 rpm and 140 A_{RMS} (35 A/mm²). As seen in Fig. 18, winding hot-spot reaches 180°C after 30 s, which defines the peak operating condition in worst case circumstances.

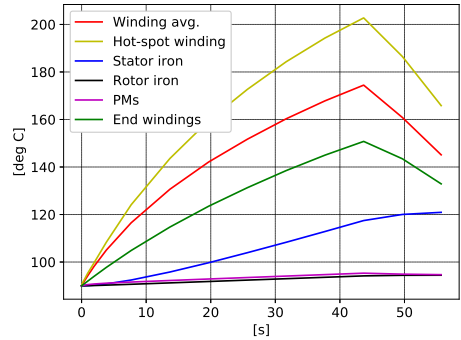


Fig. 18: Transient simulation for peak operating condition at initial machine temperature of 90°C, oil temperature of 60°C, constant flow of 6 l/min, 3600 rpm and 140 A_{RMS} (35 A/mm²).

Measurements for peak torque, 140 A_{RMS} , are carried out at 150 rpm. The input oil temperature is approximately 20°C and oil flow of 6 l/min. The readings of the warmest sensors are depicted in Fig. 19 and compared to simulated values, confirming that all temperatures are well within the limits. The winding temperature measurements are partly interrupted by interference of PWM operation at high currents in this setup. The difference between simulated and measured temperatures is again mainly due to uncertainty in the placement of the sensor.

VI. CONCLUSION

In this paper a novel design and construction of an in-slot and in-stator direct oil cooled tooth coil winding machine is presented which enables current densities of 25 A/mm²

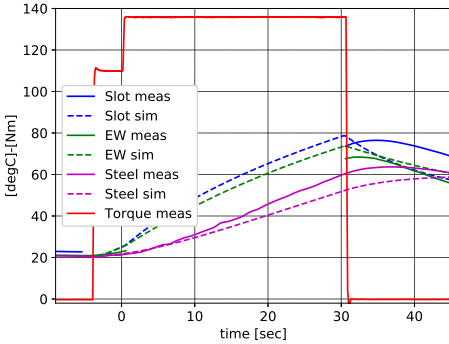


Fig. 19: Peak torque operation ($140 A_{RMS}$, $150 rpm$) for 30 s at starting temperature and oil temperature of about $20^{\circ}C$. Solid lines showing measured values of the warmest sensor for the part considered. Dashed lines are simulated values.

continuously and $35 A/mm^2$ for 30 s peak operation at oil flows of $6 l/min$ and $42 kPa$ pressure drop. Such high current densities have not been found in the literature from full rotating experiments for a similar sized machine. Although the machine is tested at max $3000 rpm$, the FEA models indicate that the target of $50 kW$ can easily be met at slightly higher speed. The hot spots of the motor is found mid-slot, which proves that the end-windings are very well cooled by the coolant oil flow.

The slot cooling channels are created using a high thermal conductivity potting material and can be successfully simplified in FEA modeling using an equivalent composite material. A conjugate heat transfer simulation is developed to characterize the cooling performance and run using the losses from electromagnetic finite element simulations. Convection heat transfer coefficients are extracted and used to simulate the transient operating condition. The model-to-measurement temperature deviations are within a few percent (and within a few $^{\circ}C$), proving the usefulness of the simplified thermal model.

VII. BIOGRAPHIES



Alessandro Acquaviva received a double M.Sc at Politecnico di Torino and KTH, Stockholm, Sweden in 2012. After four years in traction electrification industry and completing an MBA he is currently pursuing his Ph.D. at Chalmers University of technology in Gothenburg, Sweden. His areas of interest include the modeling, control and design of electrical machines and power electronics with focus on automotive applications.



Stefan Skoog was born 1985, graduated as M.Sc.E.E from Lund University, Sweden in 2010. Stefan has a decade of professional experience in R&D in advanced mechatronics and automotive powertrains. He is currently a PhD student at Chalmers University, Sweden, working on mild hybrid electrification systems limited to 48 VDC aimed for personal vehicles. His interests include modeling, design and verification of advanced battery systems, power electronics and electric machines.



Torbjörn Thiringer works at Chalmers university of Technology, in Gothenburg, Sweden, as a professor in applied power electronics. He took his M.Sc and Ph.D at Chalmers University of technology in 1989 and 1996 respectively. His areas of interest include the modeling, control and grid integration of wind energy converters into power grids as well as power electronics and drives for other types of applications, such as electrified vehicles, buildings and industrial applications.

REFERENCES

- [1] E. A. Grunditz and T. Thiringer, "Performance analysis of current bevs based on a comprehensive review of specifications," *IEEE Transactions on Transportation Electrification*, vol. 2, no. 3, pp. 270–289, Sep. 2016.
- [2] J. Pyrhönen, T. Jokinen, and V. Hrabovcova, *Design of rotating electrical machines*. John Wiley & Sons, 2009.
- [3] J. R. Hendershot and T. J. E. Miller, *Design of brushless permanent-magnet machines*. Motor Design Books, 2010.
- [4] K. T. Chau, C. C. Chan, and C. Liu, "Overview of permanent-magnet brushless drives for electric and hybrid electric vehicles," *IEEE Trans. on Industrial Electronics*, vol. 55, no. 6, pp. 2246–2257, 2008.
- [5] A. Carriero, M. Locatelli, K. Ramakrishnan, G. Mastinu, and M. Gobbi, "A review of the state of the art of electric traction motors cooling techniques," *SAE Technical Paper*, vol. 2018-01-0057, 2018.
- [6] M. Popescu, D. A. Staton, B. Aldo, C. Andrea, H. Douglas, and G. James, "Modern heat extraction systems for power traction machines," *IEEE Transactions on Industry Appl.*, vol. 52, no. 3, pp. 2167–2175, Mar. 2016.
- [7] Y. Gai, M. Kimiabeigi, Y. Chuan Chong, J. D. Widmer, X. Deng, M. Popescu, J. Goss, D. A. Staton, and A. Steven, "Cooling of automotive traction motors: Schemes, examples, and computation methods," *IEEE Transactions on Industrial Electronics*, vol. 66, no. 3, pp. 1681–1692, Mar. 2019.
- [8] A. Acquaviva, O. Wallmark, E. A. Grunditz, S. T. Lundmark, and T. Thiringer, "Computationally efficient modeling of electrical machines with cooling jacket," *IEEE Transactions on Transportation Electrification*, vol. 5, no. 3, pp. 618–629, Sep. 2019.
- [9] A. Boglietti, A. Cavagnino, D. Staton, M. Shanel, M. Mueller, and C. Mejuto, "Evolution and modern approaches for thermal analysis of electrical machines," *IEEE Transactions on Industrial Electronics*, vol. 56, no. 3, pp. 871–882, Mar. 2009.
- [10] A. M. El-Refaie, "Fractional-slot concentrated-windings synchronous permanent magnet machines: Opportunities and challenges," *IEEE Trans. on industrial Electronics*, vol. 57, no. 1, pp. 107–121, 2010.
- [11] S. Skoog and A. Acquaviva, "Pole-slot selection considerations for double layer three-phase tooth-coil wound electrical machines," in *ICEM '18, Alexandroupoli*, 2018.
- [12] F. Libert and J. Soulard, "Investigation on pole-slot combinations for permanent-magnet machines with concentrated windings," in *Int. Conference on Electrical Machines (ICEM)*, pp. 5–8, 2004.
- [13] A. Reinap, F. J. Marquez-Fernandez, M. Alaküla, R. Deodhar, and K. Mishima, "Direct conductor cooling in concentrated windings," in *ICEM '18, Alexandroupoli*, 2018.
- [14] M. Schiefer and M. Doppelbauer, "Indirect slot cooling for high-power-density machines with concentrated winding," in *IEMDC '15*, pp. 2167–2175, 2015.
- [15] G. Dajaku, W. Xie, and D. Gerling, "Reduction of low space harmonics for the fractional slot concentrated windings using a novel stator design," *IEEE Transactions on Magnetics*, vol. 50, no. 5, 2014.
- [16] P. Lindh, I. Petrov, A. Jaatinen-Väri, A. Grönman, M. Martinez-Iturralde, M. Satrustegui, and J. Pyrhönen, "Direct liquid cooling method verified with an axial-flux permanent-magnet traction machine prototype," *IEEE Transactions on Industrial Electronics*, vol. 64, no. 8, pp. 6086–6095, Aug. 2017.
- [17] I. Petrov, P. M. Lindh, M. Niemela, E. Scherman, O. Wallmark, and J. J. Pyrhonen, "Investigation of a direct liquid cooling system in a permanent magnet synchronous machine," *IEEE Transactions on Energy Conversion*, pp. 1–1, 2019.
- [18] S. A. Semidey and J. R. Mayor, "Experimentation of an electric machine technology demonstrator incorporating direct winding heat exchangers," *IEEE Transactions on Industrial Electronics*, vol. 61, no. 10, pp. 5771–5778, Oct. 2014.
- [19] Z. Liu, T. Winter, and M. Schier, "Direct coil cooling of a high performance switched reluctance machine (srm) for ev/hev applications," *SAE International Journal of Alternative Powertrains*, vol. 4, no. 1, pp. 162–169, 2015.
- [20] Z. Liu, T. Winter, and M. Schier, "Comparison of thermal performance between direct coil cooling and water jacket cooling for electric traction motor based on lumped parameter thermal network and experimentation," in *Proceedings of the EVS28 International Electric Vehicle Symposium and Exhibition, Goyang, Korea*, pp. 3–6, 2015.
- [21] A. Acquaviva, "Analytical electromagnetic sizing of inner rotor brushless pm machines based on split ratio optimization," in *ICEM '18, Alexandroupoli*, 2018.
- [22] B. Aslan, E. Semail, J. Korecki, and J. Legranger, "Slot/pole combinations choice for concentrated multiphase machines dedicated to mild-hybrid applications," in *IECON 2011-37th Annual Conference of the IEEE Industrial Electronics Society*, pp. 3698–3703. IEEE, 2011.
- [23] K. Yamazaki and Y. Fukushima, "Effect of eddy-current loss reduction by magnet segmentation in synchronous motors with concentrated windings," *IEEE Transactions on Industry Applications*, vol. 47, no. 2, pp. 779–788, 2011.
- [24] A. Alessandro, A. G. Emma, S. Lundmark, and T. Thiringer, "Comparison of mtpa and minimum loss control for tooth coil winding pmsm considering pm and inverter losses," in *EPE 2019*, 2019.
- [25] P. Ponomarev, M. Polikarpova, and J. Pyrhönen, "Thermal modeling of directly-oil-cooled permanent magnet synchronous machine," in *2012 XXth International Conference on Electrical Machines*, pp. 1882–1887. IEEE, 2012.
- [26] J. Nerg, M. Rilla, and J. Pyrhonen, "Thermal analysis of radial-flux electrical machines with a high power density," *IEEE Trans. on Ind. Electronics*, vol. 55, no. 10, pp. 3543–3554, Oct. 2008.
- [27] G. W. Milton, "Bounds on the transport and optical properties of a two-component composite material," *J. Appl. Phys.*, vol. 52, pp. 5294–5304, 1981.

Paper VII

Electromagnetic and Calorimetric Validation of Direct Oil Cooled Tooth Coil Winding PM Machine for Traction Application

Submitted 2020-05-17 to MDPI Energies

First author contributions

Lead machine design FEA, thermal and mechanical, idea generation,
data processing and analysis, FEA figures, figure generation.

Second author contributions





Lead in design, construction and calibration of measurement setup,
data acquisition, idea development.

Third, fourth author

Paper review, paper structure, idea revision, supervision,
administration, resource allocation, funding.

Article

Electromagnetic and Calorimetric Validation of Direct Oil Cooled Tooth Coil Winding PM Machine for Traction Application

Alessandro Acquaviva ^{1,*} , Stefan Skoog ¹ , Emma Grunditz ¹  and Torbjörn Thiringer ¹ 

¹ Chalmers University of Technology

* Correspondence: alessandro.acquaviva@chalmers.se; Tel.: +46-735704363

Version May 17, 2020 submitted to Energies

Abstract: Tooth coil winding machines offer a low cost manufacturing process, high efficiency and high power density, making these attractive for traction applications. Using direct oil cooling in combination with tooth coil windings is an effective way of reaching higher power densities compared to an external cooling jacket. In this paper, the validation of the electromagnetic design for an automotive 600 V, 50 kW tooth coil winding traction machine is presented. The design process is a combination of analytical sizing process and FEA optimization. It is shown that removing iron in the stator yoke for cooling channels does not affect electromagnetic performance significantly. The machine is designed, manufactured and tested continuously at 105 Nm with 25 A/mm² and at 145 Nm with 35 A/mm² 10 s peak during 6 l/min oil cooling. Inductance, torque and back EMF are measured and compared with FEA results showing very good agreement with the numerical design. Furthermore, the efficiency of the machine is validated by a direct loss measurements, using a custom built calorimetric set-up in six operating points with an agreement within 0.9 units of percent between FEA and measured results.

Keywords: Permanent magnet machines, Electromagnetic design, Model verification, Performance evaluation, Calorimetric measurement, Oil cooling, Efficiency validation

1. Introduction

In recent years, research and development of automotive electric traction machines has greatly intensified. Apart from high efficiency and low cost, a specific design target for these machines is high power density (i.e. power per volume) [1–3]. Aiming for high power density means maximizing the material utilization of the machine, which is essential to achieve cost-effective solutions for mass-production, and low package volumes that enables effective system packaging.

Therefore, high-power density electric machines as well as power electronics, are seen by the US department of energy as critical enablers of large-scale electric vehicle adoption [2]. The previous technical target specified in the US DRIVE Technology Roadmap for 2020 was 5.7 kW/liter for a 55 kW peak machine. However, the latest target for 2025 is 50 kW/liter for a 100 kW peak machine. Even though existing solutions are well positioned for the 2020 target, significant challenges lies ahead to live up to the next generation of traction systems in year 2025. This is exemplified in Table 1, which provides a comparison of power densities, both net (total volume of active steel) and gross (volume of complete electric machine casing), for state-of-the-art automotive electric traction machines.

High-power density electric machines can be achieved by utilizing factors such as:

- high mechanical speed [3], by a high electric frequency, or high pole number [4]
- high airgap flux density (i.e. magnetic loading), eg. by using high energy magnets, or a field winding excitation, both in combination with core material with a high saturation[5]

- high current loading, or high current density, while simultaneously assuring a low thermal resistance between the winding and coolant

For the sake of high magnetic loading, the development of electric drive-trains is primarily dominated by the permanent magnet synchronous machine (PMSM) [6], characterized by its high power density as well as high efficiency [1,7,8]. However, as identified in [2], to reach even higher power density, more research is required regarding “improved thermal materials”, as well as “advanced cooling/thermal management techniques to reduce size, cost and improve reliability”. Extensive engineering efforts are devoted to solve these challenges, as summarized well in [9–11]. An apparent aim is to try to bring the coolant medium closer to the main sources of heat, i.e. the stator core and winding, as opposed to so called cooling jackets.

One possibility is then to use a tooth-coil winding machine (TCWMs), also known as non-overlapping fractional slot concentrated winding (FSCW) machine. With this machine type, it may be possible to devote some of the space that is normally used for active material, for cooling channels instead, without sacrificing performance. Still, it offers high torque density and high efficiency [12–14] when combined with a permanent magnet (PM) rotor, as well as low cost manufacturing. In [15], a 12-slot 8-pole TCWM for traction application is compared with a distributed winding (DW) interior-magnet, a switched reluctance, and an induction machine. The TCWM is shown to perform best in terms of torque density, even without considering the shorter winding overhang. Efficiency-wise, the two PM machines are comparable, TCWM being slightly better in the low speed region and less efficient at high speeds compared to the DW machine. Other interesting traction motor designs using TCWM are presented in [16–20], however, without the integration of direct cooling in the stator, continuous current densities above 20 A/mm² are hardly reached, which limits the torque density.

Previous proposals of high performing liquid cooling techniques for TCWMs comprise examples such as the following:

- using conductive pipes in the slots, with the drawback of generating large eddy current losses [21]
- theoretical evaluation of the concept of flushing the entire stator and rotor with oil coolant [22]
- direct-water cooled coils by winding a coolant carrying steel pipe with litz wire, validated in a 205 kW machine for a bus application [23]
- using fluid guiding structure and airgap sealing to allow for oil cooling within the slots [24].

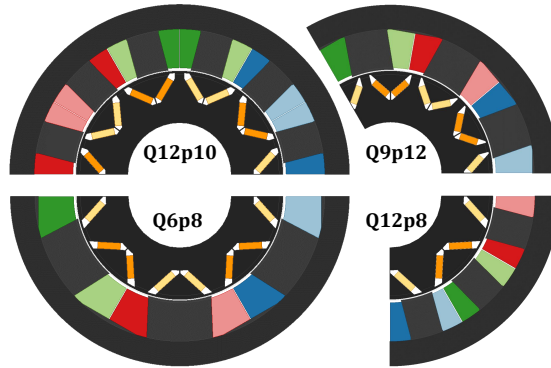
Neither of these examples though, have reached the levels of power density and efficiency that is presented in this paper, nor have they experimentally verified as high current densities.

Enabling high current density, which in turn means high copper losses at peak operation, does not preclude the traction machine to achieve high energy efficiency. The reason is that during driving, the machine operates most of the time in part-load, i.e. the low torque region, as shown for several drive cycles in [25]. Achieving high energy efficiency can significantly extend the range of the vehicle for a given battery pack.

This purpose of this paper is to present the electromagnetic design and verification of a high-power density, high-efficiency 50 kW TCWM, sized for traction application of passenger vehicles. The high power density is achieved by integration of direct-oil cooling in the stator yoke as well as in the slot via a potting material with high thermal conductivity, which shapes the cooling channels. The details of the design and verification of the cooling solution are presented by the authors in [26]. This paper instead focuses on the electromagnetic design validation. Particularly, it is shown how the placement of stator yoke oil cooling channels can be done without affecting the electromagnetic performance, which has not been found in literature. Experimental validation of the torque, no-load EMF and inductance present a very good match with simulations. Furthermore, the efficiency is verified through a direct loss measurement in a custom-made calorimetric set-up, also showing a good match with simulated results. Finally, the paper guides the reader through the main choices and steps for the design of a traction PM-TCWM intended for high volume production.

Table 1. Performance metrics for traction machines

Machine	Net Power Density (kW/l)	Gross Power Density (kW/l)	Peak Efficiency
Toyota HSD 2010 [27]	22	5.2	96% [27]
BMW i3 [3]	20	9.2	94% [28]
Machine presented here	19	6.7	95%
DoE Target 2020 [2]	-	5.7	-
DoE Target 2025 [2]	-	50	-

**Figure 1.** Smallest unique section of rotor and stator geometries for the four TCWM slot-pole combinations evaluated through FEA.

2. Machine design

The target application of the machine in this paper is a traction motor for either a small passenger vehicle, or an assist motor in a plug-in hybrid electric vehicle. The traction machine is assumed to operate with a fixed-gear reduction gearbox, powering either of the vehicle wheel pairs, and able to operate with a large field-weakening window. The design specifications are listed in Table 2.

2.1. Electromagnetic analytical sizing and design choices

The electromagnetic design is based on an analytical sizing method combined with a finite element mapping and verification. Given the target power rating, a desired high power density, and the ability to gear the machine, an axially long and radially small machine is selected to achieve high mechanical speeds. A fundamental frequency of 1.2 kHz is assumed at maximum speed, limited by machine iron losses and the maximum switching frequency (typically 10 kHz) together with a reasonable frequency modulation index of a high-performance traction inverter. A pole-pair number of five or six will now set the maximum mechanical speed to 14.4 and 12 krpm, respectively. Using the methodology presented in [13], the only slot (Q) - pole (p) options left for a balanced three-phase machine are Q6p8, Q12p8, Q12p10 and Q9p12, all illustrated in Fig. 1. A FEA comparison between these four feasible pole-slot combinations in terms of output torque and iron losses at 300 Hz electrical frequency is shown in Fig. 2. This comparison is done keeping the main geometrical parameters (material types, axial length, stator external and internal diameter, airgap length, tooth embrace) and loading parameters (current density, airgap flux density) constant in all the designs. The Q12p10 machine presents the highest torque density and lowest iron losses among the machines compared, as can be seen in Fig. 2. Furthermore the Q12p10 offers the best balance between high fundamental winding factor (0.933), low harmonic leakage inductance factor (0.97), and high cogging frequency, all numbers are derived in [13].

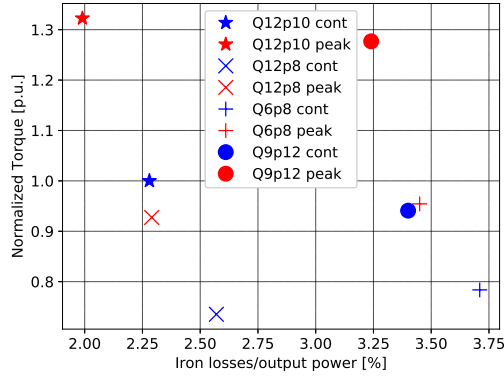


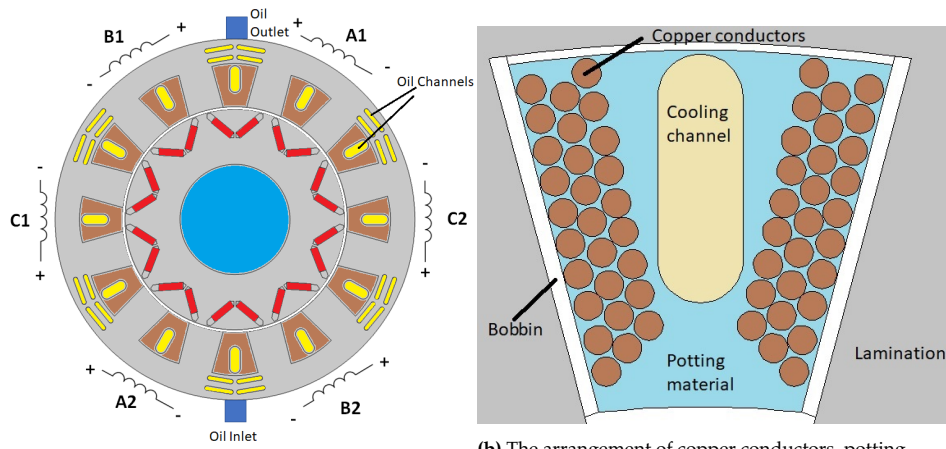
Figure 2. Numerical comparison of the different pole slot combinations for peak and continuous operation. The machines have the same volume, airgap flux density and current density. The torque is normalized to the Q12p10 machine in continuous operation.

The analytical sizing procedure, presented in [29], is based on the split ratio optimization. The split ratio, defined as the ratio between internal to external stator diameter, in fact can be used as a main parameter to size the machine. The analytical model is built by writing the torque equation of the brushless PM machine as a function of the main geometrical parameters and the two main loading parameters, airgap flux density and current density. It is shown in [29] that the choice of the split ratio is a trade-off between efficiency and torque density. In the design presented in this paper the split ratio is chosen to maximize the efficiency, resulting in 0.62. The choice is also driven by thermal considerations; a low value of split ratio leads to a high copper and slot area, which, for a fixed current density, means critical cooling requirements. A stator design without tooth tips is chosen to improve manufacturability by allowing the coils to be pre-wound outside the stator and inserted radially. The rotor is chosen as an internal V-shaped PM with air barriers to enable high saliency which improves the field weakening (FW) characteristic. Embedding the magnets in the rotor also limits magnet losses caused by harmonics in the airgap MMF [30,31]. One additional measure taken to limit excessive magnet losses is magnet segmentation [31,32] by using 20 equal Vacodym 745DHR NdFeB magnet units stacked axially in each rotor slot.

The resulting machine parameters are listed in Table 3. The maximum phase current corresponds to 35 A/mm² current density in the copper conductors. The coil disposition and geometries of stator and rotor with details about disposition of conductors and cooling channels are shown in Fig. 3. The Q12p10 machine has a key winding factor [13] of 2, meaning each phase coil consist of two electrically series connected coils on adjacent teeth. Each coil has 28 turns, which allows for a 1.6 mm diameter enamel copper wire to be used and avoiding parallel strands in the coils. Having a bobbin which can

Table 2. Electrical machine design specifications

Quantity	Symbol	Value	Unit
Peak torque	T_{max}	140	Nm
Peak power	P_{max}	50	kW
Base speed	n_b	3 600	rpm
Max speed	n_{max}	11 000	rpm
Coolant max temperature	$\Theta_{max,c}$	60	°C
Max winding temperature	Θ_{max}	180	°C
DC bus voltage	V_{DC}	600	V



(a) Stator and rotor laminations geometry, coil disposition and cooling channels.

(b) The arrangement of copper conductors, potting material and oil cooling channel within one slot.

Figure 3. Details of lamination geometry, cooling channels and conductor disposition.

be inserted, limiting the conductor diameter and avoiding parallel strands enables the use a linear winding machine, which can drastically reduce the manufacturing cost at high volume production. Each set of two series coils are then parallel connected to form a full phase winding, as shown in Fig. 4.

Table 3. Electrical machine main dimensions and data

Quantity	Symbol	Value	Unit
Outer Stator diameter	D_e	180	mm
Inner Stator diameter	D	111.4	mm
Active length	L	100	mm
Tooth width	w_t	17	mm
Stator Yoke width	w_{sy}	13	mm
Magnet thickness	h_m	3.5	mm
Diameter of each conductor	d_N	1.6	mm
Number of turns per coil	N	28	-
Maximum RMS current	I_{max}	140	A

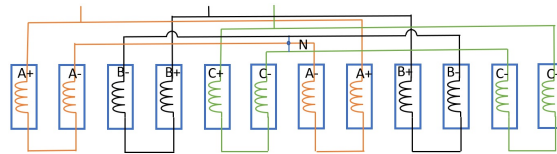


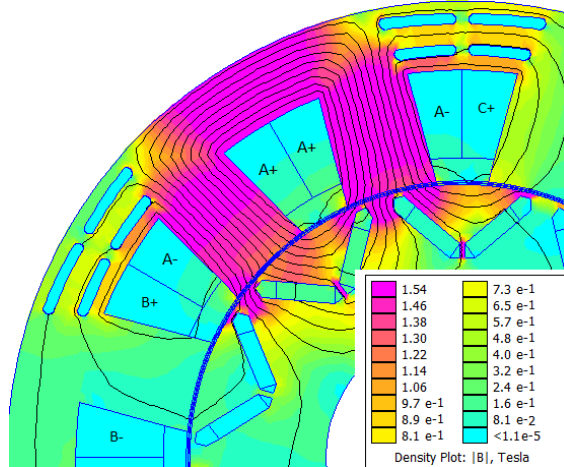
Figure 4. Winding disposition and connection. For this prototype machine, both parallel connection and Y connection is made outside the housing through six connection terminals.

2.2. Cooling channel size and electromagnetic effects

Introducing cooling channels in the stator back yoke by removing iron after the split ratio optimisation might affect the electromagnetic performance negatively by increasing the reluctance path for the rotor PM flux and/or the linked flux between stator coils. The Q12p10 machine features low mutual inductance between phases by linking the vast majority of the flux generated by phase windings in a loop contained within the two adjacent teeth belonging to the same phase group. This

Table 4. Results from FEA evaluation of cooling barrier size at 3000 rpm, 40 A/mm²

Barrier size (mm)	Average torque		Torque ripple pk2pk	
	(Nm)	(%)	(Nm)	(%)
1.0	162.13	0	16.484	0
2.0	162.12	-0.01	16.633	+0.90
3.0	161.91	-0.13	16.973	+2.97
4.0	160.65	-0.91	19.135	+16.1
5.0	157.37	-2.94	23.933	+45.2

**Figure 5.** FEA established magnetic flux generated by 100 A in phase A without any remanence in the magnets.

scenario is illustrated in Fig. 5 without any PM flux and 100 A in phase A. The reluctance change for coil self-linked flux due to cooling channels positioned between the coil groups belonging to the different phases, is believed to be negligible. In [30], a similar yoke barrier strategy is used to reduce the flux of sub-harmonics which exist in this winding layout, aimed to reduce both iron and PM losses in the Q12p10 machine. The solution in [30] evaluates yoke barriers situated between the teeth within a phase, which leads to a large reduction on torque for the machine type preferred in our paper.

To find out the performance implications of flux barrier between the phases, including the PM flux, a FEA parametric sweep is performed. The cooling channels thicknesses is swept from from 1 to 5 mm. As a reference, 2.0 mm is used in the final design shown in Fig. 5, and at 5 mm each, the two channels cover 77% of the 13 mm yoke thickness. Note that the shape of the channels and the choice of having four parallel channels instead of one is driven by flow split evaluation as explained in [26]. Average torque, torque ripple and iron losses are evaluated at rated speed, from zero up to to above rated current; 3000 rpm and 160 A (40 A/mm²). The results for the highest current, which has the most dramatic impact, are shown in Table 4. More than half (4 mm) of the yoke width can be cut out before 1% average torque loss is experienced. Torque ripple consequences are kept low at 3 mm or lower. Regarding iron losses, no monotonic or clear change is found for the different barrier thicknesses; increase of iron losses is less than 1% as a function of slot size. Using two 2 mm coolant barriers positioned between the phase groups is considered to have negligible impact on electromagnetic performance, and offer enough cross-section area for low-viscosity oil to flow without significant pressure drop. This type of utilization of part of the stator yoke to introduce cooling channels can be generalized for all the TCWMs with an even key winding factor, which represents the number of adjacent coils of the same phase [13].

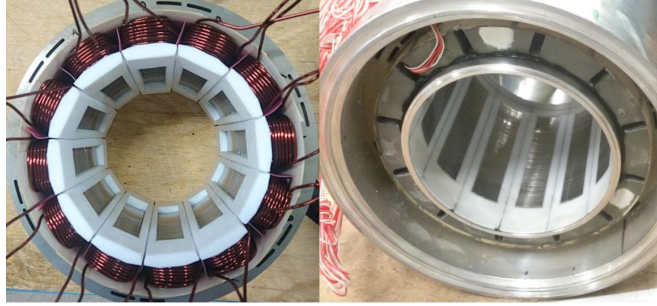


Figure 6. Wound stator before (left) and after (right) potting. The white plastics in the left picture is the bobbins used to pre-form the coils outside the machine.

2.3. Slot fill factor and cooling channels

The cooling channels are derived from the space in between the two coils, which is unused space in the slot. These are shaped in the epoxy material with Teflon sticks that are extracted after the potting process. The potting material is a epoxy resin, with a thermal conductivity of $1.9 \text{ W} / (\text{m} \cdot \text{K})$. The total slot area is 350 mm^2 . The cooling channel area in the slot is 100 mm^2 giving a net slot area of 250 mm^2 . The copper area is 113 mm^2 , therefore the net fill factor is 0.45 while the bulk fill factor considering the total slot area is 0.32. The stator with the windings mounted before and after potting is presented in Fig. 6. All thermal and cooling design considerations, including fluid dynamic analysis, for this machine are presented in [26].

3. Numerical evaluation

The electromagnetic performance of the machine, including loss mapping, is evaluated using FEA. The losses are used as input for evaluating the thermal performance and the efficiency.

Interior PM machines, when functioning as motors, are typically operated in the second quadrant of the d-q current plane. This is done in order to use both the PM flux generated torque, the reluctance torque and, at high speed operation, field weakening. The maximum negative d-axis current and positive q-axis current are evaluated analytically and used as references to map the operating region. For each point in the mapping, a set of 2D quasi-static magnetic FEA for one electric period is performed.

3.1. Loss Mapping

In order to evaluate PM and iron losses, the information stored on each simulation is the B field x and y component (B_x and B_y) of the stator and rotor iron mesh elements and the magnetic vector potential A , which in 2D FEA has only the z component, of the PMs mesh elements.

The iron losses are computed by performing the Discrete Fourier Transform (DFT) of B_x and B_y of stator and rotor iron elements. For each harmonic i and mesh element j

$$B_{fe,i,j}^2 = B_{x,i,j}^2 + B_{y,i,j}^2. \quad (1)$$

Iron losses are computed as the sum of all the contributions of the harmonics and all the m elements [25]

$$P_{fe,\omega} = K_m \sum_{j=1}^m \sum_{i=1}^{n/2} \frac{V_j}{k_s} \gamma_{fe} (k_e B_{fe,i,j}^2 f_i^2 + k_h B_{fe,i,j}^2 f_i) \quad (2)$$

where k_e and k_h are eddy current and hysteresis loss factors that can be extracted from the lamination data, γ_{fe} is the mass density of the iron, f_i is the electrical frequency corresponding to the i^{th} harmonic,

where the fundamental harmonic is the first harmonic present in the machine MMF for a certain speed ω . V_j is the volume of the mesh element j and k_s is the stacking factor. Furthermore, K_m is a iron loss scaling coefficient. This coefficient accounts, in the first place, for the effect of laser cutting of non-oriented electrical steel causing structural changes at the cutting edge, which finally affect the magnetic properties. Secondly, there is often a mismatch between the loss data found in the steel data sheets and the measured values.

Copper and iron losses are calibrated with the measured phase resistance, and by measuring the iron losses with the calorimetric set up described in Section IV, at 3000 rpm and no load. This results in an iron loss scaling coefficient K_m in eq. (2) of 2.0, meaning that the measured values of iron losses are twice the ones estimated with FEA using the interpolated loss coefficients from the soft iron manufacturer. Typical values of iron loss scaling coefficients found in the literature [22] are in the range between 1.5 and 2.0.

To calculate the PM losses, the DFT of the vector potential A of mesh elements belonging to the PMs is computed. The PM induced current density can be then calculated as

$$J_{PM} = -\frac{1}{\rho_{pm}} \frac{dA_{PM}}{d\theta} \omega + C(t) . \quad (3)$$

where $C(t)$ is an integration constant which forces the net total current flowing in each magnet to zero at any time instant and ρ_{pm} is the resistivity of the magnet material. The method is fully described in [33]. PM segmentation in the axial direction is accounted for by considering an equivalent eddy current resistance path. A flow chart summarizing the loss mapping procedure is shown in Fig. 7. The torque-speed maps showing the different loss contributions are presented in Appendix A.

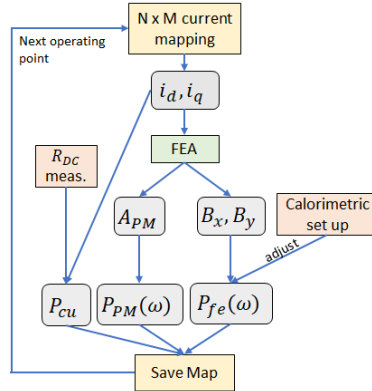


Figure 7. Loss mapping procedure flow chart

3.2. Inductance and linked PM flux

The d and q-axis inductance as a function of current are useful parameters for control purpose. The flux linkage of each phase and for all operating points is known from the FEA. Using the Clark and Park transformation the d-axis and q-axis flux linkage are derived. The PM flux linkage can be calculated at $i_d = 0$ as a function of the q-axis current as

$$\Psi_{pm}(i_q) = \Psi_d \Big|_{i_d=0} . \quad (4)$$

The d-axis and q-axis inductance can be computed as

$$L_d = \frac{\Psi_d - \Psi_{pm}}{i_d} \quad (5)$$

$$L_q = \frac{\Psi_q}{i_q}. \quad (6)$$

The inductance maps as a function of the d-axis and q-axis currents are presented in Fig. 8.

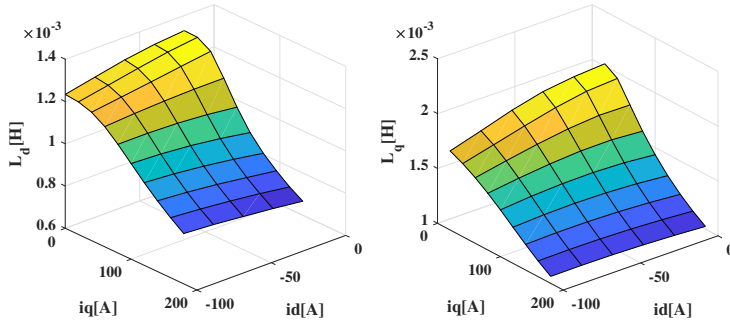


Figure 8. Inductance maps established through FEA.

3.3. Induced voltage

The induced phase voltage of the machine can be calculated from the derivative of the flux with respect to the angle, using approximation of derivatives by finite differences, as

$$V_{a,b,c} = \frac{\Delta \Psi_{a,b,c}}{\Delta \theta} \omega + R_{DC} i_{a,b,c}. \quad (7)$$

where $\Delta \Psi_{a,b,c}$ is the finite difference in flux linkage for a mechanical angle step of $\Delta \theta$, is the R_{DC} is the measured DC phase resistance, ω is the mechanical rotational speed and $i_{a,b,c}$ is the phase current.

3.4. Torque

The torque is computed through Arkkio's method [34], which essentially averages out all Maxwell stress tensor integration paths in a circular band in the air gap to improve the accuracy of torque computation by cancelling out some numerical noise due to the differentiation.

4. Test set up

In order to evaluate the performance of the assembled traction machine, a calorimetric set up is designed and constructed. The lab environment consists of a electric dynamometer, the test machine, power electronics, a custom made oil-to-water cooling system and a dSpace SCALEXIO-rack. The setup is illustrated in Fig. 9 and shown on photo in Fig. 10.

Sensors are installed and calibrated to measure DC and AC voltage (v), phase currents (i) output torque (τ), rotational speed (ω), rotational position (θ), oil and water flow-rates (\dot{m}), oil and water inlet and outlet temperatures (T) and pressures (p), water flows and pressures. Critical measurement equipment is listed in Tab. 5. The dSpace rack acts as the control hub of the dynamo setup. With the total setup, both electrical, mechanical and direct-loss power can be measured and displayed continuously and reference values can be set via a PC GUI. Oil and water temperatures are measured and converted to digital form with high resolution. The inlet-to-outlet temperature drop (ΔT) of the coolant oil is established. Together with the oil mass flow (\dot{m}), oil density ($\rho = 821 \text{ kg/m}^3$) and the

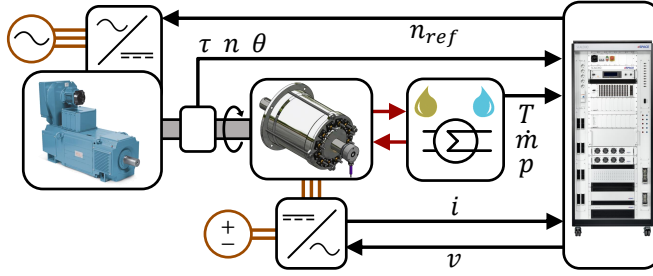


Figure 9. Calorimetric measurement system setup: A dSpace system is controlling the dynamo, the prototype machine, and the custom made oil-to-water cooling system.

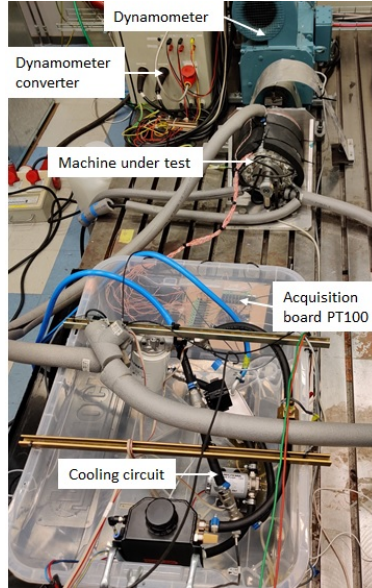


Figure 10. Picture of calorimetric test setup, showing the thermal insulation of the machine, oil hoses, and phase cables.

oil specific heat capacity ($c_p = 2100 \text{ J/kg/K}$) the total loss heat transported out of the machine can be calculated as

$$P_{cal} = \dot{m} \rho c_p \Delta T. \quad (8)$$

The test machine and the oil system is thermally insulated towards ambient in order to minimise thermal leakage and enable accurate calorimetric measurements. A glass fiber washer acts as a thermal insulator between the machine enclosure and the mounting frame. The coolant oil is heat exchanged with mass flow controlled tap water so that the inlet oil temperature to the machine is kept at 22°C , in order to minimize leakage heat from the surroundings.

A three-leg IGBT based inverter, operating at 5 kHz SVM closed-loop current control is feeding the test machine at up to $600 V_{DC}$. The dynamometer is operating at closed-loop speed control through a thyristor heat pump, feeding back power to the grid when the test machine is operating in motor mode.

Table 5. Critical measurement equipment

Quantity	Equipment
Torque	ETH DRBK-500-n
Speed, Position	Kübler 8.5020.2514.1500
Voltage	LeCroy HVD3206A
Current	LeCroy CP150
Power Analysis	LeCroy MDA805
Mass flow	Swissflow SF800

5. Results

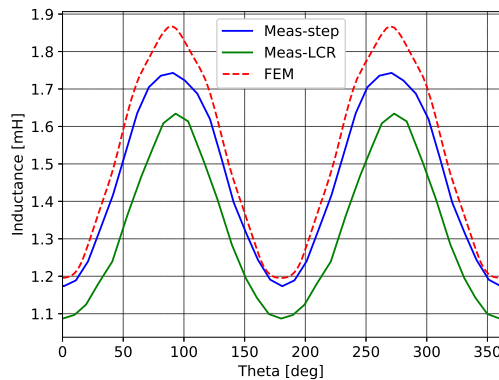
In this section the results from the measurements are presented and compared to the simulated values.

5.1. Machine parameters, back EMF and torque evaluation

The initial set of tests performed on the machine is to extract the main equivalent circuit model parameters. Firstly, the DC resistance of each coil is measured using a 4-terminal method resulting in a phase resistance of $62\text{ m}\Omega$. Secondly, the machine is connected with phase A in series with the parallel of phase B and C. The inductance seen with this type of connection needs to be scaled by $2/3$ to obtain the synchronous inductance. By moving the rotor in small mechanical angle steps and locking it, the inductance for each position can be measured using two methods:

- LCR tester at 1 kHz
- voltage step response from a fast power supply resulting in ca 19 A. The 20-80% rise time is extracted with an oscilloscope and re-scaled to a first order time constant

The results of the two measurement methods compared to the predicted FEA synchronous inductance as a function of the mechanical position are presented in Fig. 11. The maximum and minimum values of the curves in Fig. 11 represent the q-axis and d-axis inductance respectively. The machine presents a saliency $L_q/L_d = 1.45$ given by the V-shaped rotor geometry. Fig. 12 shows the no-load back-EMF at 1016 rpm, with both FEA and measurements.

**Figure 11.** Inductance versus electrical position by FEA and two different measurement methods

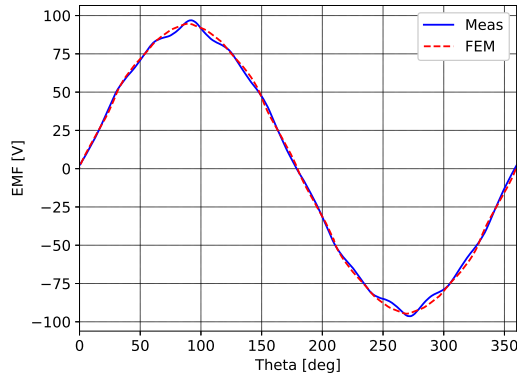


Figure 12. No-load back-EMF at 1016 rpm measured and simulated line-line voltage in Y-connection

245 The torque is measured, with the torque sensor, in two different operating conditions, pure
 246 q-axis current (90 deg) and the MTPA angle at maximum current (115 deg). The results at 150 rpm
 247 are presented in Fig 13. A current value of 100 A RMS corresponds to a copper current density
 248 of 25 A/mm² which can be kept continuously for this machine. If the machine would have been
 249 equipped with a standard water jacket cooling, a current density of 10 A/mm² is to be expected [7,24].
 250 Maintaining the same fill factor and removing the cooling channels, the slots could theoretically fit 40%
 251 more copper. Altogether, the maximum allowed continuous phase current would be 56 A (instead of
 252 100 A), and according to Fig. 13, the maximum output peak torque limited to 62 Nm instead of 110 Nm.
 253 Overall, by using direct oil cooling, the continuous power of the machine, for the same operating
 254 speed, increases by over 75%.

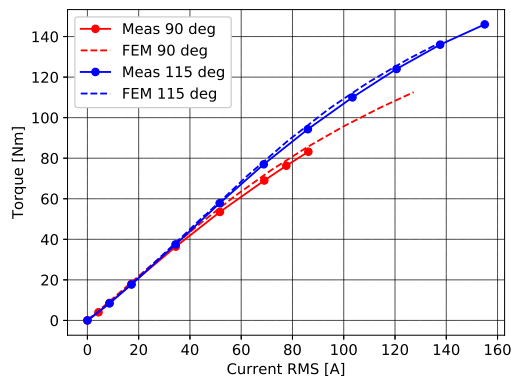


Figure 13. Average torque output at 150 rpm rotor speed, 90 and 115 deg current angle. Measurement and simulation comparison.

255 5.2. Calorimetric evaluation of efficiency

Electromagnetic efficiency through FEA, not including mechanical losses, is presented in in Fig. 14. The six operating points where the efficiency of the machine has been measured with the calorimetric

setup are marked with letters. The calorimetric method is presented in Eq. 8, and the measured efficiency is calculated using the total AC electrical active power P_{in} from the power analyser as:

$$\eta = \frac{P_{in} - P_{cal}}{P_{in}} . \quad (9)$$

The output mechanical power is defined as $P_{mech} = \omega \tau$. The measured efficiency are presented in Table. 6 and summarized in Fig. 16. The measured efficiency is within 0.9% of the simulated one. The difference between the two can be attributed to two main reasons.

- Mechanical losses, such as friction in the bearings and windage losses, which are not included in the FEA efficiency but are present in the measurements
- Leakage heat towards ambient air and through the shaft. Although, all possible precautions have been taken to minimize the heat leakage it is not possible to completely remove this source of error

The mechanical power can also be used to estimate the efficiency, however the accuracy of the torque sensor reading is lower compared to the input power reading and would lead to a higher uncertainty. Measurements above base speed are unfortunately not possible with the current dynamo setup.

In Fig. 15 the calorimetric run for point E is presented. It is of great importance to reach a thermal steady state in order to have an accurate calorimetric reading.

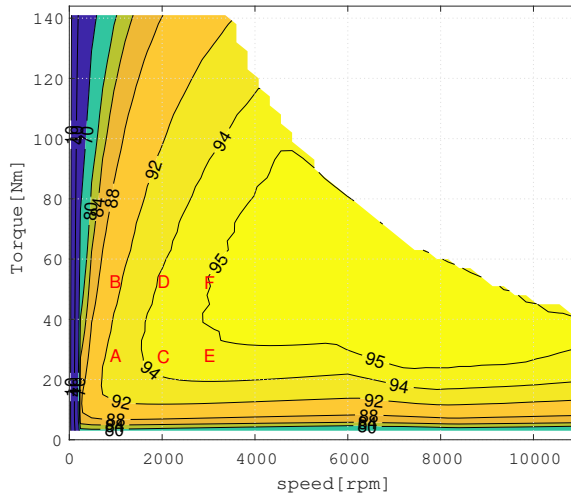


Figure 14. Efficiency map established with FEA while operating with a MTPA control strategy. Letters A-F represent the points verified with calorimetric measurements presented in Tab. 6.

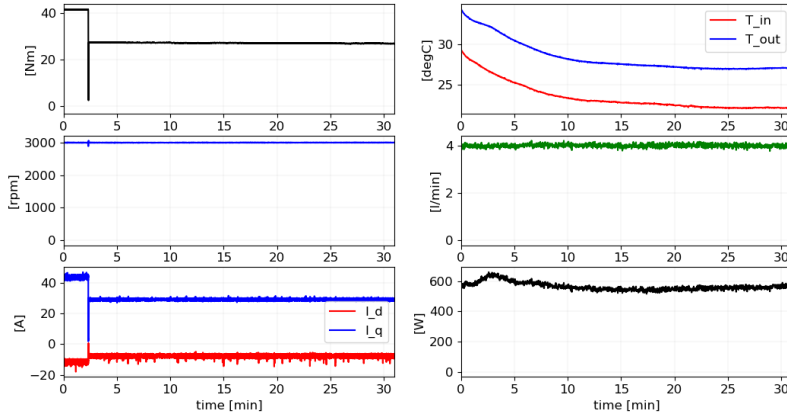


Figure 15. Calorimetric run at 3000 rpm and 30 A RMS. The plots are showing: top left output torque, top right oil inlet and outlet temperature, middle left mechanical speed, middle right oil flow rate, bottom left d-axis and q-axis currents, bottom right calorimetric loss

Table 6. Results from calorimetric measurements

Point	ω (rpm)	τ (Nm)	i (A RMS)	P_{mech} (kW)	P_{in} (kW)	P_{cal} (W)	η (%)	η_{FEA} (%)	$\eta_{FEA}-\eta$ (%)
A	1003	27.5	30.0	2.89	3.16	233	92.63	92.8	0.17
B	1005	56.0	60.0	5.89	6.65	660	90.07	90.8	0.73
C	1985	26.6	30.0	5.52	5.97	370	93.80	94.3	0.50
D	1990	56.6	60.0	11.78	12.65	860	93.20	94.0	0.80
E	3004	27.0	30.0	8.49	9.05	570	93.70	94.6	0.90
F	3007	57.0	60.0	17.96	18.74	785	94.66	94.9	0.24

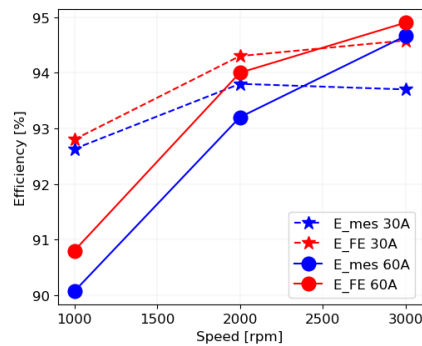


Figure 16. Measured and simulated efficiency comparison. E_{mes} is measured efficiency, E_{FE} is efficiency established with FEA.

269 6. Conclusion

270 This paper presents the design of a tooth coil winding PMSM machine for traction application,
 271 focusing on the electromagnetic design and performance verification. The solution adopted integrates

stator cooling, both thorough the slot and the stator yoke. The originality of the design consists on the integration of the cooling, using a thermally conductive epoxy resin to create the channels within the slot as well as the positioning of the stator yoke cooling channels. It is shown that for the Q12p10 machine, the electromagnetic performance is negligible affected by removing iron in the stator yoke for cooling channels if the position is carefully selected. The machine is designed such that it is possible to use a linear winding machine to pre-wind the coils on a bobbin, potentially leading to a reduced manufacturing cost for high volume production.

The adopted cooling solution enables a continuous copper current density of 25 A/mm². This allows for a 75% higher output torque and power density comparing with a corresponding water-jacket-cooled machine. Inductance, torque and no-load back EMF are measured and compared with FEA results, showing very good agreement. Furthermore, the efficiency of the machine is validated in one operating point, using a calorimetric direct-loss measurement set up, matching with FEA within 0.9 percent units. The peak efficiency according to FEA is a wide area above 95%, which is on par state-of-the-art automotive traction machines for higher power levels. The overall net power density (19 kW/l) is comparable with the current state-of-the-art traction machines on the market, even with higher power ratings, despite this machine being an early prototype. Further design improvements towards series production is likely to bring also the gross power density to very appealing levels by minimizing the volumetric overhead of coolant interfaces and connection terminals.

Author Contributions: Conceptualization, A.A.; methodology, A.A. and S.S.; software, A.A. and S.S.; validation, A.A. and S.S.; formal analysis, A.A. and S.S.; investigation, A.A. and S.S.; resources, A.A. and S.S.; data curation, A.A. and S.S.; writing—original draft preparation, A.A. and S.S.; writing—review and editing, A.A., S.S. and E.G.; visualization, A.A. and S.S.; supervision, E.G. and T.T.; project administration, T.T.; funding acquisition, T.T. All authors have read and agreed to the published version of the manuscript.

Acknowledgments: The authors gratefully acknowledge the financial support from the Swedish Energy Agency and the Swedish Governmental Agency for Innovation Systems (VINNOVA).

Abbreviations

The following abbreviations are used in this manuscript:

PMSM	Permanent magnet synchronous machine
HTC	Heat transfer coefficient
FEA	Finite element analysis
TCWM	Tooth coil winding machine
DW	Distributed winding
MMF	Magneto-motive force
FW	Field weakening
SVM	Space vector modulation

Appendix A

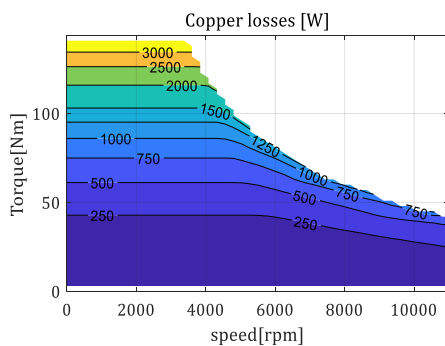


Figure A1. Copper loss map from FEA.

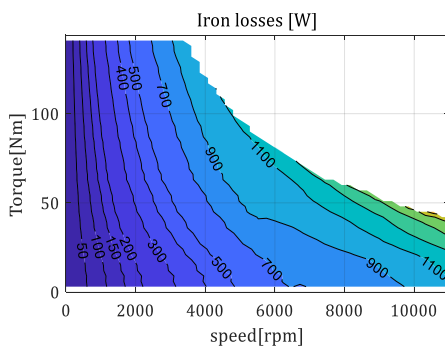


Figure A2. Iron loss map from FEA.

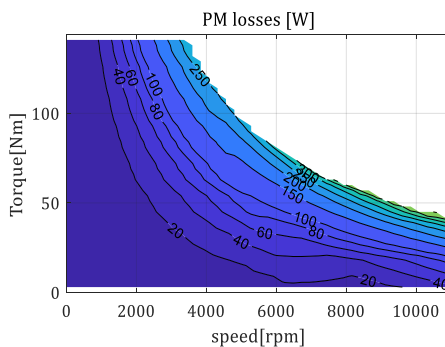


Figure A3. PM loss map from FEA.

References

1. Chau, K.T.; Chan, C.C.; Liu, C. Overview of Permanent-Magnet Brushless Drives for Electric and Hybrid Electric Vehicles. *IEEE Trans. on Industrial Electronics* **2008**, *55*, 2246–2257.

2. Electrical, U.D. Electronics Technical Team Roadmap. Technical report, 2017.
3. Chowdhury, S.; Gurpinar, E.; Su, G.J.; Raminosoa, T.; Burress, T.A.; Ozpineci, B. Enabling Technologies for Compact Integrated Electric Drives for Automotive Traction Applications. 2019 IEEE Transportation Electrification Conference and Expo (ITEC). IEEE, 2019, pp. 1–8.
4. Zhang, X.; Haran, K.S. High-specific-power electric machines for electrified transportation applications-technology options. 2016 IEEE Energy Conversion Congress and Exposition (ECCE). IEEE, 2016, pp. 1–8.
5. Ramesh, P.; Lenin, N. High Power Density Electrical Machines for Electric Vehicles—Comprehensive Review Based on Material Technology. *IEEE Transactions on Magnetics* **2019**, *55*, 1–21.
6. Grunditz, E.A.; Thiringer, T. Performance Analysis of Current BEVs Based on a Comprehensive Review of Specifications. *IEEE Transactions on Transportation Electrification* **2016**, *2*, 270–289.
7. Pyrhönen, J.; Jokinen, T.; Hrabovcova, V. *Design of rotating electrical machines*; John Wiley & Sons, 2009.
8. Hendershot, J.R.; Miller, T.J.E. *Design of brushless permanent-magnet machines*; Motor Design Books, 2010.
9. Carriero, A.; Locatelli, M.; Ramakrishnan, K.; Mastinu, G.; Gobbi, M. A Review of the State of the Art of Electric Traction Motors Cooling Techniques. *SAE Technical Paper* **2018**, 2018-01-0057.
10. Popescu, M.; Staton, D.A.; Aldo, B.; Andrea, C.; Douglas, H.; James, G. Modern Heat Extraction Systems for Power Traction Machines. *IEEE Transactions on Industry Appl.* **2016**, *52*, 2167–2175.
11. Gai, Y.; Kimiabeigi, M.; Chuan Chong, Y.; Widmer, J.D.; Deng, X.; Popescu, M.; Goss, J.; Staton, D.A.; Steven, A. Cooling of Automotive Traction Motors: Schemes, Examples, and Computation Methods. *IEEE Transactions on Industrial Electronics* **2019**, *66*, 1681–1692.
12. El-Refaie, A.M. Fractional-slot concentrated-windings synchronous permanent magnet machines: Opportunities and challenges. *IEEE Trans. on industrial Electronics* **2010**, *57*, 107–121.
13. Skoog, S.; Acquaviva, A. Pole-Slot Selection Considerations for Double Layer Three-phase Tooth-Coil Wound Electrical Machines. ICEM '18, Alexandroupoli, 2018.
14. Libert, F.; Soulard, J. Investigation on pole-slot combinations for permanent-magnet machines with concentrated windings. Int. Conference on Electrical Machines (ICEM), 2004, pp. 5–8.
15. Yang, Z.; Shang, F.; Brown, I.P.; Krishnamurthy, M. Comparative Study of Interior Permanent Magnet, Induction, and Switched Reluctance Motor Drives for EV and HEV Applications. *IEEE Transactions on Transportation Electrification* **2015**, *1*, 245–254.
16. Reddy, P.B.; El-Refaie, A.M.; Huh, K.K.; Tangudu, J.K.; Jahns, T.M. Comparison of interior and surface PM machines equipped with fractional-slot concentrated windings for hybrid traction applications. *IEEE Transactions on Energy Conversion* **2012**, *27*, 593–602.
17. Lindh, P.; Montonen, J.; Immonen, P.; Tapia, J.A.; Pyrhönen, J. Design of a traction motor with tooth-coil windings and embedded magnets. *IEEE Transactions on Industrial Electronics* **2013**, *61*, 4306–4314.
18. Dubar, C. Design and analysis of a fault-tolerant fractional slot PMSM for a vehicle application. PhD thesis, Chalmers University of Technology, 2016.
19. Wang, J.; Yuan, X.; Atallah, K. Design optimization of a surface-mounted permanent-magnet motor with concentrated windings for electric vehicle applications. *IEEE Transactions on Vehicular Technology* **2012**, *62*, 1053–1064.
20. Zhang, H. On electric machinery for integrated motor drives in automotive applications. PhD thesis, KTH Royal Institute of Technology, 2017.
21. Ibrahim, M.N.F.; Sergeant, P. Prediction of Eddy Current Losses in Cooling Tubes of Direct Cooled Windings in Electric Machines. *Mathematics* **2019**, *7*, 1096.
22. Ponomarev, P.; Polikarpova, M.; Pyrhönen, J. Thermal modeling of directly-oil-cooled permanent magnet synchronous machine. 2012 XXth International Conference on Electrical Machines. IEEE, 2012, pp. 1882–1887.
23. Lindh, P.; Petrov, I.; Pyrhönen, J.; Scherman, E.; Niemelä, M.; Immonen, P. Direct Liquid Cooling Method verified with a Permanent-Magnet Traction Motor in a Bus. *IEEE Transactions on Industry Applications* **2019**, *55*, 4183–4191.
24. Liu, Z.; Winter, T.; Schier, M. Direct coil cooling of a high performance switched reluctance machine (SRM) for EV/HEV applications. *SAE International Journal of Alternative Powertrains* **2015**, *4*, 162–169.

25. Acquaviva, A.; Grunditz, E.A.; Lundmark, S.; Thiringer, T. Comparison of MTPA and Minimum Loss Control for Tooth Coil Winding PMSM Considering PM and Inverter Losses. 2019 21st European Conference on Power Electronics and Applications (EPE '19 ECCE Europe), 2019.
26. Acquaviva, A.; Skoog, S.; Thiringer, T. Design and Verification of In-slot Oil-Cooled Tooth Coil Winding PM Machine for Traction Application. *IEEE Transactions on Industrial Electronics* **2020**, pp. 1–1.
27. Burrell, T.A.; Campbell, S.L.; Coomer, C.; Ayers, C.W.; Wereszczak, A.A.; Cunningham, J.P.; Marlino, L.D.; Seiber, L.E.; Lin, H.T. Evaluation of the 2010 Toyota Prius hybrid synergy drive system. Technical report, Oak Ridge National Lab.(ORNL), 2011.
28. Ozpineci, B. Annual Progress Report for the Electric Drive Technologies Program. *Oak Ridge National Laboratory, Tech. Rep* **2016**.
29. Acquaviva, A. Analytical Electromagnetic Sizing of Inner Rotor Brushless PM Machines Based on Split Ratio Optimization. ICEM '18, Alexandroupoli, 2018.
30. Dajaku, G.; Xie, W.; Gerling, D. Reduction of Low Space Harmonics for the Fractional Slot Concentrated Windings Using a Novel Stator Design. *IEEE Transactions on Magnetics* **2014**, 50.
31. Aslan, B.; Semail, E.; Korecki, J.; Legranger, J. Slot/pole combinations choice for concentrated multiphase machines dedicated to mild-hybrid applications. IECON 2011-37th Annual Conference of the IEEE Industrial Electronics Society. IEEE, 2011, pp. 3698–3703.
32. Yamazaki, K.; Fukushima, Y. Effect of eddy-current loss reduction by magnet segmentation in synchronous motors with concentrated windings. *IEEE Transactions on Industry Applications* **2011**, 47, 779–788.
33. Ishak, D.; Zhu, Z.Q.; Howe, D. Eddy-current loss in the rotor magnets of permanent-magnet brushless machines having a fractional number of slots per pole. *IEEE Transactions on Magnetics* **2005**, 61, 2462–2469.
34. Arkkio, A. Analysis of induction motors based on the numerical solution of the magnetic field and circuit equations. PhD thesis, Helsinki University of Technology, 1987.

Paper VIII

Manufacturing of in-slot cooled tooth coil winding PM machines

Submitted to ICEM2020
Conference date: 2020-08-23 in Gothenburg, Sweden

First author contributions

Paper structure, lead machine design FEA, thermal and mechanical,
corresponding author, manufacturing support.

Second author contributions

Idea development, verification of machine design with FEA,
48 V machine responsible, picture generation,
manufacturing support.

Manufacturing of cooled tooth coil winding PM machines with in-slot oil cooling

Alessandro Acquaviva, *Student Member, IEEE*, Stefan Skoog, *Student Member, IEEE*, and Torbjörn Thiringer, *Senior Member, IEEE*

Abstract—This paper presents a description of the manufacturing challenges and solutions of two 50 kW radial flux inner-rotor tooth coil winding PM machines with in-slot cooling for vehicle application. The two machines are designed for different DC link voltages, 600 V and 48 V. The machines are designed to achieve high efficiency and high power density. To enable this, liquid cooling is necessary. In the solution presented, the oil coolant is pushed through the stator yoke and in the slots with the intent of removing the heat close to the loss generation. The cooling channels in the slots are built during the stator potting process using a high thermally conductive potting material. The stator is designed to be compatible with automated manufacturing for high volume production. The machines presented in this paper are designed for high speed operation and capable to withstand current densities of 25 A/mm² in continuous operation and 35 A/mm² for 30 s peaks, at 6 l/min oil flow and an inlet temperature of 20°C.

Index Terms—Brushless PM machines, Cooling, Electric Vehicles

I. INTRODUCTION

Tooth coil winding machines (TCWM) are widely used for mass produced low power industrial applications because of the low cost manufacturing process and good copper fill factor. These are becoming attractive also for traction applications [1], [2]. The cost saving comes mainly from the simple winding structure, which typically allows to use high speed winding machines, such as linear winding machines (also known as spindle winding machines), based on bobbin rotation and the wire is layered onto the bobbin.

Traction electric drives are designed for high power density, high efficiency and reliability. In order to achieve this an effective cooling system for the electrical machine is needed, typically a closed loop forced liquid cooling. Several different forced cooling solutions found in industry can be categorized as [3], [4]:

- Cooling jacket (oil or water)
- Hollow shaft (oil or water)
- In-slot cooling (oil or water)

The authors gratefully acknowledge the financial support from the Swedish Energy Agency and the Swedish Governmental Agency for Innovation Systems (VINNOVA).

A. Acquaviva, S. Skoog and T. Thiringer are with the Division of Electric Power Engineering at Chalmers University of Technology, Gothenburg, Sweden (e-mail: alessandro.acquaviva@chalmers.se, stefan.skoog@chalmers.se, torbjorn.thiringer@chalmers.se).

- Fluid bath (oil)
- Fluid spray (oil)

Some of these can be combined on the same machine.

Depending on the solution in use there are different options when it comes to the coolant fluid, as shown in [4]. However, most solutions use either oil or water (typically mixed with glycol). The specific heat of water or water/glycol is about twice that of oil, so a given flow rate of water absorbs more heat per degree increase in temperature than the same flow rate of oil. The coolant chosen in the solution adopted is oil, this because oil is a good electrical insulator, thus it can be in direct contact with the conductors. In the machines presented in this paper the coils are not in direct contact with the oil, but some fluid might penetrate through the potting material. Additionally there is a direct contact in the end section, where the connections between adjacent coils and the coil terminals are brought out of the machine. Also, an oil leak from the cooling channel through the airgap would not cause any hazard. If water should similarly leak, substantial machine damage might occur, such as PM corrosion and steel oxidation. Oil, is already often present as a lubricant in the transmission and naturally helps to prevent corrosion, which can be beneficial for the system compactness.

In-slot cooling is an efficient way of removing the heat very close to the main source. Tooth coil winding, in particular the double layer configuration, present opportunities of direct winding cooling. Firstly, the end winding is not overlapping, meaning an easy access to the slot from the end section. Secondly, typically it is convenient to have wound with a winding machine either by segmenting the stator or by designing the stator without tooth tip to insert the pre-formed coil. During this process often some space is left between the two coils, this can be used for the cooling, see Fig 2.

In [5] a tooth coil winding machine concept using in-slot cooling is presented. This solution uses water-soluble mould cores in the space in the slot not filled with copper to create cooling channels, a concept that is hard to adopt for mass production. Directly cooled axial flux PMSM, using Litz wire with a tube for liquid inside each turn, can also be found in the literature [6]. This solution requires custom-made Litz wires which can be costly, complicated to wind during manufacturing and yet a maximum feasible current density of 14 A/mm² is reported. A different concept is presented in [7], where a direct winding copper heat

exchanger is placed in between the each of the coils of a double layer tooth coil wound machine. This solution allows a direct, in-slot water-cooling of the windings without exposing the winding copper wires to water. Current densities of 25 A/mm^2 continuous and 40 A/mm^2 peak operation are reported with this solution. The copper heat exchangers in the slot add complexity when it comes to slot insulation and manufacturing. Furthermore, a complete machine in hardware validating the cooling concept is not presented.

In-slot cooling for a SRM is presented in [8], [9] showing how the cooling performance is improved compared to water mantle cooling. The concept, tested DC current up to 22 A/mm^2 , comes with some challenges regarding coolant leakage to the rotor.

The machine presented in this paper has been built, tested and validated up to the maximum torque. The cooling concept, using a high thermally conductive potting material to create the slot cooling channels and the placement of the stator yoke cooling channels, has not been found in the literature. The design process and test results are described and presented in [10], [11]. Both thermal and electromagnetic experimental verification was carried out up to the peak torque of 145 Nm, showing that the machine can withstand 25 A/mm^2 for continuous operation and 35 A/mm^2 for 30 seconds with an oil flow rate of 6 l/min. The focus of this paper is to show how the solution adopted has been manufactured, presenting the main issues and how these have been solved. Furthermore, an analysis of how the manufacturing of such solution could be made for mass production is presented.

II. PROPOSED SOLUTION

The electrical machine in this paper is designed as traction motor for a small passenger vehicle, a two seater car with a curb weight of 800 kg. The resulting machine design specifications are presented in Table I.

TABLE I: Electrical machine design specifications

Quantity	Value	Unit
Peak torque	140	Nm
Peak power	50	kW
Base speed	3 600	rpm
Max speed	11 000	rpm
Coolant max temperature	60	$^{\circ}\text{C}$
Max winding temperature	180	$^{\circ}\text{C}$
DC bus voltage	600/48	V

The machine is sized using an analytical sizing process, described in [12] and verified with FEA. The main geometrical dimensions, outcome of the sizing, are presented in Table II and the details of the winding.

The coil disposition and geometries of stator and rotor as well as the cooling channel disposition are shown in Fig. 1.

The slot cooling channels are derived from unused space in-between the coils. The total slot area, A_{slot} , is 350 mm^2 . The cooling channel area, A_{cool} , for a single slot is 100 mm^2 which gives a net slot area of 250 mm^2 . The bulk fill factor is defined as

TABLE II: Main dimensions and data for both 600 V and 48 V machines

Quantity	Value	Unit
Outer Stator diameter	180	mm
Inner Stator diameter	111.4	mm
Active length	100	mm
Tooth width	17	mm
Stator Yoke width	13	mm
Magnet thickness	3.5	mm

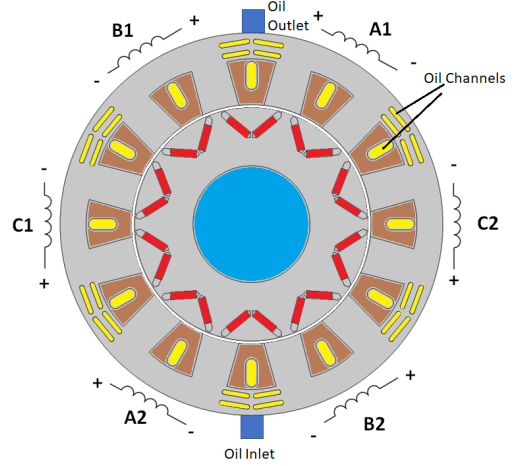


Fig. 1: Stator and rotor laminations geometry, coil disposition and cooling channels (in yellow).

$$k_{fill,bulk} = \frac{A_{cu}}{A_{slot}} \quad (1)$$

and the net fill factor as

$$k_{fill,net} = \frac{A_{cu}}{A_{slot} - A_{cool}} \quad (2)$$

where A_{cu} is the copper area, which differs for the two motors:

- the 600 V machine has 56 (2x28) conductors with a diameter of 1.6 mm in each slot. Resulting in a total copper area of 113 mm^2 , yielding a net fill factor of 0.45, while considering the total slot area yields a bulk fill factor of 0.32.
- the 48 V machine has 54 (2x3x9) conductors with a diameter of 1.5 mm in each slot. Resulting in a total copper area of 95.5 mm^2 , yielding a net fill factor of 0.38, while considering the total slot area yields a bulk fill factor of 0.27.

Figure 2 shows the slot and the conductor disposition for the two machines.

Another feature of the 12 slot 10 pole machine, is that it presents the opportunity of inserting cooling channels also in the stator yoke as described and analyzed in [11] and

TABLE III: Winding design for the two machines

Quantity	48 V Mach.	600 V Mach.	Unit
Diameter of each conductor	1.5	1.6	mm
N. parallel conductors per turn	9	1	-
N. turns per coil	3	28	-
Max. RMS current	1200	140	A

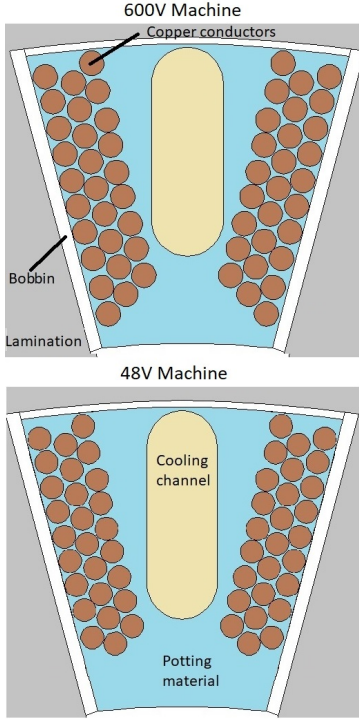


Fig. 2: Slot design: upper 600 V machine with 28 turns, lower 48 V machine with 3 turns of 9 parallel conductors

presented in Fig. 1. This allows to directly cool the stator iron, which can have a significant amount of losses at high speed operation. A fluid flow analysis and distribution is presented in [10].

The machine is designed for high power density but the main target is high efficiency. In [12] it is shown that by writing the machine torque equation as a function of the split ratio, inner to outer stator diameter ratio, there is a trade off between efficiency and power/torque density. Efficiency was privileged and has been evaluated in [11] and shown in Fig. 3. The net power density is 19 kW/l and is comparable with other traction motors found in industry [11].

III. MANUFACTURING

In this section the manufacturing of the prototypes is discussed and described, analysing also the potential for mass

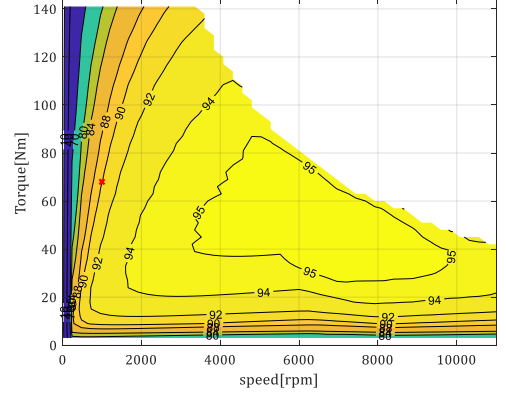


Fig. 3: Efficiency map established with FEA while operating with a MTPA control strategy. In red one of the points where the efficiency has been measured experimentally.

manufacturing. A flow chart showing the main steps of the stator manufacturing process is presented in Fig 4.

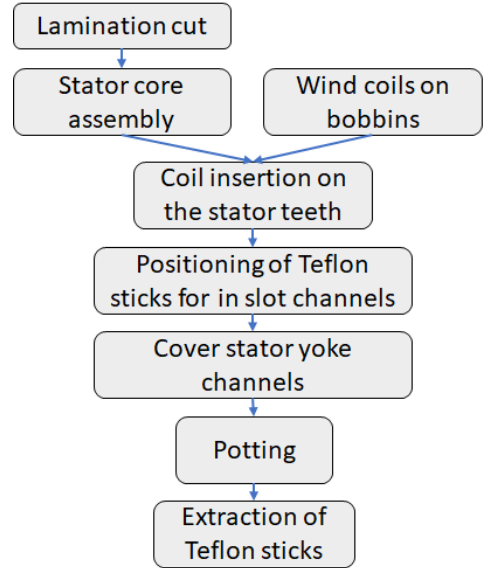


Fig. 4: Flow chart of the stator manufacturing process. End section barriers are placed after inserting the stator in the frame and not shown here.

A side view and cross section of the machine is presented in 5.

The prototypes have been built using single Polytetrafluoroethylene (PTFE) sticks for each slot as shown in Fig. 6. PTFE is used for the cooling channels former because of the

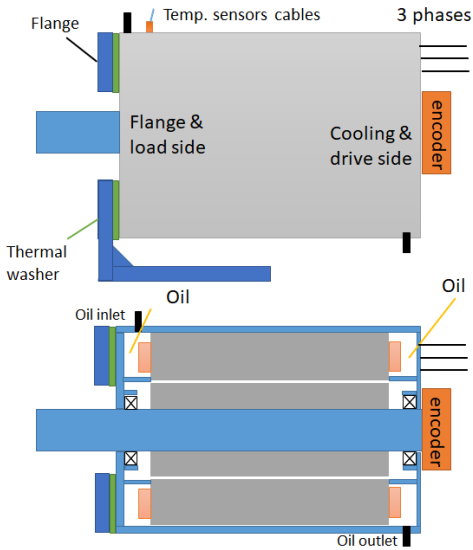


Fig. 5: Side and cross section view of the machine and support

remarkable nonstick properties. In fact the material is self-lubricated which allows to extract the channel former sticks once the potting is cured without damaging the stator. For series production, it is possible to have a PTFE ring with all the sticks inserted at once, shown in Fig. 7. In order to make the extraction process of all the sticks at the same time possible, these need to have a well defined draft angle; a cross section which is slightly gradually reducing, wider at the point of connection to the ring and thinner at the other end. The difference between the two ends of the cooling channel former needs to be very small to limit the effect of the non-constant cross section on the fluid dynamics. The 600 V machine stator before and after the potting and extraction process is presented in Fig. 8.

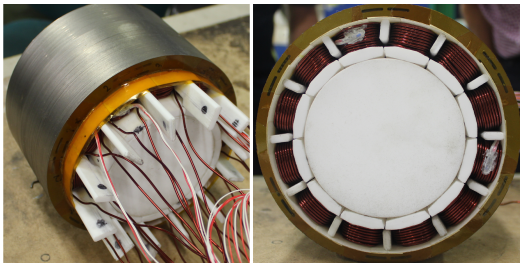


Fig. 6: Insertion of PTFE barriers before potting process. Left non-drive end and right drive end.

The coils for the two machine prototypes are hand wound

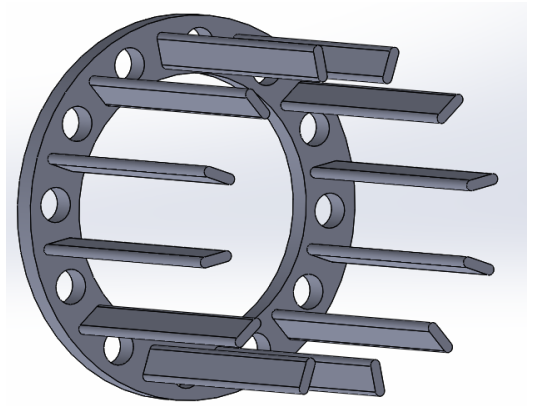


Fig. 7: PTFE ring with channel former sticks for automated manufacturing of slot cooling channels

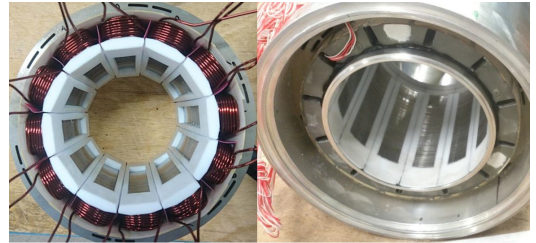


Fig. 8: 600 V machine before potting and frame mounting (non-drive end) of the left and after potting and mounting the frame on the right (non-drive end).

using a steel coil former as a support for the bobbin, shown in Fig. 9. These avoid the collapse of the PTFE bobbin during the winding when a significant pull to the wire is applied. The coil former with the wound bobbin is placed in front of the tooth and then pushed radially in the stator. In a high volume production process this could be automatized with a more detailed analysis of the tolerances needed in the process. Furthermore, the bobbins, which are now made by water cutting, can easily be molded for high volume production.

The 12 slot 10 pole machine presents four coils for each phase [13], the coils of the same phase are paired around the stator core, as shown in Fig.10. The two adjacent coils of the same phase cannot be parallel connected because the induced voltages are not in phase [13] but need to be series connected. The coils can be wound in pairs of two, without interrupting the conductor, and inserted. This avoids one connection point which is usually a costly and complex process during manufacturing. Also, the parallel connection of the two pairs of parallel coils as well as the star connection can be made internally, this guarantees additional cooling on the point of connection which can be otherwise a critical

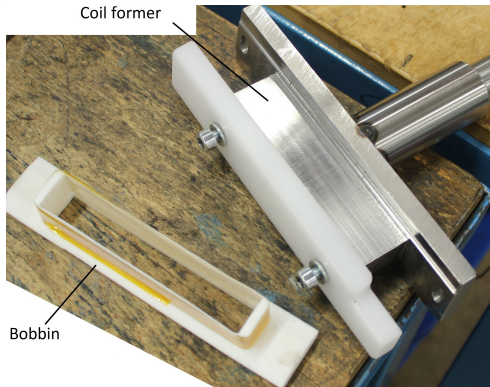


Fig. 9: Bobbin and coil former for manual winding

hot-spot.

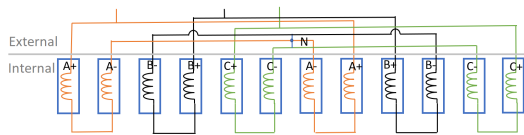


Fig. 10: Diagram showing the disposition and connection of the coils. For the prototypes 12 terminals are coming out of the frame and the star and parallel connections are made externally. For mass manufacturing all this can be done internally having externally only 3 connection terminals.

The series connected adjacent coils are soldered and bundled, the connection point is immersed in oil during normal operation. Pictures showing the connection points and terminations of the two machines are presented in Fig. 11 and Fig. 12.

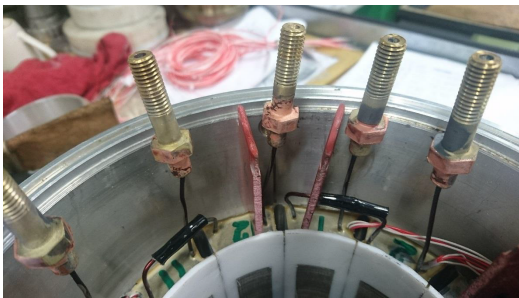


Fig. 11: Detail of adjacent coil connection for 600 V machine

Fiber glass flow stoppers are installed in the end section to redirect the coolant flux in two parallel paths. The end section is shown in Fig. 13. The temperature sensors installed in the mid-axial position of the machine are routed through



Fig. 12: Stator of 48 V machine after potting and after connection of adjacent coils

the cooling channel. This type of installation is quite invasive when it comes to flow distribution, however in an industrial product these are typically not necessary.

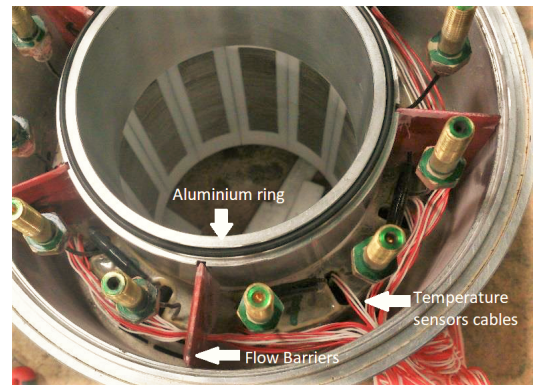


Fig. 13: End section barriers to redirect flow

The end winding section, which is basically immersed in oil, needs to be sealed with respect to the airgap. This is done by using o-rings at the ends of the frame as shown in Fig. 13.

A big issue during manufacturing has been to seal of leakage from oil cooling channels to the rotor area. In fact leakage was detected via the stator sheets by performing a pressure test with air at 1.5 bar. There is a rather short distance via the steel sheets from the cooling channels to the surrounding areas. Obviously, the back lack glue was not sufficient and the molding material has not penetrated enough

into any voids. Finally, for the prototypes the leakages has been resolved by using a penetrating glue, Loctite 420.

A degree of leakage to the rotor is anyway accepted, in fact the end section presents a rotor leakage outlet, shown in Fig. 14.

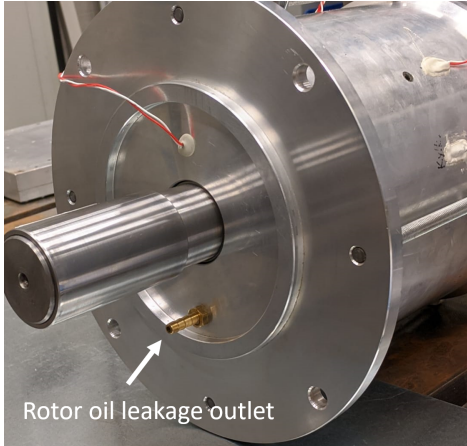


Fig. 14: Rotor leakage outlet

A list of the materials used to manufacture the different parts is presented in Table IV

TABLE IV: Used materials

Part	Material
Stator and rotor Lamination	M235-35 Backlack
Frame	Aluminum A356 Temper
Magnets	NdFeB Vacodum 745 DHR
Potting stator	Lord CoolTherm EP-2000
Potting rotor	Elantas Elatron MC4260
Bobbin	PTFE
Leakage sealing	Penetrating glue Loctite 420
Cooling channel former	PTFE
End section barriers	Fiberglass

The coolant oil used is provided by ExxonMobil and specifically developed for electrical machine cooling, featuring low viscosity and good thermal properties as shown in Table V. However, any low viscosity oil could potentially be used if compatible with the materials used.

TABLE V: Oil coolant properties (data from ExxonMobil).

	40 °C	80 °C	100 °C
Kinematic viscosity (cSt)	2.31	1.28	1.02
Specific heat (J/kgK)	2.15	2.28	2.35

IV. DESIGN IMPROVEMENTS

The main issue found during testing is an oil leakage of about 1% of the total volumetric flow towards airgap and the rotor oil drainage worked as expected. The leakage

started after testing the machine at high temperature. The thermal expansion during the testing has probably caused some openings of the sealing of the inner part of the stator and the oil leaks radially through the lamination sheets. This leakage, if controlled, could be beneficial for rotor cooling. A possible solution to avoid this leakage completely is to install a non conductive thin cylindrical sheet in the airgap or a special coating of the inner stator. This, however, could cause an increase in the airgap length needed for mechanical tolerance.

The margins taken because of the hand-winding process and the sub-optimal bobbins used during prototyping led to a copper conductor of 1.6 mm and 1.5 mm in diameter respectively for the 600 V and 48 V machine. However, with a winding machine and an optimized bobbin design for series production a copper conductor of 1.8 mm is feasible, which would result in a net fill factor of 0.57 (600 V machine, 28 turns) and 0.55 (48 V machine, 3 turns with 9 conductors per turn).

Regarding the terminations and end sections these have been built keeping big margins. The flow stoppers can be integrated in the end-cap, avoiding single insertion. There is significant room to reduce the space in the end section, thus reducing the total volume and in turn to further improve the power density.

The external frame is used just for mechanical support and can be made thinner than the one built for the prototypes. This would allow to further improve the weight and gross power density. A summary of the suggested design improvements for mass production is presented in Table VI.

TABLE VI: Design Improvements

	Prototype	Mass production
Star connection	External	Internal
Parallel coil connection	External	Internal
Adjacent coil connection	Soldered	No interruption
Coil former	Single	Multi-former tool
Bobbins	Water cut	Molded
Winding	Manual	Linear winding machine
Temperature sensors	Yes	No
Wire diameter	1.6 mm-1.5 mm	1.8 mm
End-section barriers	Single parts	Integrated in end-cap

V. CONCLUSIONS

In this paper the design and manufacturing steps of two 50 kW in-slot cooled tooth coil winding machine prototypes has been discussed and analyzed. The machines are meant for traction application and are designed to achieve high efficiency and high power density. This is done by designing the machine for high speed operation and capable to withstand current densities of 25 A/mm² in continuous operation and 35 A/mm² for 30 s. To enable this, cooling channels are created in the slot using a high thermally conductive epoxy resin. Additionally, the oil can flow through the stator iron and in the end sections. The process to create the cooling channels within the slot is potentially an interesting solution for industry and the overall machine design can be improved and engineered to be compatible with mass manufacturing.

A. Acknowledgements

Sincere gratitude to Bevi AB for sharing valuable experience on manufacturing challenges and assembling the machine prototypes.

VI. BIOGRAPHIES



Alessandro Acquaviva received a double M.Sc at Politecnico di Torino and KTH, Stockholm, Sweden in 2012. After four years in traction electrification industry and completing an MBA he is currently pursuing his Ph.D. at Chalmers University of technology in Gothenburg, Sweden. His areas of interest include the modeling, control and design of electrical machines and power electronics with focus on automotive applications.



Stefan Skoog was born 1985, graduated as M.Sc.E.E from Lund University, Sweden in 2010. Stefan has a decade of professional experience in R&D in advanced mechatronics and automotive powertrains. He is currently a PhD student at Chalmers University, Sweden, working on mild hybrid electrification systems limited to 48 VDC aimed for personal vehicles. His interests include modeling, design and verification of advanced battery systems, power electronics and electric machines.



Torbjörn Thiringer works at Chalmers university of Technology, in Gothenburg, Sweden, as a professor in applied power electronics. He took his M.Sc and Ph.D at Chalmers University of technology in 1989 and 1996 respectively. His areas of interest include the modeling, control and grid integration of wind energy converters into power grids as well as power electronics and drives for other types of applications, such as electrified vehicles, buildings and industrial applications.

REFERENCES

- [1] A. M. El-Refai, "Fractional-slot concentrated-windings synchronous permanent magnet machines: Opportunities and challenges," *IEEE Trans. on industrial Electronics*, vol. 57, no. 1, pp. 107–121, 2010.
- [2] N. Bianchi, M. Dai Pre, L. Alberti, and E. Fornasiero, *Thory and Design of Fractional-Slot PM Machines*. Cleup, 2007.
- [3] C. Alberto, L. Matteo, R. Kesavan, M. Gianpiero, and G. Massimiliano, "A review of the state of the art of electric traction motors cooling techniques," *SAE Technical Paper*, vol. 2018-01-0057, 2018.
- [4] M. Popescu, D. A. Staton, B. Aldo, C. Andrea, H. Douglas, and G. James, "Modern heat extraction systems for power traction machines," *IEEE Transactions on Industry Appl.*, vol. 52, no. 3, pp. 2167–2175, 2016.
- [5] M. Schiefer and M. Doppelbauer, "Indirect slot cooling for high-power-density machines with concentrated winding," in *IEMDC '15*, 2015, pp. 2167–2175.
- [6] P. Lindh, I. Petrov, A. Jaatinen-Väri, A. Grönman, M. Martinez-Iturralde, M. Satrustegui, and J. Pyrhönen, "Direct liquid cooling method verified with an axial-flux permanent-magnet traction machine prototype," *IEEE Transactions on Industrial Electronics*, vol. 64, no. 8, pp. 6086–6095, Aug 2017.
- [7] S. A. Semidey and J. R. Mayor, "Experimentation of an electric machine technology demonstrator incorporating direct winding heat exchangers," *IEEE Transactions on Industrial Electronics*, vol. 61, no. 10, pp. 5771–5778, Oct 2014.
- [8] Z. Liu, T. Winter, and M. Schier, "Direct coil cooling of a high performance switched reluctance machine (srm) for ev/hev applications," *SAE International Journal of Alternative Powertrains*, vol. 4, no. 1, pp. 162–169, 2015.
- [9] —, "Comparison of thermal performance between direct coil cooling and water jacket cooling for electric traction motor based on lumped parameter thermal network and experimentation," in *Proceedings of the EVS28 International Electric Vehicle Symposium and Exhibition, Goyang, Korea*, 2015, pp. 3–6.
- [10] A. Acquaviva, S. Skoog, and T. Thiringer, "Design and verification of in-slot oil-cooled tooth coil winding pm machine for traction application," *Submitted to IEEE Transactions on Industrial Electronics*, Dec. 2019.
- [11] A. Acquaviva, S. Skoog, E. Grunditz, and T. Thiringer, "Electromagnetic design and testing of tooth coil winding pm machine for traction application," *Submitted to IEEE Transactions on Industrial Electronics*, Feb. 2020.
- [12] A. Acquaviva, "Analytical electromagnetic sizing of inner rotor brushless pm machines based on split ratio optimization," in *ICEM '18, Alexandroupoli*, 2018.
- [13] S. Skoog and A. Acquaviva, "Pole-slot selection considerations for double layer three-phase tooth-coil wound electrical machines," in *ICEM '18, Alexandroupoli*, 2018.